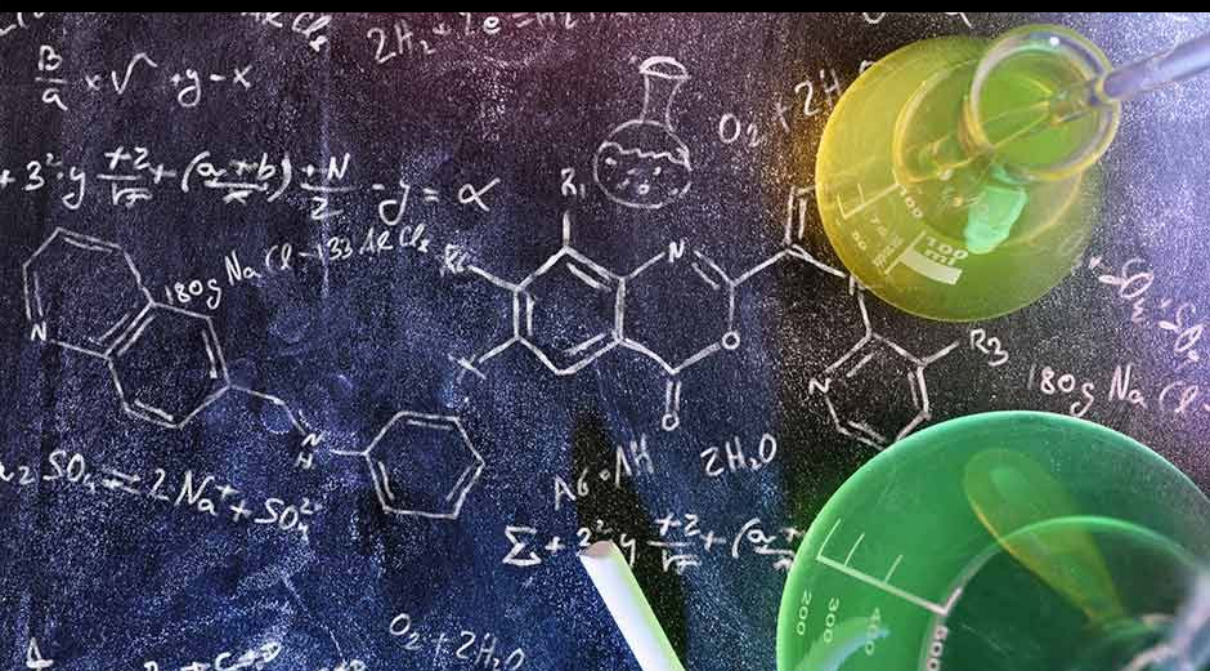# DEVELOPMENTS IN SCIENCE

Physics, Chemistry, Biology

Editor: Prof. Dr. Sibel DEMİR KANMAZALP

Developments in Science:

Physics, Chemistry, Biology

Editor

Prof. Dr. Sibel DEMİR KANMAZALP

yaz
yayınları

2023

Developments in Science: Physics, Chemistry, Biology

Editor: Prof. Dr. Sibel DEMİR KANMAZALP

CONTENT

BODIPYS AS LASER DYES: RECENT ADVANCES

Seda CETINDERE[1]

1. INTRODUCTION

A laser is a device designed to produce coherent light waves across the ultraviolet (UV), visible (VIS), and near-infrared (NIR) regions (Prohit, 2020). Lasers are typically classified based on their operational mode and the active medium employed, categorized into two primary types: continuous wave (CW) lasers and pulsed wave lasers. Furthermore, lasers can be grouped into four main categories according to the active medium used: solid-state, liquid, gas, and semiconductor lasers (Shankarling & Jarag, 2010). The essential components of a laser system are depicted in Scheme 1. In this illustration, the active medium is represented by a dye dissolved in a liquid solvent, which is responsible for stimulated emission. A light pump is employed to supply the necessary energy for achieving population inversion. Mirror 1 and mirror 2 act as parallel reflectors, enhancing stimulated emission by enabling multiple reflections within the laser cavity. A small fraction of the laser light exits the cavity through mirror 2 and is utilized for various specific applications.

Dye lasers are recognized for their versatility as laser sources, making significant contributions to fundamental chemistry, physics, and numerous other scientific disciplines. These lasers employ an organic dye as the lasing medium,

---

[1] Dr., Gebze Technical University, Department of Chemistry, sdemirer@gtu.edu.tr, ORCID: 0000-0001-7599-8491.

commonly in the form of a liquid solution. Dye lasers have the remarkable capability to generate laser light across a broad spectrum of wavelengths, typically spanning 50 to 100 nanometers in width. The wide bandwidth of dye lasers makes them exceptionally well-suited for tunable and pulsed laser applications. For instance, rhodamine 6G can be tuned across a range from 635 nm to 560 nm, capable of producing incredibly short pulses as brief as 16 femtoseconds. The pioneering work of Sorokin and Lankard, as well as Schäfer et al., in 1966, marked the initial discoveries of organic dye lasers (Sorokin & Lankard 1966; Schäfer et. al., 1966). Tunability stands as an intrinsic and crucial characteristic of dye lasers, an insight initially brought to light by Soffer and McFarland (Soffer & McFarland, 1967). Dye lasers are closely associated with offering extensively tunable coherent emissions, a feature poised to become indispensable in established scientific domains such as photochemistry (Ready & Erf, 1984) and spectroscopy (Demtröder, 2007). Furthermore, they are set to catalyze the development and exploration of new research fields, including laser isotope separation (Radziemski et al., 1987; Bokhan et al., 2006), laser cooling (Diedrich et al., 1989), and tunable laser medicine (Duarte, 2012; Costela et al., 2009). Due to their wide-ranging applications and consequent popularity, dye lasers have given rise to an extensive body of scientific literature. In the present day, dye lasers continue to find utility in numerous applications that demand exceptional wavelength versatility in the visible spectrum or specific throughput characteristics, such as high average power or substantial pulse energy. As a result, dye lasers are a valuable source of coherent radiation, complementing the advancements made in solid-state lasers over the past two decades. Boron-dipyrromethene (BODIPY) dyes are a class of fluorescent dyes meticulously designed for laser applications, offering tunability within the green-yellow visible range of the electromagnetic spectrum (EMS). These dyes are characterized by outstanding

features, including high photostability, a strong fluorescence quantum efficiency, low-rate constants of intersystem transition, and a substantial molar absorption coefficient. The introduction of suitable molecular substitutions into the parent BODIPY chromophore allows for the modulation of the photophysical properties of these dyes to a certain extent. This chapter aims to provide a comprehensive overview of the lasing properties exhibited by BODIPY dyes in recent years.

Scheme 1. Basic Elements of A Laser
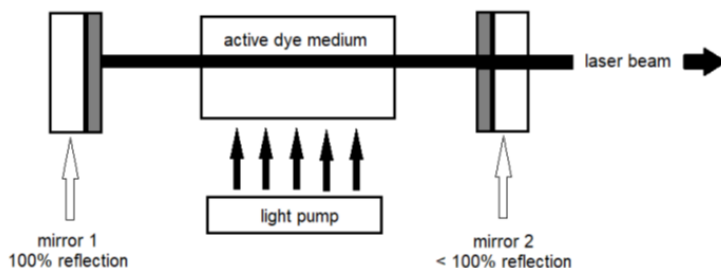
2. CHARACTERISTICS OF LASER DYES

BODIPY laser dyes consist of intricate molecules with a series of ring structures, leading to intricate absorption and emission profiles (Schäfer, 1990). Organic dyes are defined by their pronounced absorption bands within the visible range of the EMS (Gregory, 1991). This feature is typically found in organic compounds with an extended system of conjugated bonds, particularly alternating single and double bonds. Determining light absorption from the molecular structure of dyes is a complex quantum-mechanical problem. However, simplified models have been developed to explain many experimental observations, especially within specific classes of dyes. The long-wavelength absorption band of these dyes is associated with the transition from the electronic ground state S_0 to the first excited singlet state

S_1. In this transition, the magnitude of the transition moment is typically significant, giving rise to an absorption band characterized by a nearly uniform oscillatory force. In contrast, the process from S_1 to S_0 is responsible for natural emission, known as fluorescence, and for the excited emission observed in dye lasers. Thanks to their substantial transition moment, dye lasers exhibit a notably high rate of natural emission, enabling them to surpass the gain achieved by solid-state lasers by several orders of magnitude (Drexhage, 1973). When a dye laser is excited by an intense light source, such as another laser, the dye molecules are typically elevated to a higher level within the singlet manifold. From this higher state, they promptly relax to the lowest vibronic level of S_1, which corresponds to the highest laser level (as shown in Scheme 2). To ensure optimal long-term yield, it's crucial for the dye molecules to remain at this level until stimulated emission is initiated. While dye lasers cover a wide range of wavelengths, spanning from the near-UV to the near-IR, and employ dyes with diverse chemical compositions, the underlying principles remain consistent. An explanation based on the velocity equation approximation and transverse sections for excited emission and absorption is commonly utilized, regardless of the material or wavelength. In practical systems that employ dyes, the relevant parameters often have similar values. The radiation characteristics of laser dyes depend on the structural composition of the dye molecules and their interaction with the solvent. A wealth of literature is available on the spectroscopic, photophysical, and chemical properties of dyes (Zlatić et al., 2020; Bezrodna et al., 2021). In practical dye laser systems, the dye is blended with a compatible solvent, ensuring uniform dispersion of the molecules within the liquid medium. To exceed the permanent threshold, a high-energy light source is required to 'pump' the fluid. Typically, this involves the use of a fast discharge flash tube or an external laser. The dyes used in these lasers consist of relatively large, organic compounds known for

their fluorescence. Most dyes exhibit very short fluorescence lifetimes, typically on the order of a few nanoseconds. To ensure optimal performance, dye molecules must exhibit specific key characteristics, which include strong absorption at the excitation wavelength and minimal absorption at the lasing wavelength. Equally significant are several key characteristics for laser dyes, including a high quantum yield, typically falling within the range of 0.5 to 1.0, as well as photochemical stability. Typically, these dyes also feature a short fluorescence lifetime, typically falling within the range of 5 to 10 nanoseconds and demonstrate low absorption in the first excited state during the pumping process. Furthermore, maintaining a high level of purity is essential for laser dyes since impurities can frequently quench the laser output. Through careful dye selection, it becomes possible to generate coherent light at the desired wavelength within the broad range of 320 to 1200 nanometers.

Scheme 2. The Energy Levels of An Organic Dye Molecule, Illustrating Its Key Electronic States and Transitions
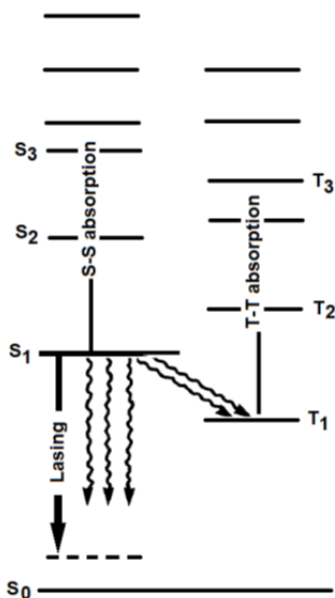
3. BODIPYS AS LASER DYES

Fluorescent dyes have been the subject of extensive research within the scientific community across various interdisciplinary fields (Liu et al., 2021; Wrona-Piotrowicz et al., 2022; Kim et al., 2022; Wangngae et al., 2021). The profound interest in these dyes has paved the way for their successful utilization as active media in tunable lasers, the advancement of photoelectronic devices, applications as fluorescent probes and chemical sensors, as well as monitoring the physicochemical attributes of their surrounding environments (de Silva et al., 1997; Valeur & Leray, 2020; Rurack & Resch-Genger, 2002; Lakowicz, 2006). Understanding the photophysical properties of these systems holds significant importance, not only for their inherent potential applications but also for the design of new dyes tailored to specific properties. In fact, a well-established correlation has been identified (Vogel et al., 1988; Reisfeld et al., 1984; Arbeloa et al., 1990; 1997; Huang et al., 1999) between the photophysical properties and enduring characteristics of various laser dyes. This correlation can be observed through variations in the molecular structure of the chromophore (e.g., substitution effects) and environmental conditions (e.g., solvent effects). Among the numerous laser dye families that span the UV to near-IR spectral region (Maeda, 1984), BODIPYs have garnered particular attention. Their fundamental structure comprises two pyrrole rings interconnected by a methene and a BF_2 group. The first report on these dyes was documented by Treibs and Keuzer in 1968 (Treibs & Kruzer, 1968). However, their significance did not gain recognition within the scientific community until the late 1990s when reports by Boyer and Pavlopoulos highlighted their potential applications in tunable lasers (Pavlopoulos et al., 1988; 1990; Shah et al.; 1990). These encouraging findings spurred further research to delve deeper into their enduring properties and to leverage this family of dyes in various other domains, including

biology and medicine (Metzker et al., 1966; Reents et al., 2004). As a result, numerous publications swiftly emerged, providing comprehensive insights into their features and applications (Loudet & Burgess, 2017; Wood & Thompson, 2017; Ulrich et al., 2008). Comprehensive knowledge of the photophysical behavior of BODIPY dyes is indispensable for understanding their enduring effects and for the development of new photoelectronic sensors or devices based on BODIPYs. BODIPY laser dyes exhibit robust absorption and fluorescence bands in the visible spectral range, resulting in high fluorescence yield (Karolin et al., 1994; Shen et al., 2004; Quartorolo et al., 2006; Cui et al., 2007) and enduring efficiency (Mackey & Sisk, 2001; Jones et al., 2001). Furthermore, their versatility, chemical stability, low ternary state populations, as well as thermal and photochemical stability, bolster the photosensitive properties of these dyes. For instance, when BODIPY dyes are embedded within solid parent matrices, highly efficient laser signals can be generated after successive pumping pulses (Yariv et al., 2001; Ahmad et al, 2002). This capability facilitates the creation of solid-state tunable dye lasers, offering notable advantages over liquid-state lasers, including improved manageability, versatility, miniaturization of the experimental setup, and the absence of toxic and flammable solvents (Costela et al., 2003). Figure 1 displays several commercially available BODIPY dyes. For example, commercially recognized BODIPY complex, the Pyromethene-567 (PM567), emits laser light at 567 nm, with an output approximately three times higher than Rhodamine 560 (Shankarling & Jarag, 2010). Several other BODIPY dyes exhibit similar levels of efficiency. Figure 2 lists various BODIPY dyes with different substituents at the 3- and 5-positions (Shankarling & Jarag, 2010). Furthermore, In Figure 3, the synthesis of the 8-propargylamino BODIPY laser dye (7) with emissions in the blue spectral region is presented (Shankarling & Jarag, 2010).

Figure 1. Some Commercially BODIPY Laser Dyes

PM567

PM580

PM597
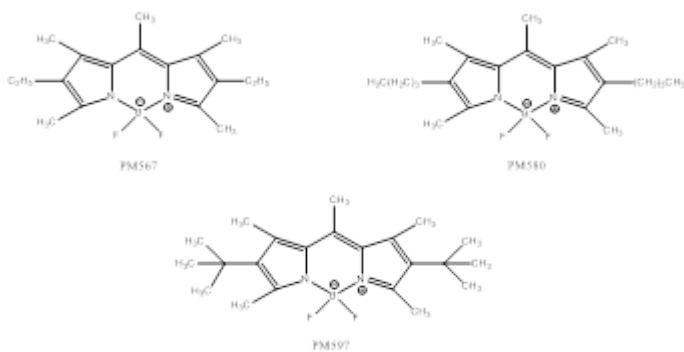
Figure 2. Some BODIPY Laser Dyes

(1)

(2)

(3)

(4)

(5)

(6)
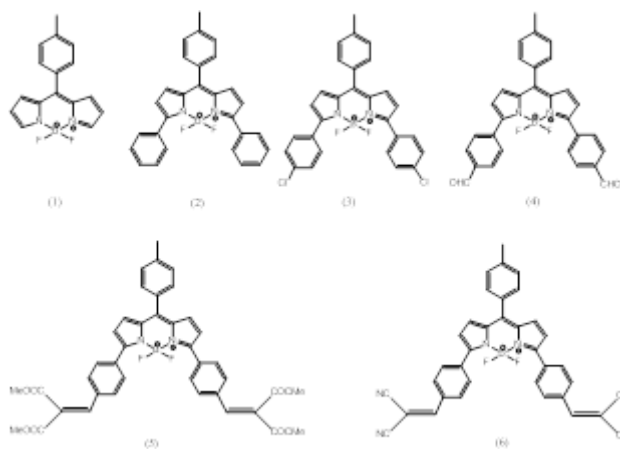
Figure 3. The Structure Of 8-Propargylamino BODIPY Laser Dye

(7)
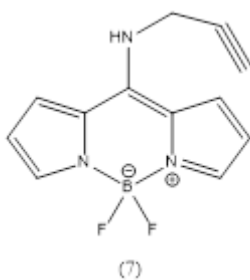
In 2007, a study introduced two new analogs of the commercial dye PM567, namely pyrromethene with a mono-acetoxy group (8) and pyrromethene with a di-acetoxy group (9) (as depicted in Figure 4). These compounds exhibited superior laser emission and greater photostability in liquid solutions when compared to the parent dye PM567 (García-Moreno et al., 2007). Furthermore, another study presented a straightforward method for the synthesis of asymmetric 3-amino- and 3-acetamido-BODIPY dyes derived from 2,3,4-trialkyl-substituted pyrroles. Among these dyes, the acetylated dye (10) (as shown in Figure 4) displayed commendable laser emission properties (Liras et al., 2007).

Figure 4. Molecular Structures of the BODIPY Dyes (8-10)
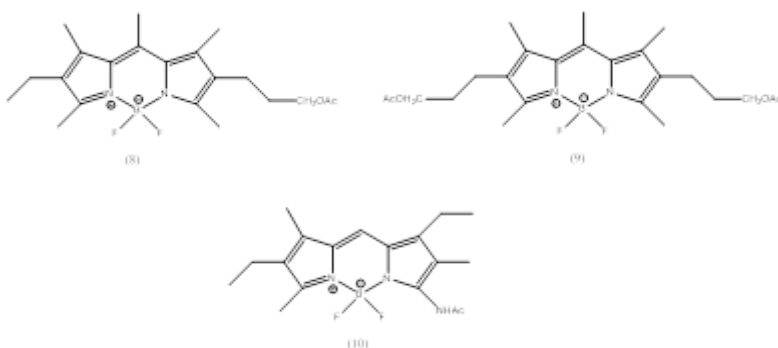
In a study led by Costela et al., they reported the synthesis, photophysical properties, and evaluation of a BODIPY laser dye featuring a 3-styryl substituent (11), as depicted in Figure 5 (Costela et al., 2008). In the same year, Alvarez et al. carried out another investigation focusing on the synthesis and lasing characteristics of four new dyes. All of these dyes shared the fundamental structure of the commercial BODIPY laser dye PM567. They featured either an 8-diphenylene or an 8-p-triphenylene group, both substituted at the terminal polyphenylene position with either an acetoxymethyl (12-13) or a methacryloyloxymethyl group (14-15), as illustrated in Figure

5 (Alvarez et al., 2008). Among these dyes, the one with two phenylene rings at position 8 (14), when dissolved in poly(methylmethacrylate) (PMMA), exhibited the most favorable overall laser behavior. This particular dye demonstrated a well-balanced combination of efficiency and photostability.

Figure 5. Molecular Structures of the BODIPY Dyes (11-15)
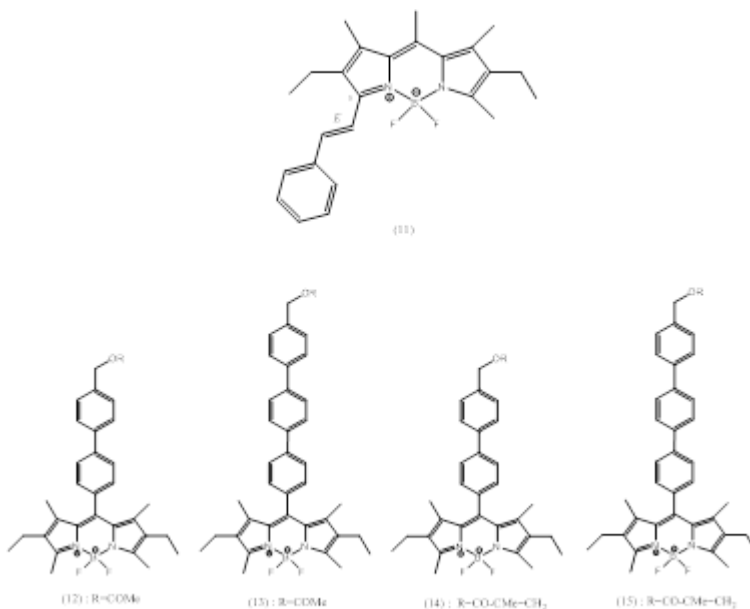
Ortiz and colleagues conducted the synthesis of BODIPY dyes featuring different phenyl groups at the 3- and 5-positions, as depicted in Figure 6. Their study revealed that these dyes exhibit remarkable laser photostability, surpassing that of commercial dyes with laser emissions in the same spectral region, such as Rhodamine 640 (Ortiz et al., 2010). The synthesized BODIPY dyes (16-19) display high efficiency and exceptional photostability, offering fine-tunable wavelength capabilities across a broad range (590–680 nm) with a narrow line width.

Figure 6. Molecular Structures of the BODIPY Dyes (16-19)

(16) : R= Cl

(17) : R= —⟨ ⟩—CHO

(18) : R= —⟨ ⟩—CH=C(CO₂Me)₂

(19) : R= —⟨ ⟩—CH=C(CN)₂
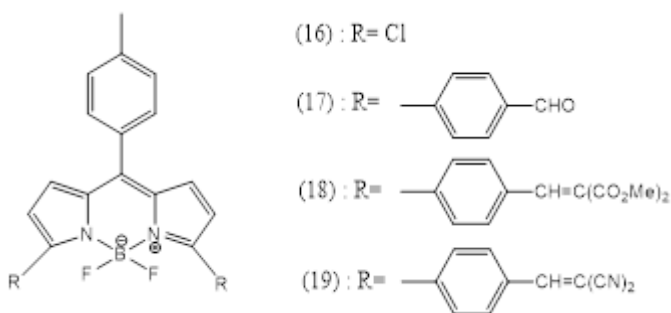
Banuelos and colleagues designed and synthesized blue-emitting dyes (20-25) featuring various amino groups at the 8-position, ranging from primary to tertiary amines, as illustrated in Figure 7 (Banuelos et al. 2011). Remarkably, under rigorous transversal pumping conditions, these dyes exhibited unexpectedly high lasing efficiencies, reaching up to 63%. Moreover, they demonstrated exceptional photostability, surpassing the lasing properties of commercial dyes emitting in the same spectral region under identical experimental conditions. In the same year, Zhang et al. reported compounds (26-29) synthesized through the condensation of the BODIPY core and aromatic aldehydes using Knoevenagel reactions (Zhang et al., 2011). Compound (26) was synthesized as a reference to assess the impact of combining different electron-donating groups on optical properties and laser behavior. These compounds demonstrated efficient and stable laser emissions that can be tuned across a range from green to the NIR spectral region (565–720 nm). Compounds (27) and (28) emitted longer wavelengths and exhibited substantial Stokes shifts. The presence of a triphenyl amino and a tetrahydroquinoline group, respectively, led to reduced fluorescent quantum yields and broader emission bands in polar solvents. These photophysical properties qualify these BODIPY compounds as exceptional laser dyes in the red-edged spectral region. Their performance enhances the laser

efficacy of well-known dyes emitting at the same wavelengths, contributing to overall laser efficiency and photostability.

Figure 7. Molecular Structures of 8-amino-substituted BODIPY Dyes (20-25)
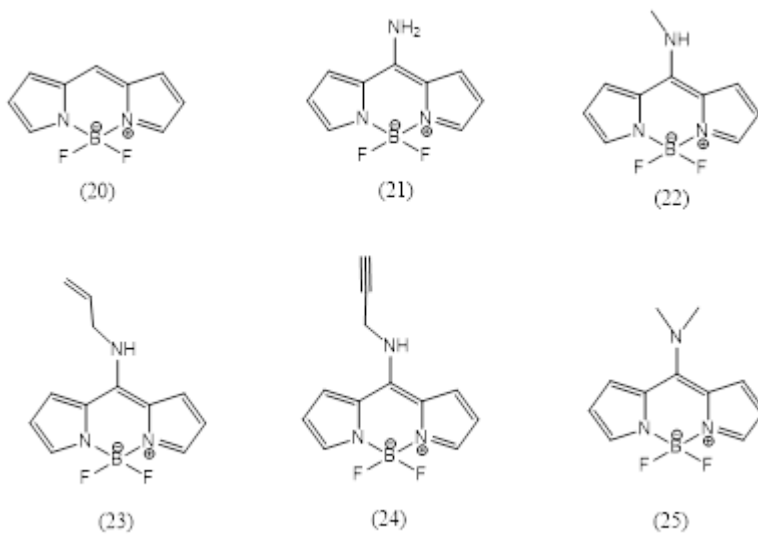
Figure 8. Molecular Structures of Mono-Styryl BODIPY Dyes (26-29)
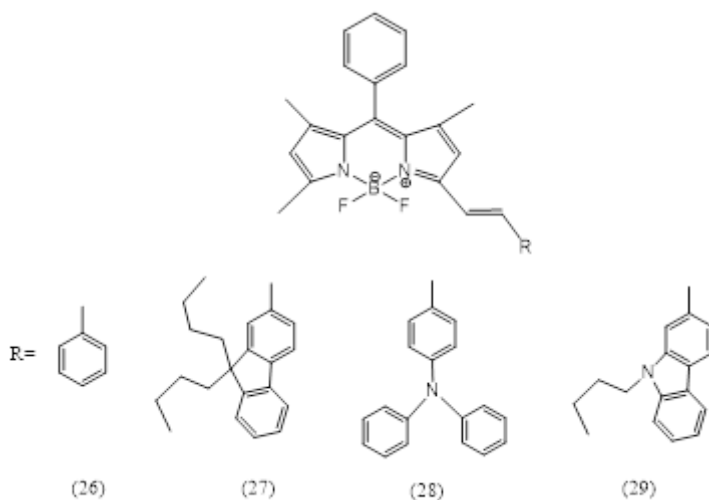
Perez-Ojeda et al. reported the remarkable lasing potential of di-iodinated BODIPY dyes (30–33) depicted in Figure 9 (Perez-Ojeda et al., 2011). Previously, these dyes were utilized as doping agents in polyfluorenes (Thivierge et al., 2011). These particular BODIPYs (30-32) have exhibited highly efficient and photostable laser emissions with wavelength tunability under demanding laser pumping conditions in both liquid and solid states. Notably, their properties surpass those of some commercially available laser dyes, including coumarin derivatives. Perez-Ojeda et al. also documented the efficient and stable laser emissions produced by BODIPY dye (33) (as shown in Figure 9) when incorporated into polymeric hosts under intense UV pumping conditions (Perez-Ojeda et al., 2012).

Figure 9. Molecular Structures of BODIPY Dyes (30-33)
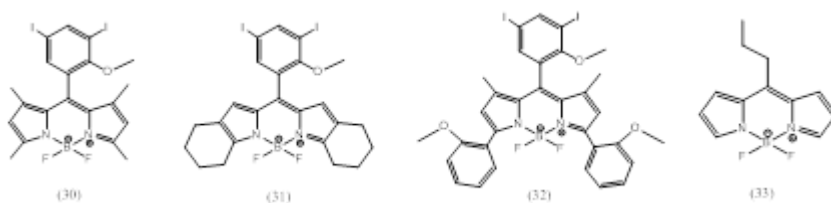
Duran-Sampedro et al. reported the synthesis of E- and C-BODIPY derivatives (34–40) (as illustrated in Figure 10) obtained from commercially available BODIPYs. They conducted a systematic investigation into the photophysical properties and laser behavior of these dyes, closely associated with the electronic properties of the B-substituent groups (Duran-Sampedro et al., 2014). Both E- and C-BODIPYs showed significantly improved laser performance when compared to their parent dyes, whether in liquid or solid phases. Notably, the lasing properties exhibited a strong correlation with their photophysical characteristics.

Figure 10. Molecular Structures of BODIPY Dyes (34-40)

34a, 35a : R^1=Me; R^2=H
34b, 35b, 37a : R^1=Me; R^2=Et
34c, 35c : R^1=Me; R^2=nBu
34d, 35d, 37b : R^1=Me; R^2=tBu
34c, 35e: R^1=C_6H_{13}; R^2=tBu
36a: Ar=TMS-C≡C-C_6H_4
36b: Ar=HC≡C-C_6H_4
37c: R^1=CH_2OCOMe; R^2=Et
37d: R^1=CN; R^2=Me
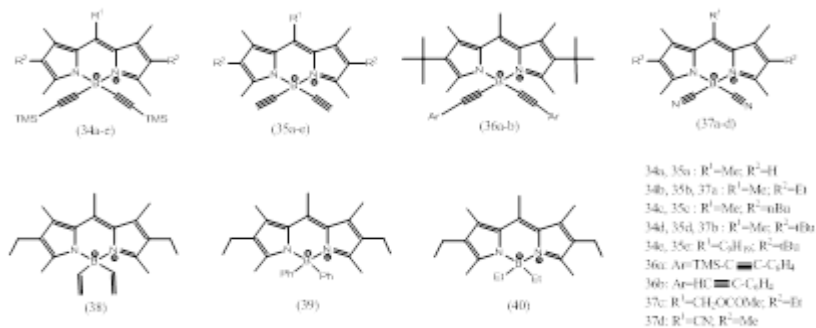
Esnal and colleagues introduced a series of coumarin-BODIPY hybrids (41-52), as depicted in Figure 11 (Esnal et al., 2015). These hybrids were formed by combining amino and hydroxycoumarins with BODIPYs, employing amino or hydroxyl groups, resulting in the straightforward production of distinctive and photostable coumarin–BODIPY hybrids. These hybrids displayed heightened absorption in the UV spectral region and showcased remarkable wavelength-tunable laser capabilities, covering the spectrum from green to red regions (~520–680 nm). Their ability to double the frequency makes them highly valuable. Moreover, they offer a versatile, tunable UV (~260–350 nm) laser source. The degree of tunability depends on the hybrid's substitution model, including factors such as the linker heteroatom, the number of coumarin units integrated into the BODIPY framework, and their respective attachment positions. The successful development of these BODIPY and coumarin-based hybrids addresses a significant challenge in advancing advanced photonic materials and related applications.

Figure 11. Molecular Structures of BODIPY Dyes (41-52)
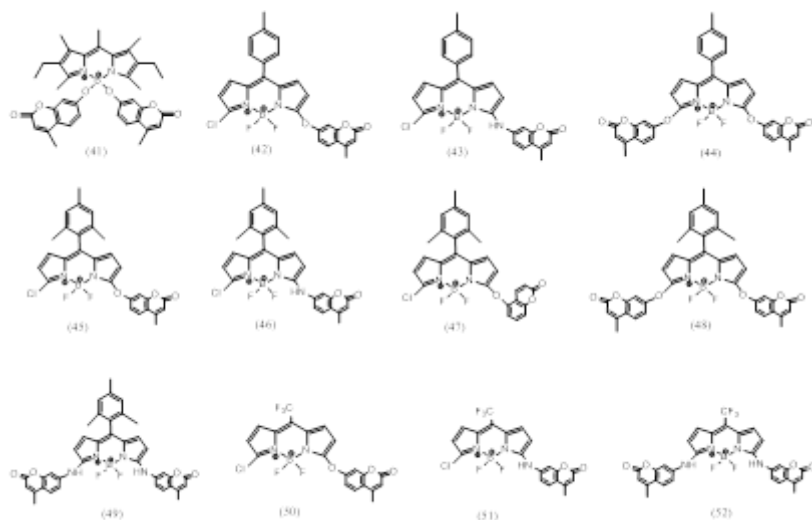
In their research, Waddell and colleagues introduced a series of BODIPY dyes (53-29) as depicted in Figure 12. These dyes featured non-aryl substituents at the 8- and 2/6-positions (Waddell et al., 2015). This study highlighted both the practicality and constraints of using crystal structure data to establish structure-property relationships within this class of optical materials. Their research contributes to the continuous endeavors focused on designing optoelectronic materials with adjustable properties through molecular engineering. Meanwhile, Palao and colleagues conducted a systematic investigation into the applicability of the Negishi reaction to halo-BODIPYs. Their work underscores the increasing interest in the Negishi reaction as a valuable synthetic tool for advancing BODIPY dyes (Palao et al., 2016). The Negishi reaction involving halo-BODIPYs was notably affected by the particular BODIPY position and the type of halogen atom. This allowed for partial functionalization in polyhalogenated systems through the appropriate selection of reaction conditions. The halogenated BODIPYs obtained in this process serve as vital synthetic intermediates for the production

of other asymmetrical BODIPYs that are challenging to prepare through alternative synthetic methods. Additionally, the investigation of the persistence properties of these dyes revealed unexpectedly remarkable persistence characteristics for unconventional BODIPY laser dyes, demonstrating the potential of the Negishi reaction in developing more versatile BODIPY dyes for advanced photonic applications.

Figure 12. Molecular Structures of BODIPY Dyes (53-59) (R=H, Me, Et, nBu or tBu; R'=Me, C$_4$H$_{11}$ or CH$_2$OC(O)Me))
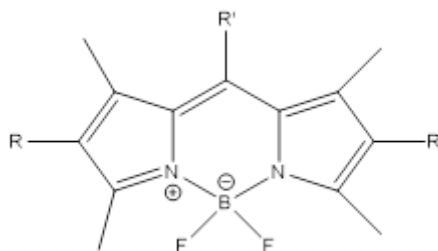
Gupta et al. presented the synthesis of BODIPY dye (60) featuring two propargyl alcohol moieties at the B-center, illustrated in Figure 13 (Gupta et al., 2017). This dye exhibited a high degree of fluorescence and demonstrated lasing efficiency comparable to that of the commercial dye PM567 (61). Notably, it showcased superior photostability in both polar (ethanol) and non-polar (1,4-dioxane) solvents.

Figure 13. Molecular Structure of BODIPY Dye (60 and 61)

(60)

(61)
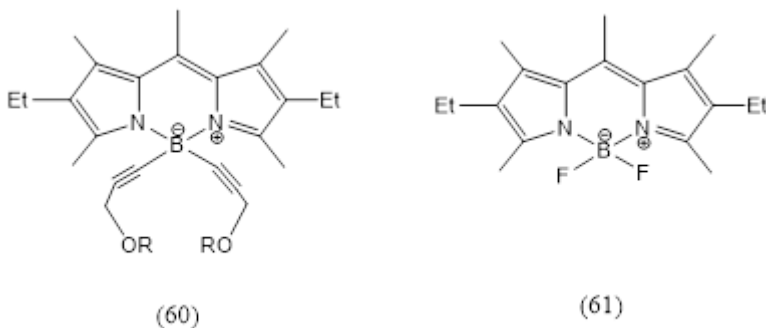
Ray and colleagues introduced a simple method for the synthesis of valuable COO-BODIPYs. They accomplished this by employing readily available F-BODIPYs and carboxylic acids under mild conditions and with brief reaction times, utilizing BCl3 as the activating agent (Ray et al., 2020). This gentle approach has opened up new possibilities for the creation of unprecedented laser dyes known for their remarkable efficiency and photostability, qualities that are often challenging to achieve using current methods. In a separate study, Maity et al. successfully designed and developed alkynyl-cored BODIPY dyes (62-63) featuring perfluorinated substituents (Maity et al., 2020). They also reported the random lasing properties of these synthesized BODIPY dyes within a polydimethylsiloxane (PDMS)-based microfluidic device (MFD).

Figure 14. Molecular Structure of BODIPY Dye (62 and 63)

(62)   (63)
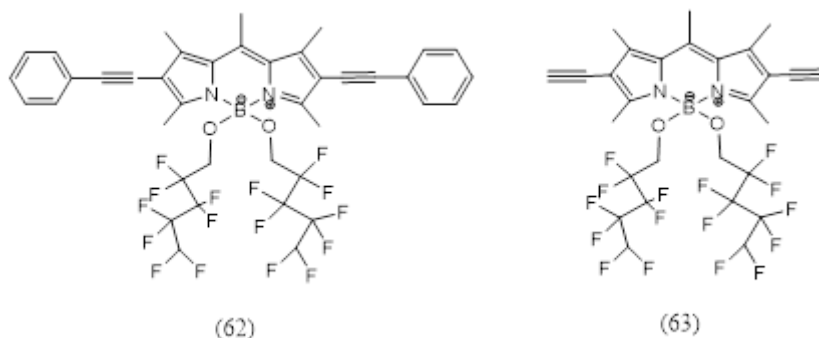
Recently, A. Prakash and colleagues conducted a study centered on the fabrication and investigation of the lasing properties of BODIPY dye-doped polymer optical fibers (DDPOFs) using two distinct pumping schemes. They utilized a π-extended BODIPY derivative, BDIPA (64), as the laser dye gain medium, in combination with PMMA to create BDIPA DDPOFs. Their research findings revealed the potential utility of BDIPA dye as a highly efficient solid-state lasing material with desirable properties.

Figure 15. Molecular Structure of BODIPY Dye (64).

(64)
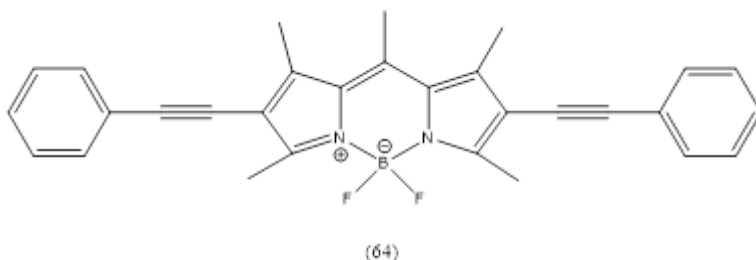
4. CONCLUSION

Dye laser technology has witnessed substantial advancements, especially over the last two decades, expanding upon its origins that trace back to the first laser action accomplished using chloro-aluminum phthalocyanine. Laser dyes have discovered applications across a multitude of scientific and industrial sectors, ranging from spectroscopy to potential countermeasure devices. The advancement of new dye lasers is centered on enhancing their ease of tuning, broad wavelength coverage, and synthetic simplicity. A promising avenue for creating novel laser dyes involves substituting functional groups within classes of laser dyes that already possess excellent laser properties. Among the various types of lasers available, those employing organic molecules as active media stand out. Organic BODIPY dyes have emerged as key players in the green/red visible spectral region. The rich and versatile chemistry of BODIPYs makes them a powerful resource for crafting a spectrum of photo-active dyes capable of serving as efficient and stable tunable lasers, covering the spectral window from 600 to 725 nm. The spectroscopic and photophysical properties of BODIPYs hold significant applications in photonics, particularly as the active medium in synthesizable dye lasers. The future of laser dyes appears promising. Presently, the primary challenge in

advancing dye lasers lies in enhancing their photostability and broadening the output range of dyes.

REFERENCE

Ahmad, M.; King, T. A.; Ko, D-K.; Cha, B. H.; Lee, J. (2002). Performance and photostability of xanthene and pyrromethene laser dyes in sol-gel phases. J. Phys. D, 35 1473.

Alvarez, M., Costela, A., García-Moreno, I., Amat-Guerri, F., Liras, M., Sastre, R., Lopez Arbeloa, F., Banuelos Prieto, J., Lopez Arbeloa, I. (2008). Photophysical and laser emission studies of 8-polyphenylene-substituted BODIPY dyes in liquid solution and in solid polymeric matrices. Photochem. Photobiol. Sci., 7, , 802–813.

Arbeloa, F.L.; Costela, A.; Arbeloa, I.L. (1990). Molecular structure effects on the lasing properties of rhodamines. J. Photochem. Photobiol. A, 55, 97.

Arbeloa, T.L.; Arbeloa, F.L.; Arbeloa, I.L.; Costela, A.; García-Moreno, I.; Figuera, J. M.; Amat-Guerri, F.; Sastre, R. (1997). Photophysical and lasing properties of a new ester derivative of rhodamine 6G J. Lumin., 75, 309.

Banuelos, J., Martin, V., Gomez-Duran, C. F. A., Cordoba, I. J. A., Pena-Cabrera, E., Garcia-Moreno, I., Costela, A., Perez-Ojeda, M. E., Arbeloa, T., Arbeloa, I. L. (2011). New 8-Amino-BODIPY Derivatives: Surpassing Laser Dyes at Blue-Edge Wavelengths. Chem. Eur. J., 17, 7261 – 7270.

Bezrodna, T.V.; Bezrodny, V.I.; Negriyko, A.M.; Kosyanchuk, L.F. 2021. Spectral, photophysical and lasing properties of Rhodamine dyes in the polyurethane acrylate matrix. Optics & Laser Technology, 138, 106868.

Bokhan, P.A.; Buchanov, V.V.; Fateev, N.V.; Kalugin, M.M.; Kazaryan, M.A.; Prokhorov, A.M.; Zakrevskii, D.E. (2006). Laser Isotope Separation in Atomic Vapor, Wiley-VCH, Weinheim.

Costela, A.; García-Moreno, I.; Sastre, R. (2003). Polymeric solid-state dye lasers: Recent developments. Phys. Chem. Chem. Phys., 5, 4745.

Costela, A., García-Moreno, I., Pintado-Sierra, M., Amat-Guerri, F., Liras, M., Sastre, R., Lopez Arbeloa, F., Banuelos Prieto, J., Lopez Arbeloa, I. (2008). New laser dye based on the 3-styryl analog of the BODIPY dye PM567. Journal of Photochemistry and Photobiology A: Chemistry, 198, 192–199.

Costela, A.; García-Moreno, I.; Sastre, R. (2009). Solid-State Organic Dye Lasers. Tunable Laser Applications. Duarte F.J. (Ed.), CRC, New York, p. 97.

Cui, A.; Peng, X.; Fan, J.; Chen, X.; Wu, Y.; Guo, B. (2007). Synthesis, spectral properties and photostability of novel boron–dipyrromethene dyes. J. Photochem. Photobiol. A, 186, 85.

Demtröder, W. (2007). Laserspektroscopie: Grundlagen und Techniken, 5th ed., Springer, Berlin.

Diedrich, F.; Bergquist, J. C.; Itano, W.M.; Wineland, D. J. (1989). Laser Cooling to the Zero-Point Energy of Motion. Phys. Rev. Lett., 62, 403.

Drexhage, K.H. (1973). Structure and properties of laser dyes. Dye lasers, Springer.

Duarte, F.J. (2012). Tunable organic dye lasers: Physics and technology of high-performance liquid and solid-state narrow-linewidth oscillators. Progress in Quantum Electronics, 36, 29-50.

Duran-Sampedro, G., Esnal, I., Agarrabeitia, A. R., Prieto, J. B., Cerdan, L., Garcia-Moreno, I., Costela, A., Arbeloa, I. L., Ortiz, M. J. (2014). First Highly Efficient and Photostable E and C Derivatives of 4,4-Difluoro-4-bora-3a,4a-diaza-s-indacene (BODIPY) as Dye Lasers in the Liquid Phase, Thin Films, and Solid-State Rods. Chem. Eur. J., 20, 2646 – 2653.

Esnal, I., Duran-Sampedro, G., Agarrabeitia, A. R., Banuelos, J., Garcia-Moreno, I., Macias, M. A., Pena-Cabrera, E., Arbeloa, I. L., de la Moya S., Ortiz, M. J. (2015). Coumarin–BODIPY hybrids by heteroatom linkage: versatile, tunable and photostable dye lasers for UV irradiation. Phys. Chem. Chem. Phys., 17, 8239—8247.

García-Moreno, I., Amat-Guerri, F., Liras M., Costela, A., Infantes, L., Sastre, R., Arbeloa, F. L., Prieto, J. B., Arbeloa, I. L. (2007). Structural Changes in the BODIPY Dye PM567 Enhancing the Laser Action in Liquid and Solid Media. Adv. Funct. Mater., 17, 3088–3098.

Gregory, P. (1991). High Technology Applications of Organic colorants. Eds: Alan R. Katritzky, Gebran J. Sabongi. Plenum Press, New York, London, pp.27– 28.

Gupta, M., Mula, S., Ghanty, T. K., Naik, D. B., Ray, A. K., Sharma, A., Chattopadhyay, S. (2017). Structure and solvent-induced tuning of laser property and photostability of a boradiazaindacene (BODIPY) dye. Journal of Photochemistry and Photobiology A: Chemistry, 349,162–170.

Huang, J.; Bekiari, V.; Lianos, P.; Couris, S. (1999). Study of poly(methyl methacrylate) thin films doped with laser dyes. J. Lumin., 81, 285.

Jones, G.; Klueva, O.; Kumar, S.; Pacheco, D. (2001). Photochemical and lasing properties of pyrromethene dyes. Int. Soc. Opt. Eng., 4267, 24.

Karolin, J.; Johansson, L. B-A.; Strandberg, L.; Ny, T. (1994). Fluorescence and absorption spectroscopic properties of dipyrrometheneboron difluoride (BODIPY) derivatives in liquids, lipid membranes, and proteins. J. Am. Chem. Soc., 116, 7801.

Kim, Y.T.; Oh, H.; Seo, M.Y.; Lee, D.H.; Shin, J.; Bong, S.; Heo, S.; Hapsari, N.D.; Jo K. (2022). Fluorescent Protein-Based DNA Staining Dyes. Molecules, 27, 5248.

Lakowicz, J. R. (2006). Principles of Fluorescence Spectroscopy. 3rd Ed., Springer, Singapore,.

Liras, M., Prieto, J. B., Pintado-Sierra, M., Arbeloa, F. L., Garcia-Moreno, I., Costela, A., Infantes, L., Sastre, R., Amat-Guerri, F. (2007). Synthesis, Photophysical Properties, and Laser Behavior of 3-Amino and 3-Acetamido BODIPY Dyes. Org. Lett., 9:21, 4183-4186.

Liu, P.; Wang, L.; Yang, Y.; Qu, Y.; Ming, L.J. (2021). Recent advances of cyclotriphosphazene derivatives as fluorescent dyes. Dyes and Pigments, 188, 109214.

Loudet, A.; Burgess, K. (2007). BODIPY dyes and their derivatives: syntheses and spectroscopic properties. Chem. Rev., 107, 4891.

Mackey, M. S.; Sisk, W.N. (2001). Photostability of pyrromethene 567 laser dye solutions via photoluminescence measurements. Dyes and Pigments, 51, 79.

Maeda, M. (1984). Laser Dyes. Academic Press, Tokyo.

Maity, A., Sarkar, A., Shivakiran-Bhaktha, B. N., Patra, S. K. (2020). Design and synthesis of perfluoroalkyl decorated BODIPY dye for random laser action in a microfluidic device. New J. Chem., 44, 14650—14661.

Metzker, M. L.; Lu, J.; Gibbs, R. A. (1996). Electrophoretically Uniform Fluorescent Dyes for Automated DNA Sequencing. Science, 271, 1420.

Ortiz, M. J., García-Moreno, I., Agarrabeitia, A. R., Duran-Sampedro, G., Costela, A., Sastre, R., Lopez Arbeloa, F., Banuelos Prieto, J., Lopez Arbeloa, I. (2010). Red-edge-wavelength finely-tunable laser action from new BODIPY dyes. Phys. Chem. Chem. Phys., 12, 7804–7811.

Palao, E., Duran-Sampedro, G., de la Moya S., Madrid, M., Garcia-Lopez, C., Agarrabeitia, A. R., Verbelen B., Dehaen, W., Boens, N., Ortiz, M. J. (2016). Exploring the Application of the Negishi Reaction of HaloBODIPYs: Generality, Regioselectivity, and Synthetic Utility in the Development of BODIPY Laser Dyes. J. Org. Chem., 81, 3700−3710.

Pavlopoulos, T. G.; Shah, M.; Boyer, J. H. (1988). Laser action from a tetramethylpyrromethene-BF$_2$ complex. Appl. Opt. 27, 4998.

Pavlopoulos, T. G.; Boyer, J. H.; Shah, M.; Thangaraj, K.; Soong, M.L. (1990). Laser action from 2,6,8-position trisubstituted 1,3,5,7-tetramethylpyrromethene-BF2 complexes: part 1. Appl. Opt. 29, 3885.

Perez-Ojeda, M. E., Thivierge, C., Martin, V., Costela, A., Burgess, K., Garcia-Moreno, I. (2011). Highly efficient and photostable photonic materials from diiodinated BODIPY laser dyes. Optical Materials Express, 1:2, 243-251.

Perez-Ojeda, M. E., Martin, V., Costela, A., Garcia-Moreno, I., Arroyo-Cordoba, I. J., Pena-Cabrera, E. (2012). Unprecedented solid-state laser action from BODIPY dyes under UV-pumping radiation. Appl Phys B, 106, 911–914.

Prasanna de Silva, A.; Nimal Gunaratne, H. Q.; Gunnlaugsson, T.; Huxley, A.J.M.; McCoy, C.P.; Rademacher, J.T.; Rice, T.E. (1997). Signaling Recognition Events with Fluorescent Sensors and Switches. Chemical Reviews, 97, 1515-1566.

Prohit, G. (2020). Overview of Lasers. Appl. Innov. Res., 2, 193-203.

Quartorolo, A. D.; Russo, N.; Sicilia, E. (2006). Structures and electronic absorption spectra of a recently synthesised class of photodynamic therapy agents. Chem. Eur. J., 12, 6797.

Ray, C., Schad, C., Moreno, F., Maroto, B. L., Banuelos, J., Arbeloa, T., Garcia-Moreno, I., Villafuerte, C., Muller, G., de la Moya S. (2020). BCl_3-Activated Synthesis of COO-BODIPY Laser Dyes: General Scope and High Yields under Mild Conditions. J. Org. Chem., 85, 4594−4601.

Radziemski, L.J.; Solarz, R.W.; Paisner J.A. (Eds.) (1987). Laser Spectroscopy and its Applications, Marcel Dekker, New York.

Ready, J.F.; Erf, R.K. (Eds.) (1984). Laser Applications, Academic, New York.

Reents, R.; Wagner, M.; Kulhmann, J.; Waldmann, H. (2004). Synthesis and Application of Fluorescence-Labeled Ras-Proteins for Live-Cell Imaging. Angew. Chem. Int. Ed., 43, 2711.

Reisfeld, R.; Brusilovsky, D.; Eyal, M.; Miron, E.; Burstein, Z.; Ivri, J. (1989). A new solid-state tunable laser in the visible. Chem. Phys. Lett. 160, 43.

Rurack, K.; Resch-Genger, U. (2002). Rigidization, preorientation and electronic decoupling—the 'magic triangle' for the design of highly efficient fluorescent sensors and switches. Chem. Soc. Rev. 31, 116.

Schäfer, F.P.; Schmidt, W.; Volze, J. (1966). Organic Dye Solution Laser. Appl. Phys. Lett., 9, 306.

Schäfer, F. P. (1990). Dye lasers and laser dyes in physical chemistry. Topics in Applied Physics. Vol. 70. Ed: Dr. Michael Stuke. Springer-Verlag, Berlin.

Shah, M.; Thangaraj, K; Soong, M.L.; Wolford, L. T.; Boyer, J. H.; Politzer, I. R.; Pavlopoulos, T. G. (1990). Pyrromethene–BF_2 complexes as laser dyes:1. Heteroat. Chem. 1, 389.

Shankarling, G.S.; Jarag, K.J. (2010). Laser Dyes. Resonance, 15, 804-818.

Shen, Z.; Röhr, H.; Rurack, K.; Uno, H.; Spieles, M.; Schulz, B.; Reck, G.; Ono, N. (2004). Boron–Diindomethene (BDI) Dyes and Their Tetrahydrobicyclo Precursors—en Route to a New Class of Highly Emissive Fluorophores for the Red Spectral Range. Chem. Eur. J., 10, 4853.

Soffer, B. H.; McFarland, B. B. (1967). Continuously Tunable, Narrow-Band Organic Dye Lasers. Appl. Phys. Lett., 10, 266.

Sorokin P. P., Lankard J.R. (1966). Stimulated emission observed from an organic dye, chloro-aluminum phthalocyanine. IBM J. Res. Develop. 10:162-3.

Thivierge, C., Loudet, A., Burgess, K. (2011). Brilliant BODIPY-fluorene copolymers with dispersed absorption and emission maxima. Macromolecules, 44(10), 4012–4015.

Treibs, A.; Kruzer, F.H. (1968). Difluorboryl-Komplexe von Di- und Tripyrrylmethenen. Justus Liebigs Ann. Chem. 718, 208.

Ulrich, G.; Ziessel, R.; Harriman, A. (2008). The chemistry of fluorescent bodipy dyes: versatility unsurpassed. Angew. Chem. Int. Ed., 47, 1184.

Valeur, B.; Leray, I. (2000). Design principles of fluorescent molecular sensors for cation recognition. Coord. Chem. Rev., 205, 3-40.

Vogel, M.; Rettig, W.; Sens, R.; Drexhage, K.H. (1988). Structural relaxation of rhodamine dyes with different N-substitution patterns: A study of fluorescence decay times and quantum yields. Chem. Phys. Lett. 147, 452.

Waddell, P. G., Liu, X., Zhao, T., Cole, J. M. (2015). Rationalizing the photophysical properties of BODIPY laser dyes via aromaticity and electron-donor-based structural perturbations. Dyes and Pigments, 116, 74-81.

Wangngae, S.; Chansaenpak, K.; Nootem, J.; Ngivprom U.; Aryamueang, S.; Lai, R.Y.; Kamkaew, A. (2021). Photophysical Study and Biological Applications of Synthetic Chalcone-Based Fluorescent Dyes. Molecules, 26, 2979.

Wrona-Piotrowicz, A.; Makal, A.; Zakrzewski, J. (2022). Highly Fluorescent Dyes Containing Conformationally Restrained Pyrazolylpyrene (Pyrazoolympicene) Chromophore. Molecules, 27(4), 1272.

Wood, T. E.; Thompson, A. (2007). Advances in the chemistry of dipyrrins and their complexes. Chem. Rev., 107, 1831.

Yariv, E.; Schultheiss, S.; Saraidarov, T.; Reisfeld, R. (2001). Efficiency and photostability of dye-doped solid-state lasers in different hosts. Opt. Mater. 16, 29.

Zhang, D., Martin, V., Garcia-Moreno, I., Costela, A., Perez-Ojeda, M. E., Xiao, Y. (2011). Development of excellent long-wavelength BODIPY laser dyes with a strategy that combines extending p-conjugation and tuning ICT effect. Phys. Chem. Chem. Phys., 13, 13026–13033.

Zlatić, K.; Ben El Ayouchia, H.; Anane, H.; Mihaljević, B.; Basarić, N.; Rohand, T. (2020). Spectroscopic and photophysical properties of mono- and dithiosubstituted BODIPY dyes. Journal of Photochemistry and Photobiology A: Chemistry, 388, 112206.

THE ROLE OF SUPERCONDUCTING MATERIALS IN TRANSPORTATION: CURRENT RESEARCH AND FUTURE PROSPECTS

Murat ABDIOGLU[1]

Ufuk Kemal OZTURK[2]

1. INTRODUCTION

As our world grows with more people and denser cities, the need for fast, reliable and environmentally friendly transportation has never been more important. The high-speed transportation systems, as one of the most important actors of this technological revolution, have the power to change our lifestyles, working preferences, interconnections between people, etc. The high-temperature superconductors (HTS), that could break down the barriers that hinder the speed and efficiency of our transportation networks can be located at the centre of this transformation.

Why is high-speed transportation so important? It's not just about making our lives more comfortable; it's also a game-changer for economic development. Fast and efficient transportation not only transports people and goods; it connects communities and opens new possibilities for collaboration and

---

[1] Assoc. Prof., Department of Mathematics and Science Education, Faculty of Education, Bayburt University, 69000, Bayburt, Türkiye, muratabdioglu61@gmail.com, ORCID: 0000-0002-5497-0817.

[2] Prof., Electromagnetic Guidance and Acceleration Research Group (EMGA), Department of Physics, Faculty of Science, Karadeniz Technical University, 61080, Trabzon, Türkiye, kozturk6167@gmail.com, ORCID: 0000-0002-8847-1880.

growth. It also represents an important player in the fight against climate change and offers a greener alternative to traditional means of transportation.

Now let's go back and explore the historical journey of high-speed transportation. Imagine yourself in the early 19th century, when steam locomotives emerged that changed the face of road travel. The 27th of September 1825 was the day the first train ran in England by Stockton and Darlington Railway company [1]. Figure 1 illustrates a drawing of gathered people to see this fantastic vehicle. The first locomotive, named Locomotion No. 1, had reached the maximum speed of 19 km/h. Over time, we saw that the transition from steam trains to electric trains pushed the limits of speed. Then, magnetic levitation (maglev) systems emerged, adding a futuristic touch to our quest for speed.

However, the conventional Maglev systems use traditional materials like copper and aluminium [2] which are holding us back, limiting efficiency and speed. The discovery of high-temperature superconductors (HTS) in the late 20th century [3] opened a new way to take the Maglev systems to a further point. This advancement promised us better energy efficiency, lower maintenance costs and better performance for high-speed applications. The Maglev systems are not the only transportation system that benefits from the HTSs. Increasing investigations on electric motors and generators enlarged the application area of HTS materials from Maglevs to full-electric aircraft [4, 5].

Figure 1. Picture of Gathered People to Witness the Opining of the Stockton and Darlington Railway [1]

Opening of the Stockton and Darlington Railway in 1825.
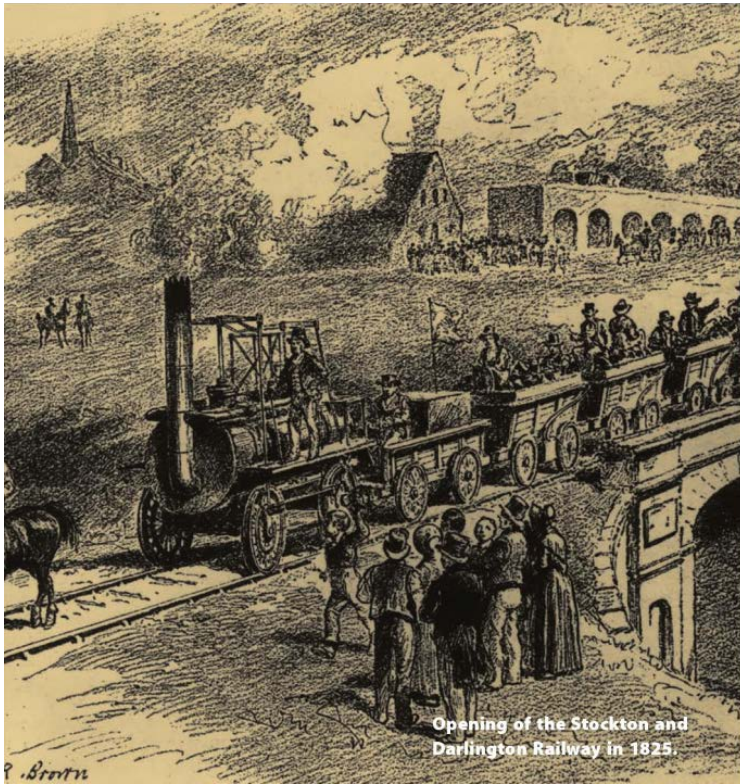
As we handle this work in detail, our mission is to evaluate the current state of research on how HTSs could join forces with transportation systems. We don't just look at interesting developments; we also address the challenges and shed light on what the future holds. We take a deep dive into existing key technologies and exciting ongoing projects to show how HTSs are important in driving our transportation networks towards a faster, greener, and more connected future. The remainder of this chapter is structured as follows: Section 2 and Section 3 outline the Maglev systems and current developments in superconducting Maglev systems, respectively. Section 4 represents the current studies on fully HTS motorized aircraft, and Section 5 offers the concluding insights.

2. MAGNETIC LEVITATION TRANSPORTATION SYSTEMS

Magnetic levitation (Maglev) transport systems represent the leading paradigm of transport technology, based on the revolutionary concept of contactless movement of trains. Harnessing the power of magnetic forces, these systems move trains with remarkable efficiency and safety, completely eliminating the need for traditional wheel-rail contact. This forward-thinking approach not only challenges the limitations of traditional means of transportation, but also promises unparalleled speed smoothness, and precision in the movement of trains. The essence of Maglev lies in its ability to float seamlessly above the railway track, thus opening up a new era of transportation that overcomes the friction and wear limitations associated with traditional rail systems.

Maglev transportation systems can be categorized based on their speed, including low-speed maglev trains (up to 120 km/h), medium-speed maglev trains (around 200 km/h), and high-speed maglev trains (exceeding 400 km/h) [6]. On the other hand, Maglev systems can be broadly classified into two main types: electromagnetic levitation (EML), and electrodynamic levitation (EDL) as illustrated in Figure 2. In some cases, the Inductrack is classified separately, but it is more reasonable to handle it within the EDL. In addition, it should be noted that sometimes suspension term is preferred instead of levitation. All the mentioned systems utilize magnetic forces to suspend and propel the train, but they employ different principles to achieve this.

Figure 2. Schematic Illustration of Three Different Maglev Techniques [7]

Electromagnetic Levitation (EML)   Electrodynamic Levitation (EDL)   Inductrack
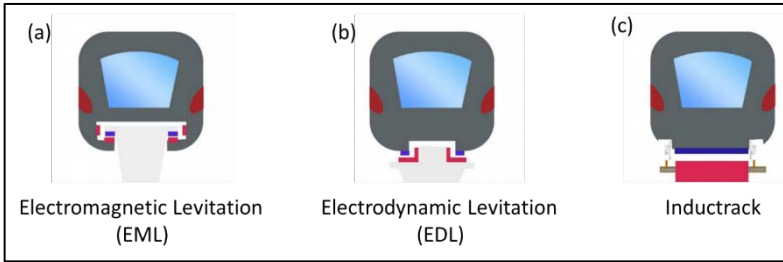
Electromagnetic Levitation (EML): EML systems use electromagnets along the track and on the train itself. The track-mounted electromagnets are energized to create a magnetic field, and the train's magnets, in turn, respond to these fields. By adjusting the strength of the electromagnetic fields, the train is suspended and propelled above the track. Basically, EML system is based on magnetic attraction. These systems are capable of levitating at lower speeds (even in zero speed) compared to EDL systems. The commercially operational Shanghai Maglev Train shown in Figure 3(a) is an example of an EML Maglev system. The working principle of this train is schematized in Figure 3(b). The Transrapid Maglev system was constructed in 2004 and can reach a top speed of 431 km/h over a line of 30.5 km. Although EML systems mostly benefit from the electromagnets, some research and development have been performed by using superconducting materials in these systems [8, 9].

Electrodynamic Levitation (EDL): EDL systems employ magnets on the train and normal conducting coils (or conducting plate) on the track. The magnets in these systems can be superconducting magnet (SCM) or permanent magnets (PMs). The main difference between EML and EDL is the magnetic interaction method between the onboard unit and the track. EDL system benefits from magnetic repulsion, while EML, on the contrary, uses magnetic attraction. EDL systems are known for

their high-speed capabilities and lower energy consumption compared to EML systems. The most well-known examples of EDL systems using SCMs or PMs are SC-Maglev [10] and Inductrack [11] systems, respectively. SC-Maglev system has been developed by Japan Railway Company. In this system, as the train moves, a changing magnetic field induces currents in the superconducting magnets, creating opposing magnetic fields that result in levitation.

Figure 3. Transrapid Electromagnetic Levitation System. (a) Photo of the Shanghai Transrapid Maglev System, and (b) Schematic Illustration of Operation Principle [6].
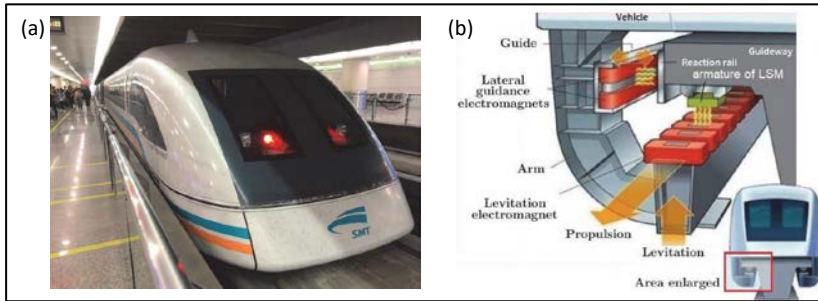
The other EDL system, Inductrack, employs PMs on the vehicle and non-ferromagnetic conducting plates on the track. This system was firstly proposed by Post and Ryutov who were the researchers at the Lawrence Livermore National Laboratory, California, USA [11]. The Inductrack EDL system is characterized by its simplicity, efficiency, and low energy consumption and relies on the principles of electromagnetic induction to achieve levitation and propulsion. In the case of the Inductrack system, the base of the vehicle is equipped with a series of PMs arranged in a Halbach array configuration, as schematically illustrated in Figure 4. A Halbach array is a special arrangement of PMs that enhances the magnetic field on one side while cancelling it out on the other [12]. As the maglev vehicle moves over the conducting track, the changing magnetic field induces eddy currents (circulating currents) in the conductive

material of the track, typically made of aluminium. These eddy currents generate their own magnetic fields, and according to the Lenz's law, the direction of these fields opposes the original change in magnetic flux. The interaction between the PMs in the vehicle and the induced magnetic field in the track creates a repulsive force, leading to levitation. The strength and configuration of the PMs, as well as the design of the conductive elements in the track, are carefully engineered to optimize the levitation effect.

Figure 4. Schematic Illustration of Inductrack EDL System.
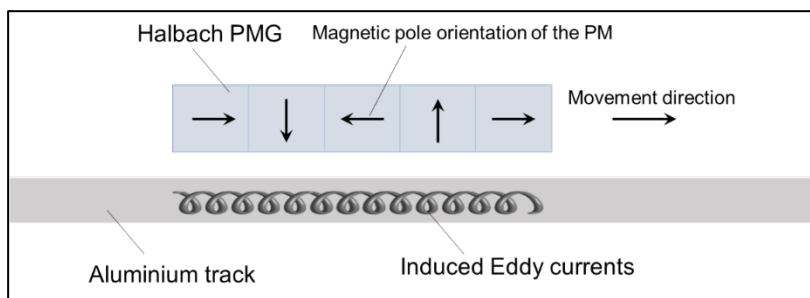
3. SUPERCONDUCTING MAGLEV

Superconducting maglev systems represent a revolutionary breakthrough in magnetic levitation technology and offer unprecedented advantages for high-speed transport. Superconducting materials are at the heart of these systems, which exhibit extraordinary properties when cooled below a critical temperature. Using superconductors in magnetic levitation technology improves efficiency, stability and overall performance, revolutionising the transport infrastructure landscape.

The main advantage of using superconducting materials in maglev systems is the phenomenon of zero electrical resistance and magnetic flux leakage, properties unique to

superconductivity. When cooled below their critical temperature, superconductors can conduct electricity without losing energy due to resistance. This property makes it possible to generate strong and persistent magnetic fields and forms the basis for highly efficient and stable levitation and propulsion systems of maglev trains.

The preferred superconducting material for these systems is typically a type II superconductor, often a compound featuring elements such as yttrium, barium, copper, and oxygen (YBCO). The other most common Type II superconductor is Nb-Ti which is currently used in SC-Maglev (Figure 5). Type II superconductors possess the capability to trap magnetic flux, allowing them to sustain superconducting properties even when subjected to an applied magnetic field. This attribute is pivotal for the reliable levitation and guidance of maglev vehicles. On the other hand, these materials have high current carrying capacity and bigger critical field. These properties make them stand out since are required for high-speed transportation systems.

Superconducting Maglev transportation systems offer numerous advantages:

Zero energy loss: The absence of electrical resistance against DC transport current ensures minimal energy loss during current flow, resulting in extremely energy efficient systems.

Increased stability: Superconducting materials create robust and stable magnetic fields that enable reliable levitation and guidance of maglev trains, especially at high speeds.

High propulsion efficiency: The persistent magnetic fields generated by superconductors enable efficient propulsion of maglev trains and contribute to enhanced acceleration and deceleration.

Reduced maintenance: The lack of wear and tear associated with friction in conventional track systems reduces the need for frequent maintenance, contributing to a longer service life.

Quiet operation: Maglev trains with superconducting technology operate quietly because they do not rely on physical contact between train and rail, making them suitable for a variety of environments.

High-Speed Capabilities: Superconducting maglev trains are ideal for high-speed transport and offer the opportunity to significantly reduce journey times compared to conventional modes of transport.

Although research and development on superconducting maglev systems have been conducted all over the world, none of these are used in daily life for now. The most well-known and the nearest to the commercial usage of one of these systems is SC-Maglev, which the Central Japan Railway Company is developing [13]. The running principle and actual photo of this system is given in Figure 5.

SC-Maglev system employs superconducting magnets in the moving body as a magnetic field source. These magnets are made up of Nb-Ti coils. The side walls of the track are paved by two sets of coils made up of normal conducting materials, one of which is an ordinary circular shape, and the other is 8-shaped null-flux coils. The guidance and levitation of the train are provided by the interaction of the SC magnets inside the train with 8-shaped coils on the track, while circular-shaped coils are used for propulsion. As indicated in Section 2, SC-Maglev system relies on EDL principle. Therefore, it needs to reach a certain speed to be levitated and this is achieved by conventional wheels mounted under the train. The train levitates after reaching about 145 km/h,

and the wheels retract. The maximum operation speed of this train is measured as 500 km/h.

Figure 5. The Running Principle (a) and Actual Photo (b) of the SC-Maglev System in Japan [14].
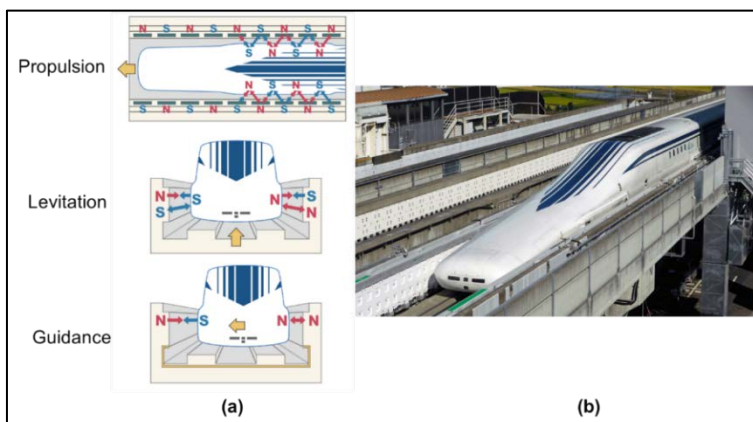
The SCMs are used in SC-Maglev system constructed by Nb-Ti superconducting wires with a critical temperature value of about 10 K. On the other hand, there are also studies in the literature that have focused on employing bulk formed HTS materials in Maglev systems. As partly mentioned in Section 1, HTS materials are known for their higher critical current density, critical magnetic field value, and magnetic flux trapping ability [15, 16]. In addition, cooling these materials down to their critical temperature (about 93 K) is very easy as compared to Nb-Ti wires since this can be achieved by liquid nitrogen (LN2). Nitrogen gas is composed of 78 % of the Earth's atmosphere, and it is liquified at the temperature of 77 K, meaning it is not hard to produce and store.

The studies on HTS Maglev systems ranges from laboratory scale [17-20] to prototype of real-scale systems [21-23]. A research team in Federal University of Rio de Janeiro, Brazil have constructed a 200 m test line in the University campus as seen in Figure 6. They conducted a comprehensive study on

this full-scale Maglev system, named Maglev-Cobra, incorporating both experimental and modelling investigations [21]. The modelling phase utilized two superconductor lines consisting of infinitely long superconductors, while experimental trials employed an arrangement of three-seeded YBCO superconductors. The study employed three different PMG arrangements as the source of the magnetic field. The results indicated that the model used was consistent with the experimental findings. In another study by the same research group [24], they designed and tested the real-scale Maglev vehicle, as depicted in Figure 6. The researchers highlighted the key advantages of Maglev-Cobra, including low energy consumption, minimal noise pollution, a curvature radius of 45 m, and the capability to ascend a 15% inclined ramp. The vehicle used a linear induction motor for traction power (Figure 6d), achieving a force of 2500 N at a gap of 8 mm between onboard unit including superconductors and the PMG path.

Figure 6. Maglev-Cobra Levitation System. (a) Maglev Vehicle on the Path, (b) Close View of the Levitation Gap, (c) 200 m Test Line in the University Campus, and (d) the Linear Induction Motor with Two Short Primaries [21, 24].
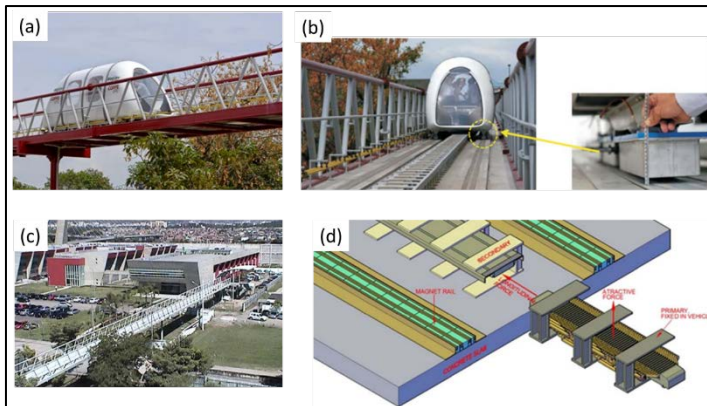
The researchers on the Southwest Jiaotong University in China which developed the first manned Maglev vehicle

prototype in 2000, tested the Maglev vehicle on a dual-rail track named "Super-Maglev" in 2016 (Figure 7) [22]. The Maglev vehicle is designed to be 2.2 meters in length, 1.1 meters in width, and to move over a gap of 10-20 mm. The PMG track is 45 meters long with a track gauge of 0.77 meters, has a race-track shape with a curvature radius of 6 meters. The vehicle's movement is facilitated by a linear induction motor, reaching a maximum speed of 50 km/h. Throughout the vehicle's motion, parameters such as the gap between the Maglev vehicle and the track, levitation force, speed, acceleration, lateral guidance, position, and total travel distance were recorded in real-time. Transportation within a vacuum tube (Evacuated Tube Transportation, ETT) significantly reduces air friction, and when combined with Maglev technology, it can also eliminate wheel-rail friction. In order to realize this revolutionary concept, researchers modified the "Super-Maglev" system and developed a 45-meter-long HTS Maglev-ETT system as shown in Figure 7 (c)-(d) [25]. The system essentially consists of three parts: a HTS Maglev vehicle-track system with a 1-ton loading capacity and 10 mm operational gap; a 45-meter-long, vacuum-sealed, race-track-shaped tube with a 2-meter diameter; a linear induction motor. The pressure inside the tube can be reduced to 2.9 kPa. Experimental results showed a significant reduction in air resistance on the vehicle within the low air pressure inside the tube.

Figure 7. Super-Maglev HTS Magnetic Levitation System in China. (a) General View of 45 Meters Long Magnetic Rail, (b) Photo of the 2nd Generation Maglev Vehicle, (c) Schematic Illustration of the ETT Tube, and (d) Panoramic View of the ETT-Maglev Tube [22, 25].
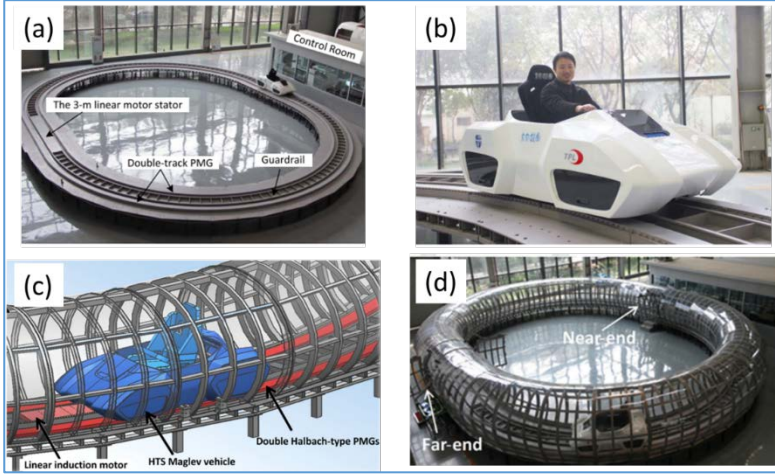
4. FULLY HTS MOTORIZED AIRCRAFT

The world population, which has increased from 6.3 billion to 7.8 billion in the last twenty years [26], is accompanied by a rapid rise in energy consumption. In addition to the direct energy consumed by the growing human population for heating and lighting, there is a simultaneous increase in indirectly consumed energy resulting from transportation needs such as tourism, business, health-related travels, and the transport of goods necessary to fulfil requirements like food and clothing. The continual increase in energy consumption poses a significant threat to the future of our planet, leading to the depletion of energy resources, primarily reliant on fossil fuels, and an increase in carbon dioxide emissions into the atmosphere.

Despite ongoing efforts in researching environmentally friendly energy sources, the majority of the world's energy needs

are still met by fossil fuels, largely due to the fact that the installation costs of renewable energy plants have not yet decreased enough to enable widespread adoption. While electric motors, particularly gaining momentum in the automotive industry, seem eco-friendly as they do not emit carbon dioxide, The World Bank data reveals that 65.2% of the world's total electricity production comes from oil, gas, and coal [27].

Given this scenario, it becomes crucial to focus not only on researching eco-friendly energy sources but also on developing transportation systems that are both energy-efficient and high-speed. Following the development of the first superconducting Maglev vehicle for human transport [22], research on Maglev systems has gained momentum as mentioned above. Simultaneously, academic research [28] and commercial applications [29] are being conducted on hyperloop systems based on Maglev technology. Although hyperloop systems theoretically claim speeds of around 1200 km/h, practical challenges such as health concerns due to acceleration forces required for high speeds over short distances and difficulties in maintaining a low-pressure environment within the tube pose obstacles to their widespread use.

In the context of intercontinental passenger and cargo transportation, air travel takes precedence, and especially for cargo transportation, sea transport becomes prominent. Therefore, as mentioned earlier, the global energy problem and the environmental pollution caused by fossil fuels used in both transportation and electricity production call for the development of energy-efficient, eco-friendly, and high-power-density ship and aircraft engines.

In recent years, the exploration of HTS materials has opened up exciting possibilities in various technological applications, including transportation. One particularly

intriguing avenue is the integration of fully HTS motorized systems in all-electric aircraft. This represents a groundbreaking shift in aviation technology, leveraging the unique properties of HTSs to enhance the efficiency, performance, and sustainability of air travel. In this subsection, we introduced the studies on and developments in the next-generation superconducting motors with high power density for all-electric aircraft. Superconducting machines, being significantly more power-dense and efficient than traditional copper-based motors, are being developed by several research groups worldwide. The first commercial low-temperature superconductor (LTS) generator was developed by Westinghouse in 1978 to enhance the performance of large turbine generators [30]. General Electric later developed a high-speed superconducting generator in 1982 [31]. In 1999, the Japanese Super-GM company tested a 70 MW generator using NbTi LTS wires for three different rotor windings [32].

NASA has initiated a project to develop technologies for a fully electric aircraft, supporting research in areas such as noise, emissions, and safety to enhance aircraft performance. As part of a project supported by NASA, a study was conducted to design a HTS motor for use in electric aircraft, aiming to achieve high power density [33]. The presented configuration in the study is a synchronous motor with a non-traditional topology developed with bulk HTS material. The designed motor has a total mass of 28 kg, a rotation speed of 2700 rpm, and a power of 220 horsepower (164 kW). The study results indicate that the use of superconducting motors in aircraft is feasible, leading to a significant increase in payload capacity and a substantial reduction in pollutant emissions. The traditional motor of a Cessna 172 aircraft for four people has a mass of 160 kg, whereas the motor presented in this study, with a mass of 30 kg, provides higher propulsion power using an approximately 60 kg cryo-cooler than the Cessna 172 motor.

Figure 8 illustrates the N3-X aircraft developed by NASA [34]. This aircraft employs hybrid laminar flow body technology, enabling it to achieve a high lift-to-drag ratio and allowing distributed electric fans to handle significant amounts of thick upper body boundary layer flow. This structure significantly reduces fuel consumption and noise. The electric transmission system consists of superconducting motors, superconducting transmission cables, cryogenic (yet non-superconducting) inverters, and rectifiers connected to generators. The propulsion performance parameters of the aircraft, designed using BSCCO and MgB2 superconducting materials, have been examined in the design of this system.

Figure 8. N3-X Vehicle Developed by NASA Employing Superconducting "Turboelectric Distributed Propulsion (TeDP)" System [34].
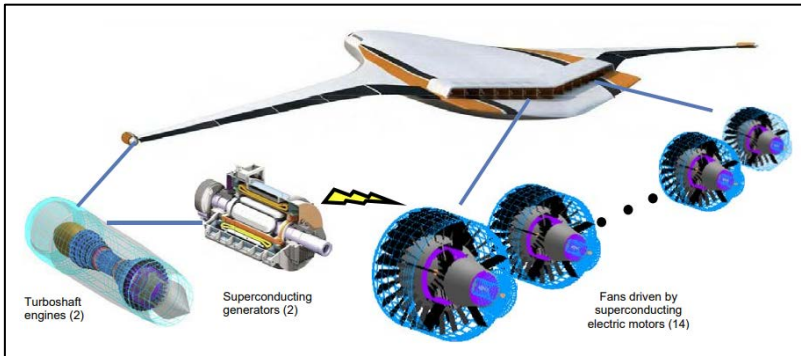
5. CONCLUSION

This chapter aimed to investigate the pivotal role of superconducting materials in revolutionizing transportation, with a focus on high-speed systems such as Maglev trains and fully HTS motorized aircraft. The escalating demands of a growing global population and increasingly dense urban environments underscore the pressing need for transportation that is not only

fast and reliable but also environmentally sustainable. Recognizing high-speed transportation systems as transformative agents in our technological landscape, this chapter explores how high-temperature superconductors (HTS) can serve as a catalyst for overcoming existing barriers and enhancing the speed and efficiency of transportation networks.

Our objective is to delve into the historical progression of high-speed transportation, starting from the era of steam locomotives to the emergence of electric trains and Maglev systems. Against this backdrop, we introduce the concept of HTS and its potential to redefine the capabilities of transportation systems. The discussion unfolds by categorizing magnetic levitation transportation systems into electromagnetic levitation (EML) and electrodynamic levitation (EDL), elucidating the distinctive advantages and applications of each.

The narrative then shifts towards a detailed exploration of superconducting Maglev systems, spotlighting their unique features, including zero electrical resistance, magnetic flux trapping, and high-speed capabilities. Emphasis is placed on the SC-Maglev system as a notable example of how superconducting materials contribute to efficiency, stability, and reduced maintenance in high-speed rail transport. Continuing our exploration, we extend the application of superconducting materials to fully HTS motorized aircraft. The chapter addresses the escalating global energy consumption and the imperative for energy-efficient, eco-friendly, and high-power-density engines in air travel. We examine how the integration of HTS materials in all-electric aircraft represents a paradigm shift in aviation technology, illustrated through NASA's project on a fully electric aircraft.

In essence, this chapter endeavours to provide a comprehensive understanding of the current research landscape

and the potential future advancements afforded by superconducting materials in shaping a faster, greener, and more interconnected future for transportation systems. As a conclusion, the application of HTS materials in transportation systems not only ensures minimal energy loss, increased stability, and high propulsion efficiency but also reduces maintenance, leading to longer service life. Moreover, as exemplified in fully HTS motorized aircraft, these materials contribute to the development of energy-efficient, eco-friendly, and high-power-density engines, revolutionizing air travel. The integration of HTS materials in transportation represents a crucial step towards achieving faster, greener, and more connected modes of travel, addressing the evolving demands of a rapidly growing global population and the imperative for sustainable transportation solutions.

REFERENCES

[1]   Kirby, M. W., & Kirby, M. W. (2002). The origins of railway enterprise: the Stockton and Darlington railway 1821-1863. Cambridge University Press.

[2]   Lee, H. W., Kim, K. C., & Lee, J. (2006). Review of maglev train technologies. IEEE transactions on magnetics, 42(7), 1917-1925.

[3]   Müller, K. A., & Bednorz, J. G. (1987). The discovery of a class of high-temperature superconductors. Science, 237(4819), 1133-1139.

[4]   Weng, F., Zhang, M., Lan, T., Wang, Y., & Yuan, W. (2020). Fully superconducting machine for electric aircraft propulsion: Study of AC loss for HTS stator. Superconductor Science and Technology, 33(10), 104002.

[5]   Masson, P. J., Soban, D. S., Upton, E., Pienkos, J. E., & Luongo, C. A. (2005). HTS motors in aircraft propulsion: Design considerations. IEEE transactions on applied superconductivity, 15(2), 2218-2221.

[6]   Gieras, J. F. (2020). Ultra high-speed ground transportation systems: Current Status and a vision for the future. Organ, 9, 20.

[7]   Rümeysa, Ö., & Yasin, Ç. M. (2021). Comparison of hyperloop and existing transport vehicles in terms of security and costs. Modern Transportation Systems and Technologies, 7(3), 5-29.

[8]   Zhang, G., Fang, Y., Song, F., Zhu, G., & Wang, Z. (2004). Optimal design and FEM analysis of the superconducting magnets of EMS-MAGLEV models using Bi-2223 tapes. IEEE transactions on applied superconductivity, 14(2), 1850-1853.

[9]   Tsuchiya, M., & Ohsaki, H. (2000). Characteristics of electromagnetic force of EMS-type maglev vehicle using bulk superconductors. IEEE transactions on magnetics, 36(5), 3683-3685.

[10]   Uno, M. (2016). Chuo shinkansen project using superconducting maglev system. Japan Railway & Transport Review, 68, 14-25.

[11]   Post, R. F., & Ryutov, D. D. (2000). The inductrack: A simpler approach to magnetic levitation. IEEE Transactions on applied superconductivity, 10(1), 901-904.

[12]   Halbach, K. (1985). Application of permanent magnets in accelerators and electron storage rings. Journal of Applied Physics, 57(8), 3605-3608.

[13]   Kusada, S., Igarashi, M., Nemoto, K., Okutomi, T., Hirano, S., Kuwano, K., ... & Yamaji, M. (2007). The project

overview of the HTS magnet for superconducting maglev. IEEE Transactions on Applied Superconductivity, 17(2), 2111-2116.

[14] https://global.jr-central.co.jp/en/company/_pdf/superconducting_maglev.pdf.

[15] Abdioglu, M., Guner, S. B., Ozturk, K., Yang, C., Chen, I., & Celik, S. (2022). Magnetic levitation force and trapped field properties of multiseeded YBCO with triangular arrangement of seeds. International Journal of Applied Ceramic Technology, 19(1), 459-466.

[16] Savaskan, B., Guner, S. B., Yamamoto, A., & Ozturk, K. (2020). Trapped magnetic field and levitation force properties of multi-seeded YBCO superconductors with different seed distance. Journal of Alloys and Compounds, 829, 154400.

[17] Guner, S. B., Celik, S., & Tomakin, M. (2017). The investigation of magnetic levitation performances of single grain YBCO at different temperatures. Journal of Alloys and Compounds, 705, 247-252.

[18] Abdioglu, M., Ozturk, K., Ekici, M., Savaskan, B., Celik, S., & Cansiz, A. (2021). Design and experimental studies on superconducting maglev systems with multisurface HTS–PMG arrangements. IEEE Transactions on Applied Superconductivity, 31(6), 1-7.

[19] Yang, W., Zhao, P., Yan, J., Liu, Z., Hu, J., Deng, F., & Tang, H. (2022). Translational levitation of a permanent magnet above the splicing plane of superconducting blocks under zero field cooling and its motion drag. Engineering Research Express, 4(3), 035052.

[20] Bernstein, P., Xing, Y., & Noudem, J. G. (2022). Increased levitation force in a stable hybrid superconducting magnetic levitation set-up. Engineering Research Express, 4(4), 045008.

[21] Mattos, L. S., Rodriguez, E., Costa, F., Sotelo, G. G., De Andrade, R., & Stephan, R. M. (2016). MagLev-Cobra operational tests. IEEE Transactions on applied superconductivity, 26(3), 1-4.

[22] Deng, Z., Zhang, W., Zheng, J., Ren, Y., Jiang, D., Zheng, X., ... & Deng, C. (2016). A high-temperature superconducting maglev ring test line developed in Chengdu, China. IEEE Transactions on Applied Superconductivity, 26(6), 1-8.

[23] Schultz, L., de Haas, O., Verges, P., Beyer, C., Rohlig, S., Olsen, H., ... & Funk, U. (2005). Superconductively levitated transport system-the SupraTrans project. IEEE Transactions on Applied Superconductivity, 15(2), 2301-2305.

[24] Sotelo, G. G., Dias, D. H. N., de Andrade, R., & Stephan, R. M. (2010). Tests on a superconductor linear magnetic bearing of a full-scale MagLev vehicle. IEEE Transactions on Applied Superconductivity, 21(3), 1464-1468.

[25] Deng, Z., Zhang, W., Zheng, J., Wang, B., Ren, Y., Zheng, X., & Zhang, J. (2017). A high-temperature superconducting maglev-evacuated tube transport (HTS Maglev-ETT) test system. IEEE Transactions on Applied Superconductivity, 27(6), 1-8.

[26] The World Bank. (2023). Population, total-World. Retrieved from https://data.worldbank.org/indicator/SP.POP.TOTL?locations=1W.

[27] The World Bank. (2023). Electricity production from oil, gas, and coal sources (% of total). Retrieved from https://data.worldbank.org/indicator/EG.ELC.FOSL.ZS.

[28] Kumar, V. A., Prajwal, G., Khan, F., Kapai, C., & Varun, N. (2020). Design and Development of Hyperloop Train. Int. J. Res. Eng. Sci. Manag, 3, 235-238.

[29] Virgin. (2023). How does Virgin Hyperloop work? Retrieved from https://www.virgin.com/about-virgin/latest/how-does-virgin-hyperloop-work

[30] Design, S. G. (1977). prepared by Westinghouse Electric Corporation for EPRI. Report EPRI EL-577, Project RP429.

[31] Gamble, B. B., & Keim, T. A. (1982). High-power-density superconducting generator. Journal of Energy, 6(1), 38-44.

[32] Yamaguchi, K., Takahashi, M., Shiobara, R., Taniguchi, T., Tomeoku, H., Sato, M., ... & Kusafuka, H. (1999). 70 MW class superconducting generator test. IEEE Transactions on applied superconductivity, 9(2), 1209-1212.

[33] Masson, P. J., & Luongo, C. A. (2005). High power density superconducting motor for all-electric aircraft propulsion. IEEE Transactions on Applied Superconductivity, 15(2), 2226-2229.

[34] Kim, H. D., Felder, J. L., Tong, M. T., Berton, J. J., & Haller, W. J. (2014). Turboelectric distributed propulsion benefits on the N3-X vehicle. Aircraft Engineering and Aerospace Technology: An International Journal, 86(6), 558-561.

MAGNETIC LEVITATION FORCE MEASUREMENT SYSTEMS AND TECHNIQUES FOR SUPERCONDUCTING MAGLEV SYSTEMS

Ufuk Kemal OZTURK[1]

Murat ABDIOGLU[2]

1. INTRODUCTION

In the dynamic environment of transportation innovation, magnetic levitation (Maglev) systems have emerged as a model for technological advancement based on the unique properties of superconducting (SC) materials. This chapter comprehensively examines a critical dimension of Maglev systems: the precise measurement and understanding of magnetic levitation forces. The first part of this journey aims to provide a comprehensive introduction that forms the basis for an in-depth study of force measurement techniques in superconducting magnetic levitation systems. While our primary objective is not to delve deeply into the nature of superconductivity, we believe that a brief introduction would prove beneficial in providing readers with insight. This introductory overview aims to enhance clarity regarding superconducting magnetic levitation, ultimately directing the reader's interest towards the subsequent sections of the chapter. The reader can easily reach deeper information about

---

[1] Prof., Electromagnetic Guidance and Acceleration Research Group (EMGA), Department of Physics, Faculty of Science, Karadeniz Technical University, 61080, Trabzon, Türkiye, kozturk6167@gmail.com, ORCID: 0000-0002-8847-1880.

[2] Assoc. Prof., Department of Mathematics and Science Education, Faculty of Education, Bayburt University, 69000, Bayburt, Türkiye, muratabdioglu61@gmail.com, ORCID: 0000-0002-5497-0817.

the superconductivity and superconducting levitation on the refs [1,2].

Basically, superconductivity can be explained as a remarkable phenomenon in certain materials where, when cooled below a critical temperature (T_c), they exhibit zero DC electrical resistance. This means that electric currents can flow through these materials without any loss of energy due to resistance. The other unique property of superconducting materials is their ability to expel the magnetic field that they are exposed to. When the temperature of the material is above T_c, the magnetic field enters the interior of the superconductor. Below T_c, and for small magnetic field values, magnetic flux will be expelled from places other than a thin layer near the surface of the superconductor. For sufficiently small values of the magnetic field, this expulsion occurs entirely, and this phenomenon is called the "Meissner effect".

Superconductors are divided into two groups, Type I and Type II, based on their behaviour under an applied magnetic field. Superconducting materials return to their "normal" state when the applied magnetic field exceeds a certain value, named critical field (H_c). This transition is a straightforward process for Type I superconductors, while it is somewhat more complex for Type II superconductors. In the Meissner state, when a superconducting material is exposed to an external magnetic field (H), the expulsion of magnetic flux density (B) from the interior of the superconductor results in the material having a macroscopic magnetization equal in magnitude but opposite in direction to H. This situation persists only until H_c is reached, and superconductivity disappears for Type I superconductors (Figure 1). In Type II superconductors, if the applied field surpasses the lower critical field (H_{c1}), magnetic flux begins to partially penetrate the material in the form of magnetic vortices. In the range between the applied field of H_c and H_{c1}, Type II

superconductors exist in a state known as the "mixed state" or "vortex state". When the applied magnetic field reaches the upper critical field (H_{c2}), magnetic flux completely enters the material, and the superconducting material returns to the "normal" state. This behaviour of Type II superconductors against the applied magnetic field allows them to trap some magnetic field within their structure.

Figure 1. Magnetisation of Type I and Type II Superconductors Under the Applied Magnetic Field of *H*.
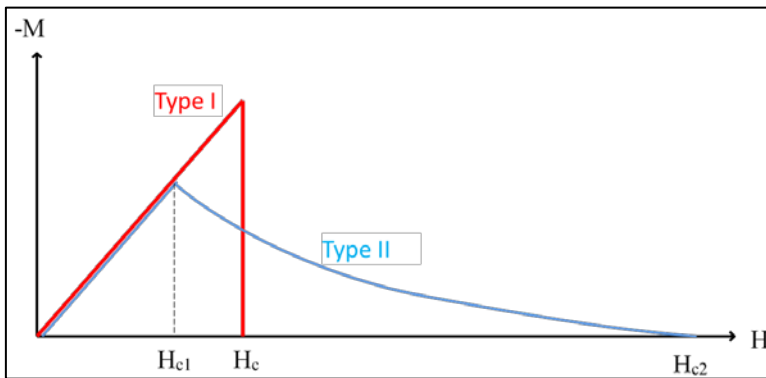
As for magnetic levitation applications, this remarkable interaction between superconductivity and magnetism forms the basis for the efficient and smooth magnetic levitation that is taken advantage of in advanced Maglev transportation systems.

When we look at the historical evolution from traditional transportation to high-speed maglev systems, the paradigm shift in transportation technology becomes clear. Within this development, the integration of superconducting materials plays a central role, not only enabling unprecedented speed and efficiency, but also promising a sustainable and environmentally friendly future for transportation. This chapter addresses the levitation and guidance force measurements, which are essential to optimizing the performance of these state-of-the-art transportation solutions. Magnetic levitation and guidance forces

occur between the magnetic field source and the superconducting unit with respect to vertical and lateral displacements, respectively. These are both critical parameters in Maglev systems since the first is related to the loading capacity while the second is responsible for the movement stability of the system.

The following sections will navigate through the special features of static and dynamic magnetic levitation measurement systems. The aim of these sections is to clarify the methods used to measure the levitation and guidance forces under more complex static and dynamic conditions during operational phases. By addressing these complexities, this chapter aims to provide a comprehensive understanding of the variety in the force measurement to ensure the proper and reliable operation of superconducting maglev systems.

In addition to the technical aspects of force measurement, the unique challenges and developments that arise in the Maglev system prototypes which are close to the real-scale applications and so-called "near-scale" applications are also addressed. This chapter not only highlights the critical point at which these technologies currently find themselves, but also provides insights into the development of superconducting maglev technology.

Essentially, this chapter is intended to be a comprehensive guide that provides a holistic and detailed examination of the force measurement systems and techniques underlying the functionality and potential of superconducting magnetic levitation systems. With this research, we hope to contribute to a broader understanding of these revolutionary transportation systems and pave the way for future advances in this fascinating field. The subsequent sections of this chapter unfold in the following manner: We delved into the static and dynamic magnetic levitation force measurement systems in Sections 2 and 3, respectively. Following that, we handled "Near-Scale"

Superconducting Maglev Systems in Section 4, which are very close to the real-scale practical applications. Lastly, we draw our conclusions.

2. STATIC MAGNETIC LEVITATION FORCE MEASUREMENT SYSTEMS

This section is dedicated to static magnetic levitation force measurement systems. Here, we unravel the methods employed to measure forces when the Maglev system is in a stable, non-operational state. During the static force measurements, the levitation and guidance forces between the magnetic field source and onboard superconducting unit is measured depending on the vertical and lateral displacement. This section provides a detailed exploration of how static forces are precisely measured to ensure the equilibrium and stability of Maglev systems.

Figure 2 illustrates an example of magnetic levitation and guidance force curves. A permanent magnetic guideway (PMG) and a bulk formed YBCO HTS is used in these measurements. In general, the levitation force measurements are conducted in two different cooling conditions of field cooling (FC) and zero field cooling (ZFC). The first indicates the situation where the superconductor is cooled under a magnetic field (i.e., the gap between the PMG and HTS is small). In contrast, in the ZFC condition, the superconductor is cooled without any magnetic field (i.e., the superconductor is far enough from the PMG while cooling). The levitation force measurements are carried out after completely cooing of the HTSs by liquid nitrogen (LN2). After the HTS reaches thermal stability with LN2 (at 77K), the levitation force, in the ZFC condition, is measured with respect to the vertical distance by firstly decreasing the gap between the PMG and HTS from maximum distance to minimum. These movements are indicated as 1 and 2, respectively, in Figure 2. In

the FC condition, the movement is reversed, i.e., firstly, the gap increased from the minimum value to a certain distance that the effect of the magnetic field no longer exists. A typical levitation force measurement curve in the FC condition is given in the inset of Figure 2.

Figure 2. Magnetic Levitation Force (a) and Guidance Force (b) Curves Occur Between a PMG and a YBCO HTS. Inset Figure Shows the Levitation Force Curve in the FC Condition [3].
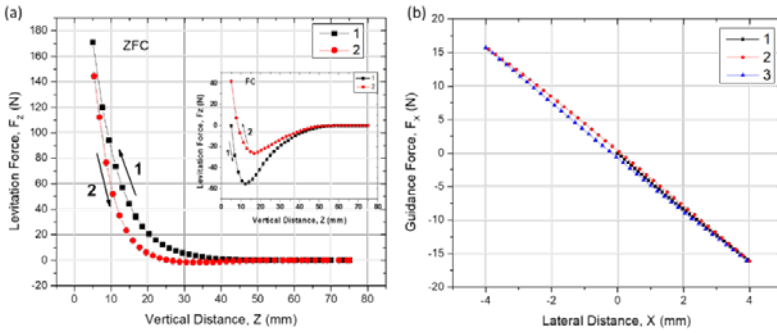
The guidance force is a restoring force against changing the lateral distance between the PMG and HTS units. A typical guidance force curve is given in Figure 2 (b). Similar to the levitation force measurements, after cooling is completed, the guidance force measurement is performed when the lateral distance changes from the central position to a certain value (+x), then to -x and finally to the first position (0). These movements correspond to curves 1, 2, and 3 in Figure 2 (b). The occurrence of a negative force against the first movement indicates the stability of the system. As shown in Figure 2, both the levitation and guidance force curves show hysteretic behaviour because of trapped flux inside the HTS which is an intrinsic character of Type II superconductors. One can see the given levitation and guidance force graphs and more than those with detailed explanations in [3].

Since the magnetic levitation and guidance forces are crucial parameters for superconducting Maglev systems, these are some of the leading research subjects in applied superconductivity. Therefore, researchers worldwide have designed and fabricated some magnetic force measurement systems. In the following of this section, we introduced some of these studies. First studies in this field started by measuring the levitation force and guidance force between a single permanent magnet (PM) and a single HTS [4-6]. The levitation force measurement system given in Figure 3 employs a high precision electronic balance [4]. The HTS sample is placed in an open-topped Styrofoam container on the upper table of the system and cooled by filling this container with LN2 until the HTS was fully immersed in the LN2. Throughout the experiment, the HTS remained submerged in the liquid nitrogen, with additional liquid nitrogen added to the container as necessary. The vertical distance between the HTS and the PMG is changed by a PC controlled servo motor. Force data is collected by the electronic balance connected to a PC. This system is suitable for small HTS samples and single PM, or simple PMG arrangements and it allows to measure small force values about several Newtons. One of the earliest levitation force measurements were conducted by Hull and Cansiz [5]. Their experimental setup include a cylindrical NdFeB PM connected to a strain-gauge force transducer along the x- and z-axes. This assembly is mounted on hand-controlled micrometre stages, allowing for both vertical (z-axis) and horizontal (x-axis) movement at low velocities over a HTS. The cooling of the HTS is provided by the same way given above in [4].

Figure 3. Magnetic Levitation Force Measurement System for Single PM and Single HTS, Designed by Çelik and Öztürk [4].
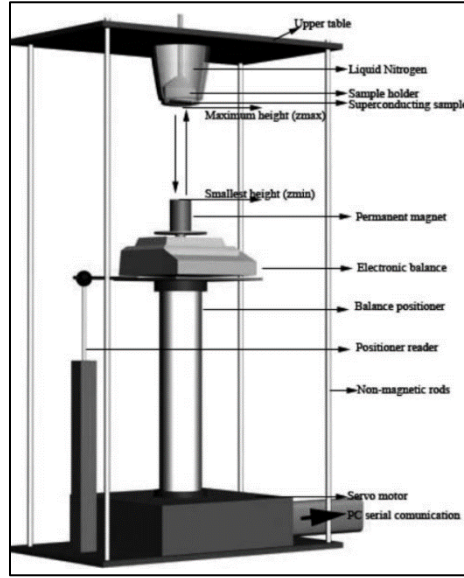
Researchers developed a self-made magnetic levitation force measurement system, the details of which are given in [7]. The apparatus comprises a cantilever beam with a PM fixed at one end, while the sample is submerged in LN2 within a container located beneath the PM. An initial and adjustable distance is set between them based on the desired measurement. The device is capable of measuring the levitation force in both ZFC and FC states. A screw, operated by a PC controlled motor, drives the PM either towards or away from the HTS. The distance is monitored using a displacement sensor, and the levitation force is quantified by a load cell. Continuous recording of both distance and force data signals is accomplished through an x-y recorder. Schematic illustration of this system is given in Figure 4.

Figure 4. Schematic Illustration of the Levitation Force Measurement System: 1. Rotary Handle, 2. Screw Rod, 3. Sliding Glide Mechanism, 4. Displacement Sensor, 5. Moving Board with a Screw Nut, 6. PM, 7. HTS, 8. Container of LN2, 9. Load Cell, 10. Motor, and 11. Base Board [7].
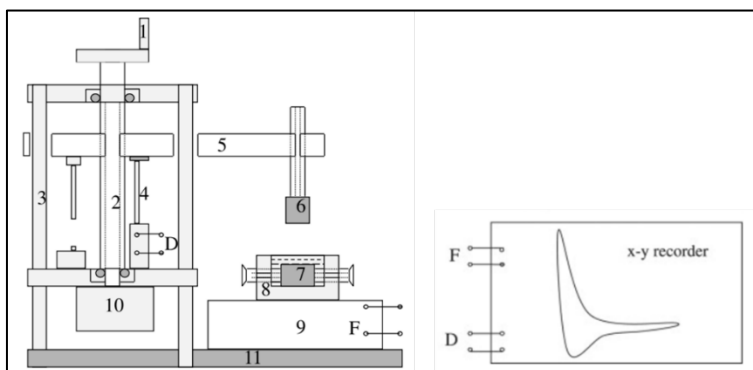
Most magnetic levitation force measurement systems work at LN2 temperatures, restricting the investigation of levitation force properties at cryogenic temperatures. The primary deficiency of this kind of system is that it does not allow levitation force measurements of MgB2 superconductors that have a critical temperature below 40 K. To overcome this restriction, Sukru Celik designed a magnetic levitation force measurement system working at cryogenic temperatures [8]. In this system, measurements encompass vertical force versus vertical motion, as well as lateral and vertical force versus lateral motion. The system provides the capability to measure vertical force versus temperature at a fixed distance between the PM and the SC sample, along with vertical force versus time measurements, spanning temperatures from 20 K to 300 K. These measurements allow for an exploration of temperature dependence, time dependence, and the relationship between distance (magnetic field) and temperature for the SC sample. Additionally, the system offers the capacity for magnetic stiffness (MS) measurements, enabling an examination of MS dependence on

temperature through measurements at various temperatures within the specified range. This measurement setup, covering a broad temperature spectrum, facilitates the characterization of superconductivity properties for superconductors with transition temperatures below that of liquid nitrogen. Although this system can be deemed unique for its ability to measure force parameters at a very broad temperature scale, it only allows measuring the levitation and guidance forces between small SC samples and a single PM.

Researchers in the Applied Superconductivity Laboratory at Southwest Jiaotong University developed their magnetic levitation force measurement system given in [9] and named it "Superconducting Maglev Measurement system (SCML-02) [10]". The schematic illustration and real photo of the SCML-02 system are given in Figure 5. The SCML-02 possesses distinctive features and functionalities, including high measurement precision, the capability to measure both single and multi HTS specimens, simultaneous three-dimensional movement of measured HTS samples and the PM, interchangeability of measurement locations between the HTS specimens and the PM, magnetic levitation force properties measurement between the HTS specimens and either a cylinder PM or a PMG. It allows for real-time independent measurement of levitation force or guidance force during vertical or horizontal movement of the HTSs, respectively. The SCML-02 also enables synchronous measurement of levitation force and guidance force for the HTSs, along with real-time independent measurement of cross stiffness of levitation force or guidance force during vertical or horizontal movement. Additionally, it facilitates the interaction of dynamic rigidity measurement for synchronous levitation force and guidance force. The device also provides measurement of relaxation time for levitation force and guidance force during vertical or horizontal movement. The main technical

specifications of the SCML-02 include a vertical maximal displacement of 150 mm, horizontal maximal displacement of 100 mm, position precision of 0.05 mm, vertical maximal support force of 1000 N with a force precision of 2‰, and horizontal maximal support force of 500 N with a force precision of 1‰.

Figure 5. The design configuration of the SCML-02 measurement system: (a) the frontal perspective of the upper liquid nitrogen container, (b) the lateral view of the lower liquid nitrogen container. The components include: 1) Vertical support post; 2) Vertical force sensor; 3) Force balance chain wheel; 4) Servo motor; 5) Slip set; 6) Upper liquid nitrogen vessel; 7) Lower clamp for cylinder PM or PMG; 8) X-Y electromotion seat; 9) Horizontal force sensor; 10) Upper clamp for cylinder PM or PMG; 11) Lower liquid nitrogen vessel; and 12) Optical bedplate. (c) Real photo of the SCML-02 [10].
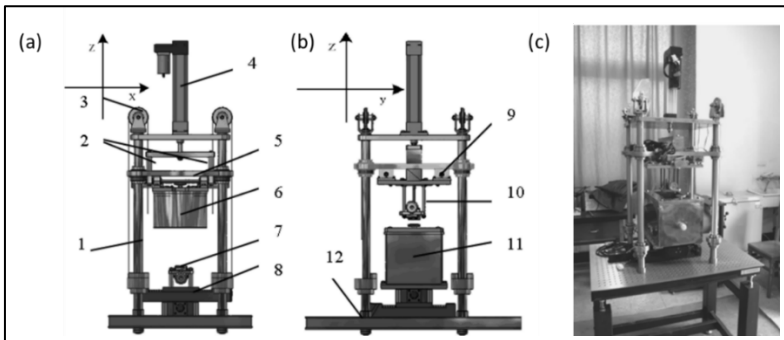
A measurement system was developed by Wen et al. [11] to explore the magnetic levitation properties of HTSs. This system comprises diverse sensors, a 3-D sliding platform, a mechanical drive with automated control, and data acquisition software. The system is characterized by high precision and repeatability, applicable to both PMG and EMG with different shapes. It allows 3-D relative motion between the magnet guideway and HTS bulks. Measurement of levitation force and guidance force of HTS specimens can be done simultaneously or separately, as well as the measurement of their relaxation. The

system facilitates the magnetic field measurements at different levitation gaps and lateral positions of the magnet guideway. It is possible to generate force measurement curves in real-time and record/export the corresponding measurement data. It supports the placement of multiple magnets simultaneously with precisely arranged distances. The system is easy to operate. Key technical specifications include a maximal displacement of 1000 mm on the x-axis, 100 mm on the y-axis, and 500 mm on the z-axis. Position precision is 0.05 mm/m. The vertical and horizontal maximal support forces are 200 N and 30 N, respectively with precisions of $\leq \pm 0.017\%$ and $\leq \pm 0.3\%$. The sliders can reach a speed on the x, y, and z of 1 m/s, while the minimum speed is 0.01 mm/s. Consequently, it enables precise investigation of the magnetic levitation characteristics of an HTS bulk above a magnet guideway and all of its functionalities have been experimentally verified.

Our group in the Department of Physics, at Karadeniz Technical University, Türkiye, developed a three-axis magnetic levitation fore measurement system in 2015 [12] The measurement system (Figure 6) comprises a liquid nitrogen vessel, incorporating YBCOs and auxiliary PMs in certain configurations, various PMG arrays, a data collection and processing unit for force and position, a precision mechanical drive, and a computer control system. Throughout the measurement process, the liquid nitrogen vessel, with a bottom wall thickness of 2 mm, is positioned above the PMG. Operating at liquid nitrogen temperature (77 K), the system is capable of measuring levitation force under both FC and ZFC regimes. To mitigate interference, the FUTEK MTA400 Tri Axial Load Cell was mitigated into the existing system (which originally had three load cells on each axis) [13]. This updated load cell has the capability to measure forces along the x, y, and z axes, with maximum values of 1110 N, 1110 N, and 2220 N, respectively,

and a corresponding sensitivity. The experimental setup is controlled by a Packardbell Imedia 8241 AMD Dual Core 64-bit PC with 3 GB RAM and a 160 GB hard drive. The system control software has been developed using the LabVIEW Graphical Programming Language. Nema 34 flange stepper motors are the chosen components for the three-axis control, with torques of 8.5 N m for the x and y axes and 12.5 N m for the z-axis. Communication between the measurement system and the PC is bidirectional and online, facilitated by the NI-PCI-6010 Low-Cost 16-bit, 200 kS/s DAQ Card. The force data is automatically recorded based on position throughout the x, y, and z axes during the experiment.

Figure 6. The Three-Axis Magnetic levitation force Measurement System Fabricated by Our Group [12, 13].
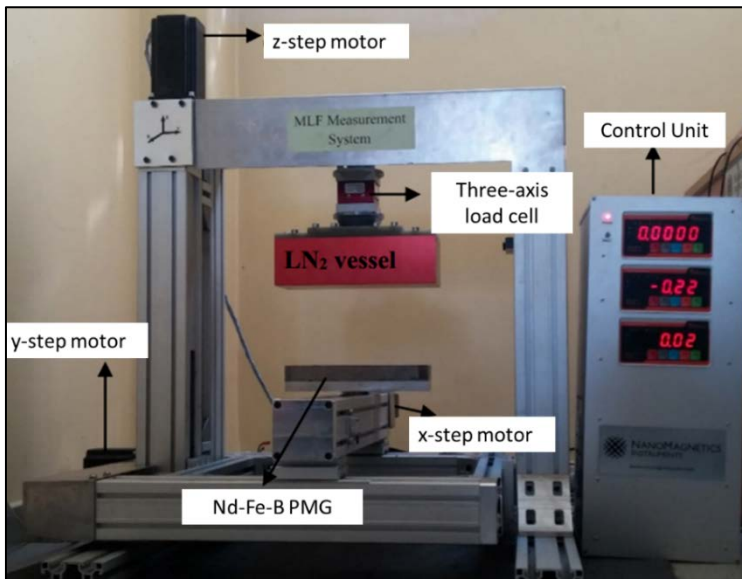
This system allows measuring levitation force, guidance force, magnetic stiffness, levitation and guidance force relaxation. Like almost all levitation force measurement systems, our system allows only single-surface interaction HTS-PMG arrangement force measurements. On the other hand, we offered

a multi-surface HTS-PMG interaction, in our previous studies [3, 14] to increase the loading and guidance performances of Maglev system. With the emergence of this idea, we needed to modify our setup to allow multi-surface interactions and fabricated it as seen in Figure 7. Since the main cost of the HTS Maglev systems comes from the cost of the PMG that has to be paved along thousands of kilometres between the cities, it is reasonable to focus on decreasing the PM number without considerable decrement in loading capacity and movement stability. We thought that this could be achieved by taking advantage of the surfaces of the PMG as much as possible and therefore constructed multi-surface HTS-PMG arrangements. We have obtained a 42.0% reduction in the fabrication cost of the Maglev system for 1000 km magnetic rail without any reduction in levitation force [3]. We also conducted some other studies with different multi-surface arrangements by using the experimental setup showed in Figure 7 [14, 15].

Figure 7. Three Axes Magnetic Levitation Force Measurement System Modified to Allow Multi–Surface HTS-PMG Arrangements. [3].
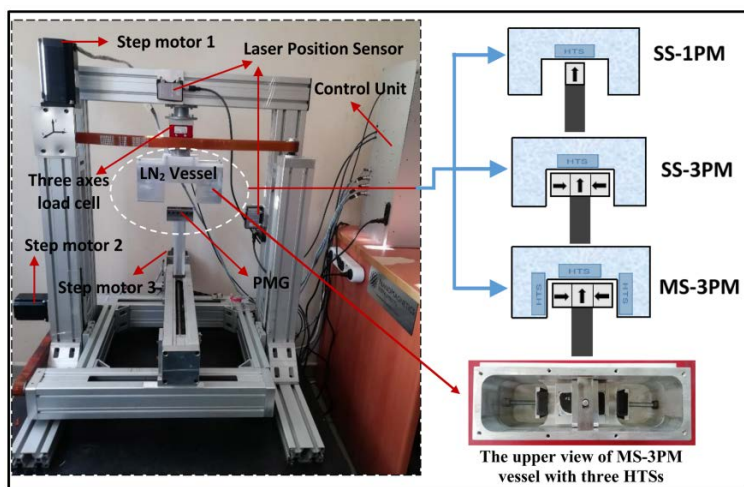
3. DYNAMIC MAGNETIC LEVITATION FORCE MEASUREMENT SYSTEMS

The magnetic levitation measurement systems introduced in the previous section are deemed static levitation force measurement systems since they don't consider the running situations or vibrations of the Maglev vehicle. In this subsection, we introduced the dynamic magnetic levitation force measurement systems exist in the literature.

The dynamic behaviour of HTS Maglev systems is challenging to determine on straight-line paths since it needs very long test tracks. Therefore, constructing circular test systems based on the equivalence principle is reasonable. Researchers at the Applied Superconductivity Laboratory of Southwest Jiaotong University in China developed an HTS Maglev dynamic measurement system (SCML-03) to determine the dynamic characteristics of the HTS Maglev system [16]. The SCML-03 system, depicted in Figure 8, consists of a main body, servo motors for vertical and horizontal movement, a three-axis force measurement system, sample container, an annular PMG, drive motor, and data collecting and processing units. The annular PMG is attached to a large circular disc with a diameter of 1500 mm. When the circular disc rotates at 1280 rpm around its central axis, the maximum linear speed of the PMG is approximately 300 km/h. The dynamic force between the PMG and the HTS container during the rotation of the circular disc at different speeds is measured using the three-axis force measurement system. The force sensor in this system can measure vertical and horizontal forces with a precision of ±1%, up to 3350 N and 500 N, respectively.

Figure 8. The Photo of the Superconducting Dynamic Magnetic Levitation Force Measurement System (SCML-03) [16_].

Deng et. al., fabricated an ultra-high-speed Maglev test setup to measure the dynamic running characteristics of both superconducting Maglev and PM electrodynamic levitation (EDL) systems [17]. The schematic illustration of this system is given in Figure 9. In this experimental setup, a 550 kW inverter-fed AC motor propels a vertically rotating rotor with a diameter of 2500 mm. The main functions of this system include the ability for the test sample to move or remain stationary in both the lateral and vertical directions as needed for experiments. The rotational velocity of the guideway rotor can be changed according to the specific needs of the experiment. The electromagnetic vibrator can induce various frequencies and amplitudes of excitations on the samples. The system enables the measurement of levitation force, guidance force, and dynamic parameters of the HTS bulks, along with assessing magnetic stiffness. Additionally, it facilitates the levitation force and drag force measurements, as

well as the dynamic parameters of the PM array in the EDL system.

Figure 9. Schematic Illustration of the Ultra-High-Speed Maglev Test System [17].
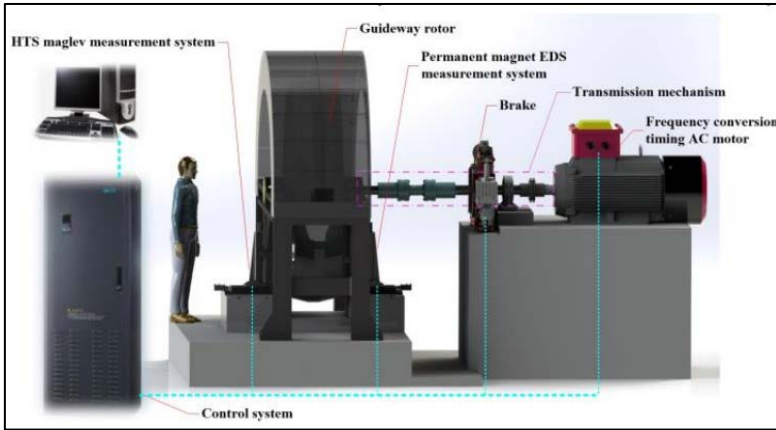
The key technical specifications of the testing system comprise a stainless-steel rotor with a diameter measuring 2500 mm and a width of 520 mm. The internal diameter of both the PMG and the aluminium guideway is 2210 mm. The guideway achieves a maximum linear speed of 600 km/h (equivalent to a rotation velocity of 1440 rpm), with an accuracy of ≤1%. The measurement system has a vertical and lateral displacement ranges of 200 mm and 800 mm, respectively.

4. "NEAR-SCALE" SUPERCONDUCTING MAGLEV SYSTEMS

In this section, we introduced the realm of "Near-Scale" Superconducting Maglev Systems, where the transition from experimental prototypes to systems with practical, real-world applications becomes increasingly evident. As we navigate through this section, our focus extends beyond the laboratory-scale models, exploring advancements that bring us closer to the

deployment of superconducting maglev technology on a scale that mirrors the demands and intricacies of everyday transportation. The shift towards near-scale implementations marks a pivotal step forward, opening avenues for a more comprehensive understanding of the challenges, possibilities, and transformative potential inherent in these evolving magnetic levitation systems. Although several research groups and institutions work on SC Maglev systems, below, we introduced only the closest one to real-scale commercial applications and named such kind of systems as "Near-Scale" Superconducting Maglev Systems.

A company called Evico, located in Germany-Dresden and affiliated with the "Leibniz Institute for Solid State and Materials Research," developed a Maglev system named "SupraTrans" in a laboratory environment [18]. The system was disassembled in Dresden in 2018 and transferred to the Karlsruhe Institute of Technology (KIT) for reconstruction in an outdoor environment and specifically for research on corrosion properties [19]. The vehicle, shown in Figure 10a, has a capacity for two passengers and is transported with four cryostats containing YBCO bulk superconductors. Only 0.1 litters of liquid nitrogen per hour are sufficient to keep the superconductors cold at 77K. The vehicle, measuring 2500 x 1200 mm and weighing 600 kg, has 2 cryostats mounted on each front and rear axle. The main frame between the axles carries the linear motor, inductive power collector, all electrical equipment, and 2 passenger seats. Developed in collaboration with Dresden University of Applied Sciences, this vehicle is designed for use as a door-to-door shuttle for airline passengers in modern centres. NdFeB magnets for the 80 m-long magnetic track (Figure 10b) are mounted on iron cores. A new track design, along with a semi-automatic assembly tool, has been developed for the efficient production of the magnetic guidance path. Additionally, cables and converters are used for

inductive power supply, along with a passive reaction rail for the linear drive. The vehicle, driven by a 3.4 kW motor on the PMG, has a maximum carrying capacity of 6000 N and can reach a maximum speed of 20 km/h with a maximum acceleration of 1 m/s².

Figure 10. The SupraTrans Maglev Prototype Developed by the Evico Company. (a) Passenger Cabin for Two People, (b) PMG Consisting of NdFeB Permanent Magnets [19].
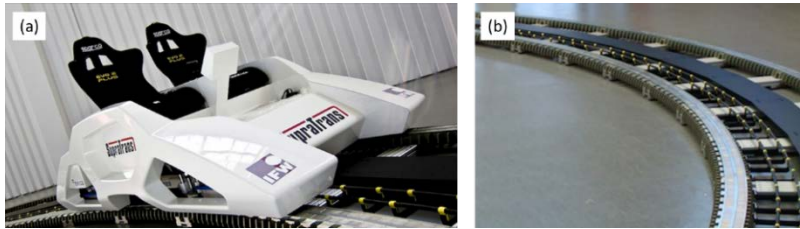
One of the mentioned systems, called Maglev-Cobra, is being developed in Brazil. The Maglev-Cobra project began in 2000 with a small model (Figure 11a), and it concluded in 2006 [20]. Subsequently, work commenced on developing a comprehensive test vehicle designed to accommodate 30 passengers. The vehicle is structured with four modules, each measuring 1.5 meters in length, featuring six levitation cryostats and a linear induction motor. In 2016, the researchers fabricated a 200-m test line at the campus of the Federal University of Rio de Janeiro [21] featuring two stations at each end, positioned at a height difference of 2.5 meters, resulting in a slope of 1.3%. This line and the Maglev vehicle on it are shown in Figure 11. The full-scale version of the vehicle comprises four interconnected modules linked by mechanical connections. Its transportation capacity is measured at 5 passengers per square meter, representing a threshold for transportation comfort and quality. With a total carrying capacity of 30 passengers divided into four modules, the vehicle is equipped with a linear induction motor (LIM) featuring two short primaries powered by two electronic

inverters. The vehicle's total no-load weight is 2000 kg, classifying it as a Light Rail Vehicle (LRV).

Figure 11. The Maglev-Cobra project. (a) Passenger cabin of the first prototype [20], (b) Moving vehicle and close view to the levitation gap between the cryostat and PMG, (c) an overhead perspective of the MagLev-Cobra test line spanning 200 meters, and (d) side view of the vehicle in operation [21].
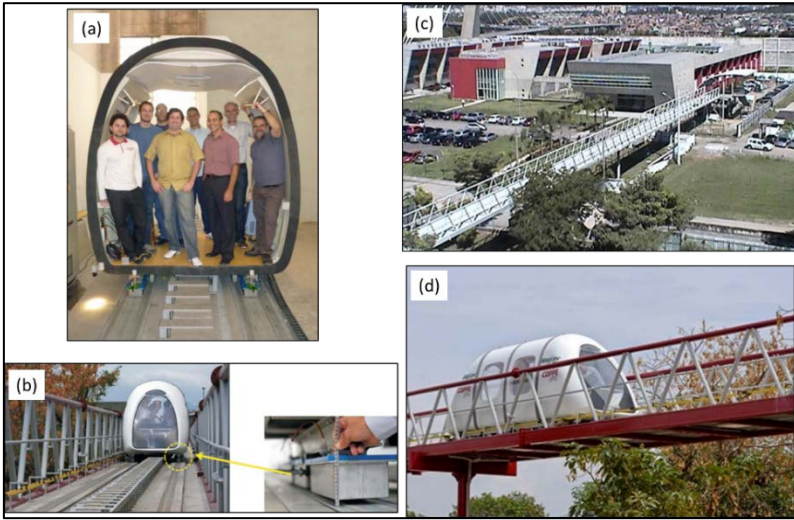
The researchers at Southwest Jiaotong University developed a high-speed running test platform [22]. This system is a component of the multifunctional high-speed train operation simulation test platform, which also facilitates high-speed experimental research for wheel-rail trains. On one side of the platform, there is a track for wheel-rail trains, while the other side features a PMG for the HTS Maglev vehicle. The high-speed HTS maglev test platform comprises three main components: 1) the levitation system, consisting of the PMG and the maglev vehicle; 2) the linear propulsion system, primarily including the power supply system, control system, mover, and stator of the linear motor; and 3) the PM eddy current braking device, which also utilizes the PMs. The entire platform is enclosed within a 4.2-meter-diameter tube, capable of establishing a low-pressure

environment for future studies on train aerodynamics and hyperloop technology. Because of the restricted length of the test track, the motor-actuated model vehicle weighing 220 kg (maximum) is required to reach a speed of 120 m/s (equivalent to 432 km/h) within a distance of 50 m. This entails achieving an acceleration of approximately 15 g, with the maximum traction force reaching 70 kN to facilitate such high acceleration.

5. CONCLUSIONS

In conclusion, this chapter has explored the magnetic levitation force measurement systems and techniques for superconducting Maglev systems. Beginning with an introduction to the fascinating interplay between superconductivity and magnetism, the chapter delved into the historical evolution of transportation, emphasizing the pivotal role of superconducting materials in advancing Maglev technology. The subsequent sections navigated through static and dynamic magnetic levitation force measurement systems, providing a comprehensive understanding of the methods used to measure forces under different conditions. The discussion extended to the developments in near-scale superconducting Maglev systems, showcasing examples of experimental prototypes and test vehicles that bring us closer to real-world applications. Notable systems, such as SupraTrans developed by Evico in Germany and Maglev-Cobra in Brazil, exemplify the shift toward practical, near-scale implementations. Additionally, the high-speed running test platform at Southwest Jiaotong University highlights the ongoing efforts to simulate and study the dynamic behavior of Maglev systems.

The chapter concludes by emphasizing its intention to serve as a comprehensive guide, contributing to a broader understanding of force measurement systems and techniques

crucial for the optimal operation of superconducting Maglev systems. The exploration of both technical aspects and practical applications sets the stage for future advancements in this transformative field of transportation technology.

REFERENCES

[1]   Innes, A. R., & Rhoderick, E. H. (1980). Introduction to superconductivity. Pergamon Press.

[2]   Moon, F. C. (2008). Superconducting levitation: Applications to bearings and magnetic transportation. John Wiley & Sons.

[3]   Ozturk, K., Abdioglu, M., & Karaahmet, Z. (2020). Magnetic force and stiffness performances of Maglev system based on multi–surface arrangements with three-seeded bulk YBaCuO superconductors. Physica C: Superconductivity and its Applications, 578, 1353739.

[4]   Çelik, Ş., & Öztürk, K. (2009). Semiempirical equation of the levitation-force density for (Sm123) 1–x (Yb211) x superconducting samples. physica status solidi (a), 206(4), 724-730.

[5]   Hull, J. R., & Cansiz, A. (1999). Vertical and lateral forces between a permanent magnet and a high-temperature superconductor. Journal of Applied Physics, 86(11), 6396-6404.

[6]   Yang, W. M., Zhou, L., Feng, Y., Zhang, P. X., Nicolsky, R., & de Andrade Jr, R. (2003). The characterization of levitation force and attractive force of single-domain YBCO bulk under different field cooling process. Physica C: Superconductivity, 398(3-4), 141-146.

[7] Yang, W. M., Zhou, L., Feng, Y., Zhang, P. X., Wang, J. R., Zhang, C. P., ... & Wei, W. (2001). The effect of magnet configurations on the levitation force of melt processed YBCO bulk superconductors. Physica C: Superconductivity, 354(1-4), 5-12.

[8] Celik, S. (2016). Design of magnetic levitation force measurement system at any low temperatures from 20K to room temperature. Journal of Alloys and Compounds, 662, 546-556.

[9] Wang, J. S., & Wang, S. Y. (2005). Synthesis of Bulk Superconductors and Their Properties on Permannent Magnet Guideway. Frontiers in superconducting Materials, 885-912.

[10] Wang, S., Wang, J., Deng, C., Lu, Y., Zeng, Y., Song, H., ... & Zhang, Y. (2007). An update high-temperature superconducting maglev measurement system. IEEE transactions on applied superconductivity, 17(2), 2067-2070.

[11] Wen, Y., Xin, Y., Hong, W., & Zhao, C. (2019). A force measurement system for HTS maglev studies. IEEE Transactions on Instrumentation and Measurement, 69(7), 5018-5026.

[12] Abdioglu, M., Ozturk, K., Gedikli, H., Ekici, M., & Cansiz, A. (2015). Levitation and guidance force efficiencies of bulk YBCO for different permanent magnetic guideways. Journal of Alloys and Compounds, 630, 260-265.

[13] Ozturk, K., Abdioglu, M., Sahin, E., Celik, S., Gedikli, H., & Savaskan, B. (2015). The effect of magnetic field distribution and pole array on the vertical levitation force properties of HTS maglev systems. IEEE Transactions on Applied Superconductivity, 25(4), 1-7.

[14] Abdioglu, M., Ozturk, K., Ekici, M., Savaskan, B., Celik, S., & Cansiz, A. (2021). Design and experimental studies on superconducting maglev systems with multisurface HTS–PMG arrangements. IEEE Transactions on Applied Superconductivity, 31(6), 1-7.

[15] Ozturk, K., Badía-Majós, A., Abdioglu, M., Dilek, D. B., & Gedikli, H. (2021). Experimental and numerical investigation of levitation force parameters of novel multisurface Halbach HTS–PMG arrangement for superconducting Maglev system. IEEE Transactions on Applied Superconductivity, 31(7), 1-12.

[16] Wang, J., Wang, S., Deng, C., Zeng, Y., Zhang, L., Deng, Z., ... & Zhang, Y. (2008). A high-temperature superconducting maglev dynamic measurement system. IEEE transactions on applied superconductivity, 18(2), 791-794.

[17] Deng, Z., Zhang, W., Kou, L., Cheng, Y., Huang, H., Wang, L., ... & Ma, Q. (2021). An ultra-high-speed maglev test rig designed for HTS pinning levitation and electrodynamic levitation. IEEE Transactions on Applied Superconductivity, 31(8), 1-5.

[18] Schultz, L., de Haas, O., Verges, P., Beyer, C., Rohlig, S., Olsen, H., ... & Funk, U. (2005). Superconductively levitated transport system-the SupraTrans project. IEEE Transactions on Applied Superconductivity, 15(2), 2301-2305.

[19] Evico. (n.d.). SupraTrans. Retrieved November 27, 2023, from https://www.evico.de/en/research/supratrans

[20] Sotelo, G. G., De Andrade, R., Dias, D. H. N., Ferreira, A. C., Costa, F., Machado, O. J., ... & Stephan, R. M. (2013). Tests with one module of the Brazilian Maglev-Cobra

vehicle. IEEE Transactions on applied superconductivity, 23(3), 3601204-3601204.

[21] Mattos, L. S., Rodriguez, E., Costa, F., Sotelo, G. G., De Andrade, R., & Stephan, R. M. (2016). MagLev-Cobra operational tests. IEEE Transactions on applied superconductivity, 26(3), 1-4.

[22] Deng, Z., Zhang, W., Wang, L., Wang, Y., Zhou, W., Zhao, J., ... & Werfel, F. N. (2022). A high-speed running test platform for high-temperature superconducting maglev. IEEE Transactions on Applied Superconductivity, 32(4), 1-5.

RELATIONSHIP BETWEEN ACRYLAMIDE AND OXIDATIVE STRESS

Suzan ONUR[1]

Adnan AYHANCI[2]

1. INTRODUCTION

With the increasing world population, appropriate processes and conditions are necessary to meet the demand for safe food and to ensure that foods can be used without spoilage. In this process, thermal processing is one of the important methods that allows foods to last longer. Thermal processing is used not only to prevent the growth of microorganisms but also to enhance the sensory properties of foods, improve characteristics such as taste, color, flavor, texture diversity, and aroma, and to inactivate unwanted enzymes. Various methods such as cooking, frying, sterilization, or pasteurization are utilized for subjecting foods to thermal processing [1]. However, heating food at certain temperatures can lead to chemical reactions, and these reactions can result in the formation of undesirable carcinogenic or mutagenic compounds during thermal processing [2].

Acrylamide (ACR), a chemical that has been found to naturally occur in foods processed at high temperatures and is widely present in thermally processed foods, is used in many

---

[1] Dr. Öğr. Üyesi, Karabük Üniversitesi, Sağlık Bilimleri Fakültesi, Fizyoterapi ve Rehabilitasyon Bölümü, suzanonur@karabuk.edu.tr, ORCID: 0000-0001-8145-6090.

[2] Prof. Dr., Eskişehir Osmangazi Üniversitesi, Fen Fakültesi Biyoloji Bölümü, aayhanci@ogu.edu.tr, ORCID: 0000-0003-4866-9814.

industries worldwide [3, 4]. The presence of ACR has been demonstrated in various processed foods prepared at high temperatures (above 120°C), such as bread, chips, biscuits, and roasted coffee [5]. The heating process primarily triggers the formation of unwanted toxic compounds, including ACR, at high temperatures due to the Maillard reaction between asparagine and reducing sugars (fructose and glucose). As a result of these thermal processes, the Maillard reaction, which can produce various substances with cytotoxic, carcinogenic, and mutagenic effects, can lead to caramelization and lipid oxidation [6, 7].

Such compounds can be hazardous to human health and may lead to mutations causing chronic diseases such as cancer [8]. Particularly, ACR, along with compounds enriched in carbohydrates, proteins, and fats, such as furans and their derivatives, imidazoles and their derivatives, heterocyclic amines, nitrosamines, polycyclic aromatic hydrocarbons, chloropropanols, and esters, are among the unwanted substances that can emerge during thermal processes [9]. Due to these characteristics, ACR was classified as a 'probable human carcinogen' by the International Agency for Research on Cancer (IARC) in 1994, based on positive bioassay results in mice and rats, and was included in Group 2A [10]. Its harmful effects on health issues are frequently emphasized [4].

In recent years, studies on the relationship between individuals' dietary habits and their health have gained momentum [11]. ACR, a substance known for its negative effects on health through nutrition in addition to industrial use, has been prominently featured in numerous experimental studies [12]. Particularly, it has been reported that various reactions occur in the environment depending on the reactions that take place during food preparation, leading to the formation of new compounds in the content of the food. While some of these compounds are desired for foods (such as certain aroma compounds), others have

been considered undesirable due to either causing a bad taste in the food or directly negatively affecting human health. ACR, as one of these compounds, is considered an unwanted component in foods due to its adverse effects on human health [11]. Considering the potential hazards of these substances to human health and the environment, various strategies are being developed in the food industry to reduce the formation of these compounds [9]. Given the health risks associated with ACR intake, mitigating the content of ACR in foods and adopting proactive measures against its harmful effects are among the most crucial issues in food safety [4].

Being a substance that has been extensively researched due to the observation of various damages in individuals exposed to ACR [13, 14], ACR (C_3H_5NO; 2-propenamide) has a molecular weight of 71.09 g/mol [11]. It appears as a white crystal in liquid form and is an odorless unsaturated amide [15] (Figure 1). The low molecular weight and high solubility in water enable ACR to easily penetrate various biological membranes [11]. ACR exhibits weak acidic and basic properties, with a melting point of 84.5°C and a boiling point of 125°C. It dissolves well in both water and polar organic solvents such as ethanol, methanol, diethyl ether, and acetone [11, 12, 16]. However, it has limited solubility in non-polar solvents (such as hexane and heptane) [12, 16]. Additionally, it readily undergoes polymerization under UV light and at its boiling point of 125°C. Comprising 50.69% carbon (C), 19.71% nitrogen (N), 7.09% hydrogen (H), and 22.51% oxygen (O), ACR is combustible and irritating [11].

Figure 1. The Chemical Structure of ACR

ACRILAMMIDE
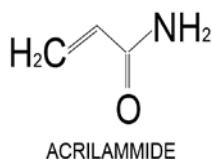
ACR can exist in two different forms: as a monomer and as a polymer (polyacrylamide). While the monomeric form exhibits toxic properties, the polymeric form does not. Studies have indicated that the monomeric form of ACR has carcinogenic and mutagenic effects in mammals and can cause harmful effects on the nervous system [16, 17]. Additionally, it has been reported to be neurotoxic, reproductive toxic, and carcinogenic in animal species [3]. Furthermore, ACR has been identified as a potent neurotoxin that affects male fertility and consequently leads to birth defects. Prolonged exposure to ACR has been found to cause nephrotoxicity, genotoxicity, neurotoxicity, epithetoxicity, and testis toxicity in laboratory animals [18].

ACR can react with small reactive molecules such as urea $(CO(NH_2)_2)$, formaldehyde (HCHO), glyoxal $(CHO)_2$, aldehydes (RCHO), amines (R_2NH), thiols (RSH), among others [19]. It can also bind to plasma proteins, particularly hemoglobin [14]. ACR undergoes oxidative biotransformation by cytochrome P450 2E1 (CYP2E1) [20], leading to the formation of glycidamide (GA), which is more reactive towards DNA and proteins compared to the parent compound ACR (Figure 2) [14, 21]. The genotoxic effects on DNA have been attributed to the biotransformation of ACR and the resulting GA [22].

Figure 2. Metabolic Pathway of ACR Converted to GA [14].
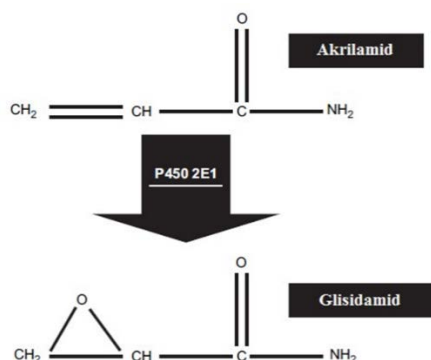
Neurotoxic effects of ACR have been observed only in humans and specifically at high exposure levels in occupational settings [3]. Given that ACR is a known neurotoxic compound for humans, it is crucial to identify foods containing high concentrations of acrylamide, especially at elevated levels, and recommend necessary precautions [23]. It is indicated that ACR in foods can arise through the degradation of lipids, carbohydrates, or free amino acids, resulting in the loss of water or carboxyl groups from organic acids such as malic, lactic, and citric acids via acrolein or acrylic acid, as well as through a direct formation mechanism from amino acids [16].

The general theory regarding ACR formation in foods is closely associated with the Maillard reaction, and it is considered a byproduct of this reaction [16]. (In other words, under conditions that lead to the formation of Maillard browning products during food processing, ACR is produced [24, 25] (Figure 3). During this reaction, it is noted that amino acids are degraded by intermediates that decarboxylate amino acids and deaminate them to form an aldehyde [26]. Particularly, thermal processes such as baking, roasting, and frying at temperatures exceeding 120°C during the processing of plant-based foods (such as grains, coffee, almonds, olives, potatoes, and jerusalem artichokes) [27, 28] can result in heat-induced reactions between the amino group of asparagine and the carbonyl groups of sugars [16, 25]. Therefore, cooked plant-based foods rich in asparagine, such as grains and potatoes, contribute to the formation of ACR [26].

The World Health Organization (WHO) has reported, based on data from numerous studies, that the average daily intake of ACR through food is between 0.3-0.8 grams [30]. The intake of ACR through diet has become a potential risk to human health. Therefore, finding an effective intervention method to prevent or mitigate ACR toxicity is crucial [31].

Figure 3. Schematic Representation of the Maillard Reaction and ACR Formation [29].
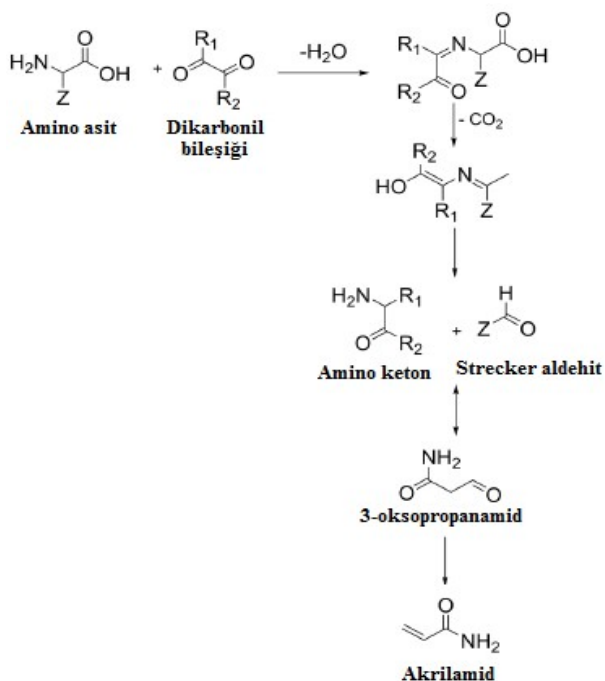
Studies have determined that the most intense and easily excreted route for ACR in the body is through urine. It has been found that 40-70% of ACR and its products are excreted through urine, 5-6% through feces, 6% through respiratory excretion, and 15% through bile [32].

ACR entering the body undergoes metabolism through two main pathways. The first involves the combination with glutathione (GSH) catalyzed by glutathione S-transferase (GST) enzyme [33, 34]. The second metabolic pathway of ACR involves epoxidation to form GA [33, 35, 36].

2. AKRYLAMIDE AND OXIDATIVE STRESS

Oxidative stress (OS) refers to the imbalance between the production of free radicals and the protective antioxidant (AO) systems, favoring free radicals [37]. The most important free radicals formed in living organisms are those derived from oxygen. Reactive oxygen species (ROS) can cause mitochondrial damage and impairment of cell function because they are unstable and can react with proteins in the cell membrane, nucleic acids, and polyunsaturated fatty acids [38]. The presence of ROS can lead to disruption of mitochondrial membrane permeability and initiation of apoptosis [39]. In biological systems, reactive species such as superoxide, hydroxyl radical, and hydrogen peroxide from molecular oxygen, as well as some reactive species from N and S sources, are generated as a result of metabolism and environmental factors. An increase in the concentration of these reactive species can disrupt cellular integrity by affecting essential molecules in the body, including cell membranes, DNA, macromolecules such as proteins, and especially polyunsaturated fatty acids, leading to the development of various diseases [40, 41].

Oxidative stress has been implicated in the pathogenesis and progression of inflammation, atherosclerosis, aging, hypertension, mutagenesis, carcinogenesis, immunological, urological, neurological diseases, eye disorders, digestive system issues, skin diseases, liver diseases, and lung diseases, as demonstrated by various studies [42-44]. The impact of OS on free radicals can lead to harmful effects on lipids, proteins, and DNA [45]. Additionally, studies have indicated that ACR can cause DNA damage and can conjugate with hemoglobin and plasma proteins [46].

ACR, which can enter the body through digestion, respiratory pathways, and absorption through the skin [47], can

easily pass through organic barriers such as the blood-placenta and blood-milk barriers [48]. In vivo animal studies have reported that ACR exhibits harmful effects in terms of neurotoxicity, hepatotoxicity and nephrotoxicity [49] and the mechanisms of these harmful effects are attributed to impaired nitric oxide (NO) neurotransmission, induced OS, lipid peroxidation and apoptosis [50-52]. Studies have also demonstrated that ACR induces multiple organ toxicity through the induction of OS and inflammation [52].

Research has shown that ACR damages cells by increasing oxidative stress. At high doses, ACR significantly increases OS due to changes in the redox state and the impact on AO enzyme activity [53]. Elevated levels of ROS can cause damage to macromolecules [54]. A study by Erfan et al. (2021) identified malondialdehyde (MDA) resulting from lipid peroxidation as a significant component in the pathogenesis of ACR hepatotoxicity. They found that ACR elevated ALT and AST levels, reduced SOD levels and caused tissue damage in liver tissues [55].

In in vitro studies [56, 57] and in rodents exposed to high doses of ACR [58, 59], it has been observed that ACR induces OS, leading to the formation and increase of ROS and a decrease in the effectiveness of antioxidant defense mechanisms [30]. Increased ACR-induced lipid peroxidation and decreased GSH levels have been reported in various organs of rodents [28, 58, 60]. Additionally, ACR has been reported to induce OS in hepatocytes [61], nerve cells [62, 63] and colonic cells [64], slowing down cellular functions and causing cell death [65]. In mouse epidermal cells, ACR has been reported to increase Cox-2 expression, and in breast epithelial cells, it elevates nitric oxide synthase [60, 66, 67]. Increased Cox-2 expression triggers apoptosis resulting in cell destruction [60].

Although ACR undergoes metabolism in the liver, reports on hepatotoxicity in humans are scarce. Numerous studies in animals have determined that ACR intake through diet can have harmful effects on the liver due to OS. In experimental adult rats, a dose of 25 mg/kg ACR was administered for 21 days, resulting in a significant decrease in GSH levels and total antioxidant levels in the liver. Furthermore, a decrease in SOD and CAT activities, an increase in serum levels of liver enzymes (AST and ALT) and an elevation in total oxidant levels were reported after ACR administration [68, 69].

Lipid peroxidation is a process consisting of initiation, propagation, and termination steps, generally defined as the attack of oxidants such as free radicals on carbon-carbon double bonds in lipids, especially polyunsaturated fatty acids. Therefore, inhibiting lipid peroxidation can be used as an important method to reduce the harmful effects of ACR [70]. Additionally, a decrease in antioxidant defense mechanisms leads to the formation of lipid peroxidation and an increase in tissue MDA levels [71].

Studies have identified the antioxidant activity and capacity to inhibit lipid peroxidation in some animal and plant-derived products. These include quinoa, Origanum vulgare (oregano), soybeans, Amaranthus hypocondriacus (Prince's feather), rice, Ambrosia mantegazzianus (giant ragweed), fish, eggs and milk proteins [72, 73]. The findings of in vitro and in vivo studies have shown that the toxicities caused by agents affecting cells can be significantly prevented by using certain plant-derived substances with antioxidant properties [74, 75].

3. CONCLUSION

In conclusion, ACR is a toxic compound that can naturally form in certain foods processed at high temperatures. The

formation of ACR is inevitable, especially during thermal processes, notably the Maillard reaction. This compound has various adverse effects on human health, particularly by increasing oxidative stress and causing cellular damage.

Research has demonstrated that ACR has neurotoxic, hepatotoxic, and nephrotoxic effects. The metabolism of ACR, especially in the liver, can increase oxidative stress and weaken antioxidant defense mechanisms. This situation can lead to the triggering of harmful reactions, such as lipid peroxidation, and an increase in cellular damage.

On the other hand, it has been found that certain foods with antioxidant properties can inhibit lipid peroxidation and reduce the harmful effects of ACR. Therefore, incorporating antioxidant-rich foods into daily nutrition could be an effective strategy to alleviate the negative effects of ACR.

However, the detailed understanding of ACR's effects is still ongoing, and research in this field continues. Changes made in the food industry and consumer preferences represent significant steps toward developing strategies to reduce ACR formation and enhance food safety.

REFERENCES

[1] Tareke, E., Rydberg, P., Karlsson, P., Eriksson, S. & Tornqvist, M. (2002). Analysis of acrylamide, a carcinogen formed in heated foodstuffs. *Journal of Agricultural and Food Chemistry,* 50(17), 4998-5006.

[2] Mogol, B.A. & Gökmen, V. (2016). Thermal process contaminants: Acrylamide, chloropropanols and furan. *Current Opinion in Food Science*, 7, 86-92.

[3] Exon, J.H. (2006). A review of the toxicology of acrylamide. *Journal of Toxicology and Environmental Health*, 9(5), 397-412.

[4] Li, D., Xian, F.F., Ou, J.Y., Jiang, K.Y., Zheng, J., Ou, S.Y., Liu, F., Rao, Q.C., Huang, C.H. (2022). Formation and Identification of Six Amino Acid-Acrylamide Adducts and Their Cytotoxicity Toward Gastrointestinal Cell Lines. *Frontiers in Nutrition*, 9.

[5] Acaroz, U., Ince, S., Arslan-Acaroz, D., Gurler, Z., Kucukkurt, I., Demirel,H.H., Arslan, H.O., Varol, N., Zhu, K. The ameliorative effects of boron against acrylamide-induced oxidative stress, inflammatory response, and metabolic changes in rats. *Food and Chemical Toxicology*, 2018, 118: 745-752.

[6] Stadler, R.H., Verzegnassi, L., Varga, N., Grigorov, M., Studer, A., Riediker, S. & Schilter, B. (2003). Formation of vinylogous compounds in model Maillard reaction systems. *Chemical Research in Toxicology*, 16(10), 1242-1250.

[7] Sharp, D. (2003). Acrylamide in food. *The Lancet*, 361(9355), 361-362.

[8] Arinç, E., Sen, A. & Bozcaarmutlu, A. (2000). Cytochrome P4501A and associated mixed function oxidase induction in fish as a biomarker for toxic carcinogenic pollutants in the aquatic environment. *Pure and Applied Chemistry*, 72(6), 985-994.

[9] Hamzalıoğlu, A., Mogol, BA. & Gökmen V. (2018). Acrylamide: An overview of the chemistry and occurrence in foods. *Encyclopedia of Food Chemistry*, 492499.

[10] Fazendeiro, MSPP. (2013). DNA damage induced by acrylamide: Role of genetıc polymorphisms in DNA damage levels. Doutoramento em Ciências da Vida, Universidade Nova de Lisboa, Faculdade de Ciências Médicas, Especialidade Genética, Lisboa, Portugal.

[11] Friedman, M. (2003). Chemistry, biochemistry, and safety of acrylamide. *Journal of Agricultural and Food Chemistry*, 51(16), 4504-4526.

[12] Gölükcü, M. & Tokgöz, H. (2005). Gıdalarda akrilamid oluşum mekanizması ve insan sağlığı üzerine etkileri. *Batı Akdeniz Tarımsal Araştırma Enstitüsü Dergisi*, 22(1), 41-48.

[13] Granath, F., Ehrenberg, L., Paulsson, B., Tornqvist, M., Marsh, G., Youk, A., Lucas, L. & Schall, L. (2001). Cancer risk from exposure to occupational acrylamide. *Occupational Environmental Medicine*, 58(9), 608-609.

[14] Besaratinia, A. & Pfeifer, GP. (2007). A review of mechanisms of acrylamide carcinogenicity. *Carcinogenesis*, 28(3), 519-528.

[15] Blasiak, J., Gloc, E., Woznıak, K. & Czechowska, A. (2004). Genetoxicity of acrylamide in human lymphocytes. *Chemico-Biological Interactions*, 149(23), 137-149.

[16] Nizamlıoğlu, N.M. & Nas, S. (2019). Gıdalarda akrilamid oluşum mekanizmaları, gıdaların akrilamid içeriği ve sağlık üzerine etkileri. *Akademik Gıda*, 17(2), 232-242.

[17] Lasekan, O. & Kassim, A. (2011). Investigation of the roasting conditions with minimal acrylamide generation in tropical almond (*Terminalia catappa*) nuts by response surface methodology. *Food Chemistry*, 125(2), 713-718.

[18] Alturfan, A.A., Tozan-Beceren, A., Şehirli, A.Ö., Demiralp, E., Şener, G., Omurtag, G.Z. Resveratrol ameliorates

oxidative DNA damage and protects against acrylamide-induced oxidative stress in rats. *Molecular biology reports*, 2012, 39: 4589-4596.

[19] Lingnert, H., Grivas, S., Jagerstad, M., Skog, K., Törnqvist, M. & Aman, P. (2002). Acrylamide in food: Mechanism of formation and influencing factors during heating of foods. *Scandinavian Journal of Nutrition*, 46(4), 159-172.

[20] Sumner, S.C., Fennell, T.R., Moore, T.A., Chanas, B., Gonzales, F. & Ghanayem, B.I. (1999). Role of cytochrome P4502E1 in the metabolism of acrylamide and acrylonitrile in mice. *Chemical Research in Toxicology*, 12(11), 1110-1116.

[21] Dearfield, K.L., Abernathy, C.O., Ottley, M.S., Brantner, J.H. & Hayes, P.F. (1988). Acrylamide: Its metabolism, developmental and reproductive effects, genotoxicity, and carcinogenicity. *Mutation Research*, 195(1), 45-77.

[22] Paulsson, B., Kotova, N., Grawé, J., Henderson, A., Granath, F., Golding, B. & Törnqvist, M. (2003). Induction of micronuclei in mouse and rat by glycidamide, genotoxic metabolite of acrylamide. *Mutation Research*, 535(1), 15-24.

[23] Abedini, A., Zirak, M.R., Akbari, N., Saatloo, N.V., Badeenezhad, A., Sadighara, P. Acrylamide; a neurotoxin in popcorns: a systematic review and meta-analysis. *Reviews on Environmental Health*, 2022.

[24] Friedman, M. & Levin, C.E. (2008). Review of methods for the reduction of dietary content and toxicity of acrylamide. *Journal of Agricultural and Food Chemistry*, 56(15), 6113-6140.

[25] Friedman, M. (2015). Acrylamide: Inhibition of formation in processed food and mitigation of toxicity in cells, animals, and humans. *Food and Function*, 6(6), 1752-1772.

[26] Mottram, D.S., Wedzicha, B.L. & Dodson, A.T. (2002). Acrylamide is formed in the Maillard reaction. Nature, 419(6906), 448-449.

[27] Tardiff, R.G., Gargas, M.L., Kirman, C.R., Carson, M.L. & Sweeney, L.M. (2010). Estimation of safe dietary intake levels of acrylamide for humans. *Food and Chemical Toxicology,* 48(2), 658-667.

[28] Prasad, S.N. (2013). Neuroprotective efficacy of eugenol and isoeugenol in acrylamide-induced neuropathy in rats: Behavioral and biochemical evidence. *Neurochemical Research*, 38(2), 330-345.

[29] Xu, X. & An, X. (2016). Study on acrylamide inhibitory mechanism in Maillard model reaction: Effect of p-coumaric acid. *Food Research International*, 84, 9-17.

[30] Lin, C.Y., Lee, H.L., Chen, Y.C., Lien, G.W., Lin, L.Y., Wen, L.L., Liao, C.C., Chien, K.L., Sung, F.C., Chen, P.C. & Su, T.C. (2013). Positive association between urinary levels of 8-hydroxydeoxyguanosine and the acrylamide metabolite Nacetyl-S-(propionamide)-cysteine in adolescents and young adults. *Journal of Hazardous Materials*, 261, 372-377.

[31] Zhao, M., Liu, X., Luo, Y., Guo, H., Hu, X. & Chen, F. (2015). Evaluation of protective effect of freeze-dried strawberry, grape, and blueberry powder on acrylamide toxicity in mice. *Journal of Food Science*, 80(4), H869-874.

[32] Sumner, S.C.J., Williams, C.C., Snyder, R.W., Krol, W.L., Asgharian, B. & Fennell, TR. (2003). Acrylamide: A

comparison of metabolism and hemoglobin adducts in rodents following dermal, intraperitoneal, oral or inhalation exposure. *Toxicological Sciences*, 75(2), 260-270.

[33] Sumner, S.C., Macneela, J.P. & Fennell, T.R. (1992). Characterization and quantitation of urinary metabolites of [1, 2, 3-13C] acrylamide in rats and mice using 13C nuclear magnetic resonance spectroscopy. *Chemical Research in Toxicology*, 5(1), 81-89.

[34] Yener, Y. (2008). Akrilamid uygulanan sıçanların kemik iliği hücrelerinde mitotik aktivite ile emperipolez ve mikronükleus sıklığının belirlenmesi. Doktora Tezi, Selçuk Üniversitesi, Fen Bilimleri Enstitüsü, Biyoloji Anabilim Dalı, Konya.

[35] Calleman, C.J., Bergmark, E. & Costa, L. (1990). Acrylamide is metabolized to glisidamide in the rat: Evidence from hemoglobin adduct formation. *Chemical Research in Toxicology*, 3(5), 406-412.

[36] Ghanayem, BL., Wang, H. & Sumner, S. (2000). Using cytochrome P-450 gene knock-out mice to study chemical metabolism, toxicity and carcinogenicity. *Toxicologic Pathology*, 28(6), 839-850.

[37] Halliwell, B. Drug antioxidant effects. *Drugs* 1991; 42: 569-605.

[38] H.Al-Gubory K. (2010). The roles of cellular reactive oxygen species, oxidative stress and antioxidants in pregnancy outcomes. *Int J Biochem Cell Biol.;* 42: 1634-1650.

[39] Yardim, A., Kandemir, F.M., Comakli, S., et al. (2021). Protective effects of curcumin against paclitaxel-induced

spinal cord and sciatic nerve injuries in rats. *Neurochem Res.* 46(2):379-395.

[40] Haris, E.D. (1992). Regulation of antioxidant enzeymes. *Faseb Jour*, 6:2675-2683.

[41] Miller, R.A & Britigan, B.E. (1997). Role of Oxidants in Microbial Pathophysiology. *Clininical Microbiology Reviews,* 10(1):p:1-18.

[42] Sorg, O. (2004). Oxidative stress: A theoretical model or biological reality? *Comptes Rendus Biologies*, 327(7):649-662.

[43] Halliwell, B. (2005). Free radicals and other reactive species in disease. *eLS.*

[44] Valko, M., Izakovıc, M., Mazur, M., Rhodes, C.J., Telser, J. (2004). Role of oxygen radicals in DNA damage and cancer incidence. *Molecular and Cellular Biochemistry*, 266(1-2):37-56.

[45] Turkes, C., Demir, Y., Beydemir, S. (2021). Infection medications: assessment Invitro glutathione S-transferase inhibition and molecular docking study. *Chemistry select*. 6(43):11915-11924.

[46] Xie, H., Wise, SS. & Wise, JPS. (2008). Deficient repair of particulate hexavalent chromium-induced DNA double strand breaks leads to neoplastic transformation. *Mutation Research*, 649(1-2), 230-238.

[47] Turkington, C., Mitchell, D. (2010). The encyclopedia of poisons and antidotes, Facts on file.

[48] Fuhr, U., Boettcher, M.I., Kinzig-Schippers, M., Weyer, A., Jetter, A., Lazar, A., et al. (2006). Toxicokinetics of acrylamide in humans after ingestion of a defined dose in a test meal to improve risk assessment for acrylamide

carcinogenicity, *Cancer Epidemiol. Biomark. Prev.* 15:266–271.

[49] Aboubakr, M., Ibrahim, S.S., Said, A.M., Elgendey, F., Anis, A. (2019). Neuroprotective effects of clove oil in acrylamide induced neurotoxicity in rats. *Pak Vet J.* 39: 111-115.

[50] Sumizawa, T. & Igisu, H. (2007). Apoptosis induced by acrylamide in SH-SY5Y cells. *Archives of Toxicology*, 81(4), 279-282.

[51] Pruser, K.N., Flynn, N.E. (2011). Acrylamide in health and disease. *Frontiers in Bioscience-Scholar*, 3:41-51.

[52] Abdel-Daim, M.M., Abo, El-Ela, F.I., Alshahrani, F.K., Bin-Jumah, M., Al-Zharani, M., Almutairi, B., Alyousif, M.S., Bungau, S., Aleya, L., Alkahtani, S. (2020). Protective effects of thymoquinone against acrylamide-induced liver, kidney and brain oxidative damage in rats. *Environmental Science and Pollution Research,* 27: 37709-37717.

[53] Teodor, V., Cuciureanu, M., Filip, C., Zamosteanu, N., Cuciureanu, R. (2011). Protective effects of selenium on acrylamide toxicity in the liver of the rat. Effects on the oxidative stress, *Rev. Med. Chir. Soc. Med. Nat. Iasi*. 115:612–618.

[54] Hong, Y., Nan, B., Wu, X., Yan, H. & Yuan, T. (2019). Allicin alleviates acrylamide induced oxidative stress in BRL-3A cells. *Life Sci*. 231:116550. DOI:10.1016/j.lfs.2019. 116550.

[55] Erfan, O.S., Sonpol, H.M. & Abd El-Kader, M. (2021). Protective effect of rapamycin against acrylamide-induced hepatotoxicity: The associations between

autophagy, apoptosis, and necroptosis. *Anat. Rec.* 304 (9):1984–1998. DOI:10.1002/ ar.24587+

[56] Jiang, L., Cao, J., An, Y., Geng, C., Qu, S., Jiang, L. & Zhong, L. (2007). Genotoxicity of acrylamide in human hepatoma G2 (HepG2) cells. *Toxicology in vitro*, 21(8), 1486-1492.

[57] Catalgol, B., Ozhan, G. & Alpertunga, B. (2009). Acrylamide-induced oxidative stress in human erythrocytes. *Human and Experimental Toxicology*, 28(10), 611-617.

[58] Zhu, Y.J., Zeng, T., Zhu, Y.B., Yu, S.F., Wang, Q.S., Zhang, L.P., Guo, X. & Xie, K.Q. (2008). Effects of acrylamide on the nervous tissue antioxidant system and sciatic nerve electrophysiology in the rat. *Neurochemical Research*, 33(11), 2310-2317.

[59] Zhang, J.X., Yue, W.B., Ren, Y.S. & Zhang, C.X. (2010). Enhanced role of elaidic acid on acrylamide-induced oxidative stress in epididymis and epididymal sperm that contributed to the impairment of spermatogenesis in mice. *Toxicology and Industrial Health*, 26(8), 469-477.

[60] Ghareeb, D.A., Khalil, A.C.R., Elbassoumy, A.M., Hussiena, H.M. & Abo-Sraiaab, M.M. (2010). Ameliorated effects of garlic (*Allium sativum*) on biomarkers of subchronic acrylamide hepatotoxicity and brain toxicity in rats. *Toxicological and Environmental Chemistry*, 92(7), 1357-1372.

[61] Cao, J., Liu, Y., Jia, L., Jiang, LP., Geng, C. & Yao, XF. (2008). Curcumin attenuates acrylamide-induced cytotoxicity and genotoxicity in HepG2 cells by ROS scavenging. *Journal of Agricultural and Food Chemistry*, 56(24), 12059-12063.

[62] Pernice, R., Hauder, J., Koehler, P., Vitaglione, P., Fogliano, V. & Somoza, V. (2009). Effect of sulforaphane on glutathione-adduct formation and on glutathione S transferase dependent detoxification of acrylamide in Caco-2 cells. *Molecular Nutrition and Food Research*, 53(12), 1540-1550.

[63] Park, H., Kim, MS., Kim, S.J., Park, M., Kong, K.H. & Kim, H.S. (2010). Acrylamide induces cell death in neural progenitor cells and impairs hippocampal neurogenesis. *Toxicology Letters*, 193(1), 86-93.

[64] Rodriguez-Ramiro, I., Martín, M.Á., Ramos, S., Bravo, L. & Goya, L. (2011). Olive oil hydroxytyrosol reduces toxicity evoked by acrylamide in human Caco-2 cells by preventing oxidative stress. *Toxicology*, 288(1-3), 43-48.

[65] Chen, J.H., Yang, C.H., Wang, Y.S., Lee, J.G., Cheng, C.H. & Chou, C.C. (2013). Acrylamide-induced mitochondria collapse and apoptosis in human astrocytoma cells. *Food and Chemical Toxicology*, 51, 446-452.

[66] Cook, L.E.L.J., Tareke, E., Word., B., Starlard-Davenport, A., Lyn-Cook, B.D. & Hammons, G.J. (2011). Food contaminant acrylamide increase expression of Cox-2 and nitric oxide synthase in breast epithelial cells. *Toxicology and Industrial Health*, 27(1), 11-18.

[67] Lim, T.G., Lee, B.K., Kwon, J.Y., Jung, S.K. & Lee, K.W. (2011). Acrylamide upregulates cyclooxygenase-2 expression through the MEK/ERK signalling pathway in mouse epidermal cells. *Food and Chemical Toxicology*, 49(6), 1254-1259.

[68] Ansar, S., Siddiqi, J., Zargar, S., Ganaie, MA. & Abudawood, M. (2016). Hepatoprotective effect of quercetin supplementation against acrylamideinduced DNA

damage in wistar rats. *BMC Complementary Medicine and Therapies*, 16(1), 327-331.

[69] Rifai, L. & Saleh, FA. (2020). A review on acrylamide in food: Occurrence, toxicity, and mitigation strategies. *International Journal of Toxicology*, 39(2), 1-10.

[70] Ayala, A., Muñoz, M.F., Arguelles, S. Lipid peroxidation: production, metabolism, and signaling mechanisms of malondialdehyde and 4-hydroxy-2-nonenal. *Oxid Med Cell Longev*, 2014, 2014: 360438.

[71] Fetoui, H., Feki, A., Ben Salah, G., Kamoun, H., Fakhfakh, F., Gdoura, R. (2015). Exposure to lambda-cyhalothrin, a synthetic pyrethroid, increases reactive oxygen species production and induces genotoxicity in rat peripheral blood. *Toxicol Ind Health.* 31(5):433-441.

[72] Srihari, T., Sengottuvelan, M., Nalini, N. Dose-dependent effect of oregano (Origanum vulgare L.) on lipid peroxidation and antioxidant status in 1,2-dimethylhydrazine-induced rat colon carcinogenesis. *Journal of Pharmacy and Pharmacology*, 2010, 60: 787-794.

[73] Neves, A.C., Harnedy, P.A., O'Keeffe, M.B., FitzGerald, R.J. Bioactive peptides from Atlantic salmon (Salmo salar) with angiotensin converting enzyme and dipeptidyl peptidase IV inhibitory, and antioxidant activities. *Food chemistry*, 2017, 218: 396-405.

[74] Aebi H.E., 1987, Catalase. In Bergmeyer HU, *Methods of Enzymatics Analysis*, 3:273-285.

[75] Felhi, S., Saoudi, M., Daoud, A., Hajlaoui, H., Ncir, M., Chaabane, R., El Feki, A., Gharsallah, N., Kadri, A. Investigation of phytochemical contents, in vitro antioxidant and antibacterial behavior and in vivo anti-

inflammatory potential of Ecballium elaterium methanol fruits extract. *Food Science and Technology*, 2017, 37: 558-563.

BIOSYNTHESIS METHODS USED IN NANOPARTICLE PRODUCTION[1]

Olcay GENÇYILMAZ[2]

1. INTRODUCTION

Studies on the discovery and production of nanoparticles with unusual and advanced properties in the size of 1-100 nm have been ongoing for the last quarter century. Nanoparticles have many physical, chemical and biological properties that are different from other alternative products. Therefore, nanoparticles are currently used in many fields such as paints, glasses, nanocomposite materials, cosmetics, sensors, cancer diagnosis and treatment. Nanomaterials are classified according to many properties such as morphological structures, homogeneity, size and content.

Generally, the production of nanoparticles is explained by two methods. These methods are Top Down Method and Bottom Up Method. Fig. 1 shows the general methods of nanoparticle production and the production methods used in these methods. Fig.1 shows that nanoparticle production can be achieved through two methods: chemical and physical, namely the Top Down Method and Bottom Up Method. These techniques have been used for many years and are still prevalent in nanoparticle production. However, it is important to note that

these physical and chemical production methods are not suitable for the production of non-toxic nanoparticles.

Although nanoparticles produced by these methods have various applications, their production involves the use of toxic chemicals and is not environmentally friendly, which limits their potential use in biotechnology. Therefore, in recent years, researchers have studied alternative production methods and discovered new ones to increase the use of nanoparticles, particularly in biotechnology and biomedical fields.

Figure 1. General Methods in Nanoparticle Production and Production Methods Used in These Methods
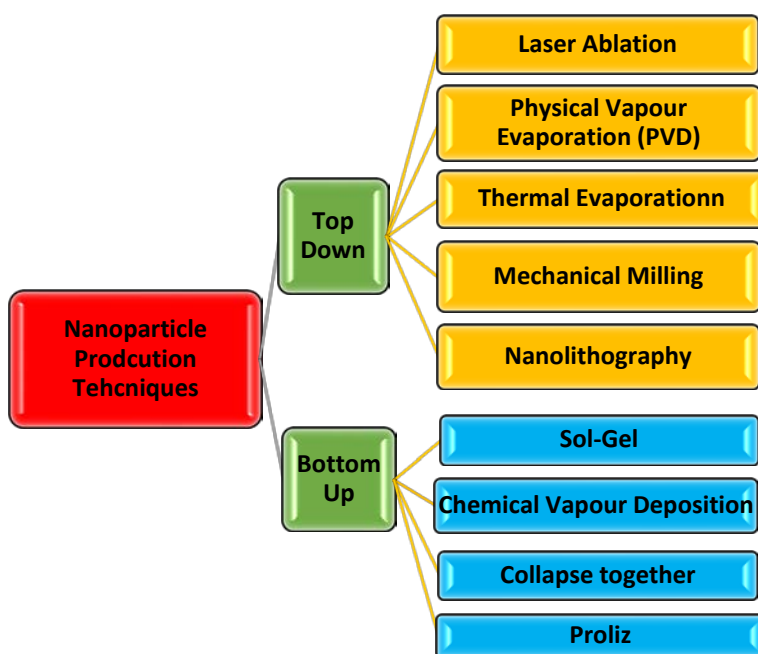
The method developed as an alternative to chemical and physical methods for synthesis non-toxic, environmentally

friendly, and reliable nanoparticles is commonly referred to as the 'biological method (biosynthesis)' or 'green synthesis'. This method has facilitated new experimental and theoretical studies in the production of nanoparticles, leading to the creation of nanoparticles with unexplored properties. The non-toxic and environmentally friendly nanoparticles produced through this method have various applications, including agriculture, nanomedicine, sensor nanoelectricity, development, cosmetics, energy storage devices, catalysts, and cancer diagnosis and treatment.

2. BIOLOGICAL METHOD (BIOSYNTHESIS) METHODS

Biosynthesis holds potential as a promising alternative to conventional chemical and physical methods for the production of nanoparticles. Biosynthesis holds potential as a promising alternative to conventional chemical and physical methods for the production of nanoparticles. This method offers numerous benefits. Biosynthesis utilizes biological agents, including fungi, plants, bacteria, and microorganisms to synthesis nanoparticles (Guilger-Casagrande and Lima, 2019; Iravani, 2011; Makarov et al., 2014; Seabra and Haddad, 2013; Sintubin et al., 2012; Mughal et al., 2021; Chen et al., 2021; Romano et al., 2022). This eco-friendly and sustainable method eradicates the need for harsh and toxic chemicals (Iravani, 2011). Furthermore, through biosynthesis, the creation of nanoparticles with varying characteristics, including size, surface charge, and morphology, is achievable (Guilger-Casagrande & Lima, 2019). This is necessary due to shortcomings observed in traditional physical and chemical approaches to nanoparticle synthesis, indicating a necessity for a new technique involving microorganism biosynthesis under certain conditions and in the presence of

catalysts. Green synthesis of nanoparticles entails the use of microorganisms such as fungi, bacteria, yeast, and algae, or biologically active materials like shells, fruit seeds, plant roots, and palm oil to produce the desired nanomaterials (Gour and Jain, 2019).

Nanoparticles form through the green synthesis technique as reactions take place in saline solutions. This process entails an oxidation and reduction process, in which microorganisms reduce electrons and convert them into metal ions, leading to nanoparticle production (Mohammadi and Ghasemi 2018). The green synthesis approach for creating metallic nanoparticles is straightforward, affordable, and low-energy. In contrast to physical and chemical methods, the green synthesis approach is more cost-effective and does not involve potentially toxic substances. Hence, it is a preferable method for medical, pharmaceutical, and environmental applications (Ahmed et al. 2017). Recently, there has been a growing interest among researchers in producing environmentally friendly nanoparticles through the green synthesis method. Such nanoparticles aid in mitigating environmental problems. Nanomaterials produced through this methodology are popular in biomedical applications due to their perceived environmental sustainability and lack of harm to humans (Devi and Gayathri 2014). Inorganic metal oxides are utilized as particles that effectively target and eliminate bacteria, fungi, microbes, and cancer cells in medical settings. Their non-toxic properties make them a safe choice. Nano-zinc oxide is an important inorganic metal oxide frequently utilized in personalized medicine due to its distinct medical and optical properties, as well as its chemical stability and durability. To incorporate metallic nanoparticles using the biosynthesis method, three crucial steps are needed: finding a solvent medium, a reducing agent that is environmentally friendly, and a non-toxic substance that

stabilizes the compound. Fig. 2 displays the biosynthesis process for nanoparticle production. In recent years, biosynthesis methods have been extensively studied for the production of nanoparticles, particularly for their application in biomedical, medical, and pharmaceutical fields. These nanoparticles exhibit varying surface and surface activity properties that can be controlled by their size.

Additionally, they possess size-dependent electrical, magnetic, and optical properties, making them useful in a wide range of applications, including sensors, carriers, electrodes, batteries, optoelectronics, cosmetics, agriculture, and textiles. Nanoparticles produced by non-toxic methods can be easily absorbed when applied to natural resources in environmental or biological applications. Therefore, it is important to produce nanomaterials that do not harm the environment or human health and to test them before application. Side effects that were not identified during production may occur during application. When dealing with the environment or living systems, one may encounter by-products that could be hazardous. The objective is to decrease the toxicity of nanomaterials by altering their structure through biosynthesis methods, while also enhancing their properties, such as recyclability and reusability. In recent years, numerous studies have been conducted and targets set to reduce the use of chemicals worldwide. The biosynthesis method shows promise in reducing environmental pollution and biological waste by decreasing the use of toxic chemicals and producing recyclable materials.

Figure 2. The Biosynthesis of Nanoparticle Production
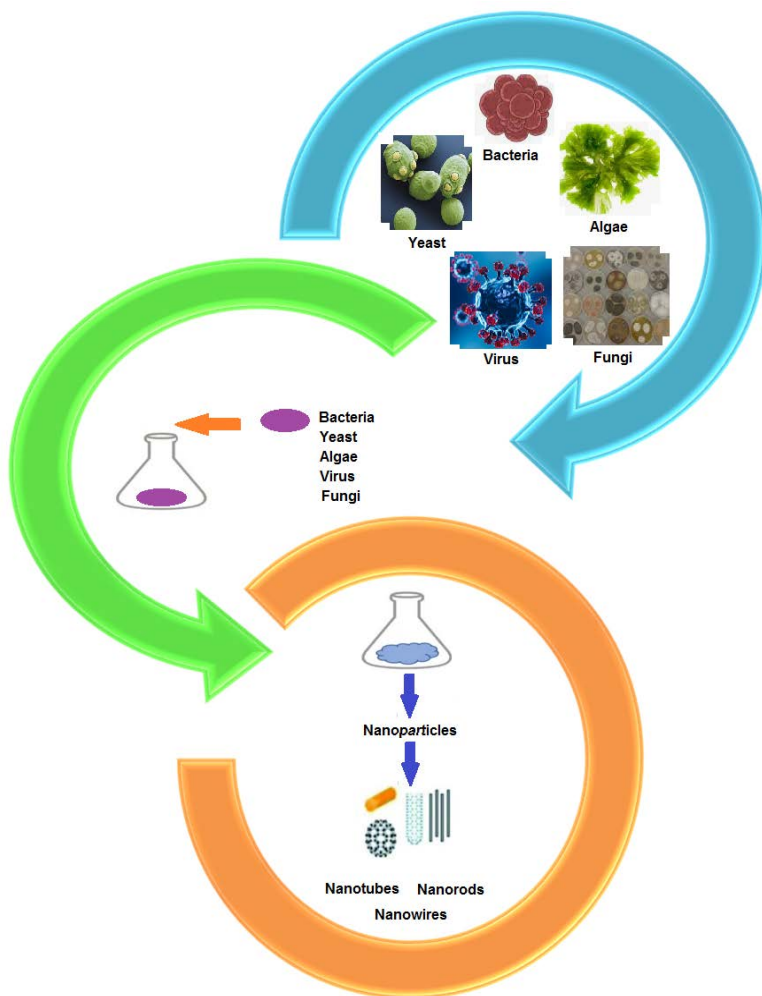
      Nanoparticles can be produced through biosynthesis using two main methods. Fig. 3 provides a schematic representation of this process. The figure illustrates the use of microorganisms and plants in nanoparticle production, as well as the biological products used during these productions.

Figure 3. A Schematic Representation of Nanoparticle Production by Biosynthesis
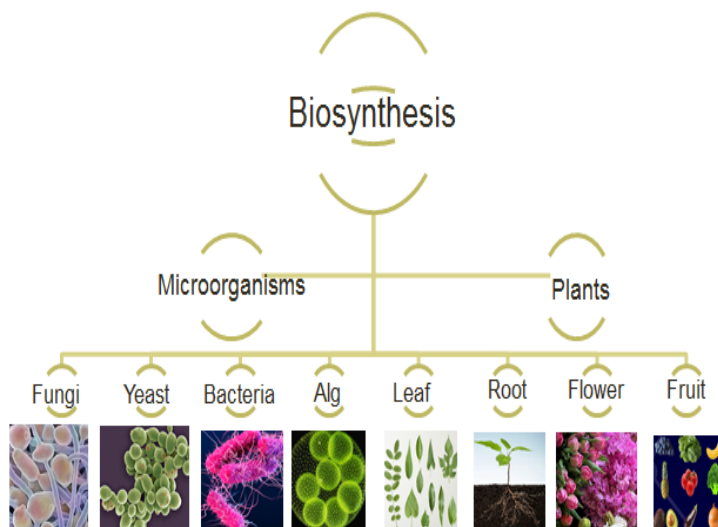
Biosynthesis can produce a range of metal and metal oxide nanoparticles, including Ag, Au, Pt, Zn, Fe, Cu, ZnO, CuO, CuO, FeO, and CoO. Both plants and microorganisms can be used in this process. Plants are often preferred due to their accessibility, abundance, and non-toxic nature. Specifically, plants with antibacterial properties are commonly used. Plants are commonly used in biosynthesis methods due to their ability to reduce metal ions. Plant extracts have been used to synthesize metal nanoparticles, such as silver and iron nanoparticles (Iravani, 2011; Seabra & Haddad, 2013; Njagi et al., 2010). These extracts can serve as both reducing and capping agents in the synthesis process (Njagi et al., 2010). When exposed to high concentrations of heavy metals, plants and microorganisms destroy their enzymes, membranes, and DNA, leading to cell death. Organisms have evolved to become more tolerant through the oxidation of enzymes and the polarization of less toxic metals (Sefaoğlu, 2020). This green synthesis approach offers

economic and valuable alternatives for the production of metallic nanoparticles (Seabra & Haddad, 2013).

Microorganisms are frequently used in biosynthesis methods, alongside plants. The primary advantage of using microorganisms is the reduction of the toxic effects of metal ions. Additionally, the formations that occur in microorganism cultures allow for the production of nanoparticles with varying morphologies. Bacteria, fungi, viruses, algae, yeasts, and enzymes are commonly used due to their low toxicity levels. Microorganisms have the ability to produce both intracellular and extracellular inorganic substances.

In summary, nanoparticle biosynthesis provides a sustainable and environmentally friendly alternative to traditional methods. This approach enables the production of nanoparticles with desired properties and can be carried out at ambient conditions (Romano et al., 2022). It has the potential to revolutionise various fields, including materials science, biotechnology, and medicine, by providing a cost-effective and efficient method for nanoparticle production.

2.1.Biosynthesis of Nanoparticles by Bacteria

Bacteria are used in biosynthesis processes. Genetic engineering of nanoparticle biosynthesis in bacteria can help tailor the properties of the nanoparticles to meet specific requirements (Chen et al., 2021). Furthermore, extremophilic microorganisms have been investigated for the green synthesis of antibacterial nanoparticles (Romano et al., 2022).

To produce metallic nanoparticles, scientists and researchers have increasingly focused on prokaryotic cells due to the presence and abundance of bacteria in the atmosphere and their ability to withstand harsh environmental conditions. These methods are the most important for producing nanoparticles due to their growth rates, ease of cultivation, low cost, and the

ability to monitor oxygen, temperature, and incubation time. Nanoparticles produced by bacteria come in various sizes and have multiple applications (Pantidos and Horsfall, 2014). Experiments have shown that certain types of bacteria can reduce heavy metal ions due to their ability to resist heavy metal toxicity, which can be harmful to microorganisms. Therefore, biosynthesis has become a crucial method for nanoparticle production (Iravani, 2014).

Bacteria can create nanoparticles through intracellular or extracellular synthesis. The negatively charged bacterial cell membrane can attract noble metals with positive charges. The cytotoxicity of metal nanoparticles is determined by the surface charge of the cell membrane. Cells with a positive charge are less affected by toxicity due to a thicker layer of peptidoglycan compared to cells with a negative charge of grams (Burlacu et al., 2019).

2.2.Biosynthesis of Nanoparticles by Fungi

Fungi have demonstrated significant potential for biogenic synthesis of nanoparticles. Several species of fungi can produce nanoparticles with varying properties (Guilger-Casagrande & Lima, 2019). The use of whole microbial cells in the biosynthesis process enables continuous production without cell death, further enhancing the feasibility of this method (Sintubin et al., 2012).

Fungi can synthesize nanoparticles using two methods: intracellular synthesis and extracellular synthesis. Intracellular synthesis involves electron transfer through the microbial cell, which polarizes nanoparticles in enzymes that convert metal ions into nanoparticles. However, the production of nanoparticles inside the cell is smaller than that outside the cell (Khandel and Shahi, 2018). Extracellular synthesis involves producing nanoparticles without unwanted elements present

inside the cell. Fungi's extracellular secretory components produce nanoparticles, which have a wider range of interactions than those produced by bacteria.

Furthermore, fungi secrete a greater number of enzymes, resulting in the rapid conversion of mineral salts into minuscule metal particles (Hasan, 2015). Fungi offer more advantages than other microorganisms for producing nanoparticles due to their ease of extraction and ability to produce a large number of proteins and enzymes outside the cell. These advantages increase nanoparticle production.

Additionally, filamentous fungi can produce highly stable nanoparticles that prevent molecular accumulation after long storage. Fig. 4 illustrates the steps of green synthesis by fungi (Kaur 2018)**.**

Figure 4. Steps of Green Synthesis of Nanoparticles Mediated by Fungi
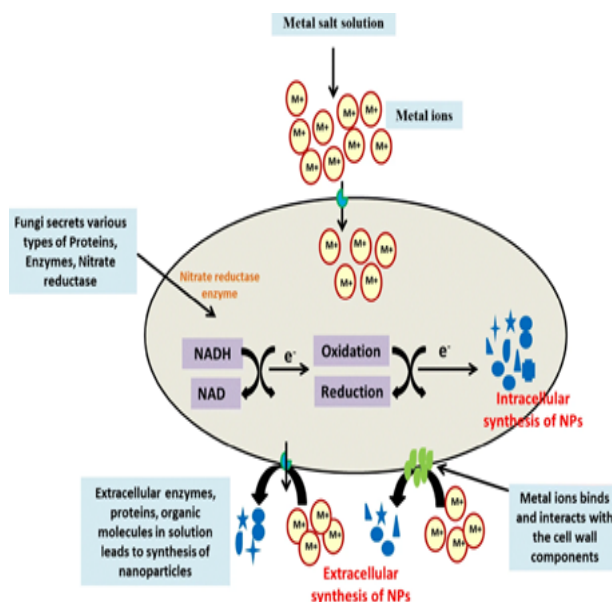
Source: (Khandel and Shahi 2018)

2.3. Biosynthesis of nanoparticles by algae

Algae are a significant source of biological nanomanufacturing due to their low toxicity and ability to bioaccumulate and reduce minerals. They have several advantages, including fast growth, easy processing, and the ability to produce large amounts of biomass, making them a preferred method for nanoparticle production. Algae are a diverse group, including brown algae, red algae, and green algae (Omomowo et al., 2020). Nanoparticles are produced through the reduction of metal ions by algae extracts in the presence of receptors such as proteins and sugars. This reduction process leads to the formation of nanoparticles (Singh and Singh, 2019). Nano production can occur both inside and outside the cell. Outside the cell, metal ions are reduced on the outer surface, while inside the cell, reduction occurs in the cell membrane and wall (Rajeshkumar et al., 2012).

2.4. Biosynthesis of Nanoparticles by Plant Extract

The production of nanoparticles using plant extracts is a simple, effective, fast, and low-cost method. Nanoparticles can be produced using various parts of plants, such as leaves, bark, seeds, stems, roots, and flowers. The chemicals present in plants are responsible for reducing metal ions (Khan et al., 2022). This method has gained significant importance in the production of nanoparticles. Plant extracts have become an increasingly popular alternative to physical and chemical methods in various applications, particularly in the medical field (Omomowo et al., 2020). One significant advantage of using plant extracts to produce nanoparticles is that it is safe for biomass and contains an abundance of reducing agents (Mohammadlou et al., 2016).

Nanoparticles are produced using plant extracts either at stable temperatures, such as plant extract receptors, or at room temperature through the reduction of aqueous metallic materials

mixed with plant extracts. Proteins, carbohydrates, fats, terpenoids, and phenolic compounds contain active functional groups such as hydroxyl, amines, ideogens, and carboxylic acids. These functional groups are considered to be active reducing agents, sources of production, and stability. Fig. 5 illustrates the steps of the green synthesis process in plants (Leela and Vivekanandan, 2008).

Figure 5. Plant-Mediated Green Synthesis Steps for Nanoparticles
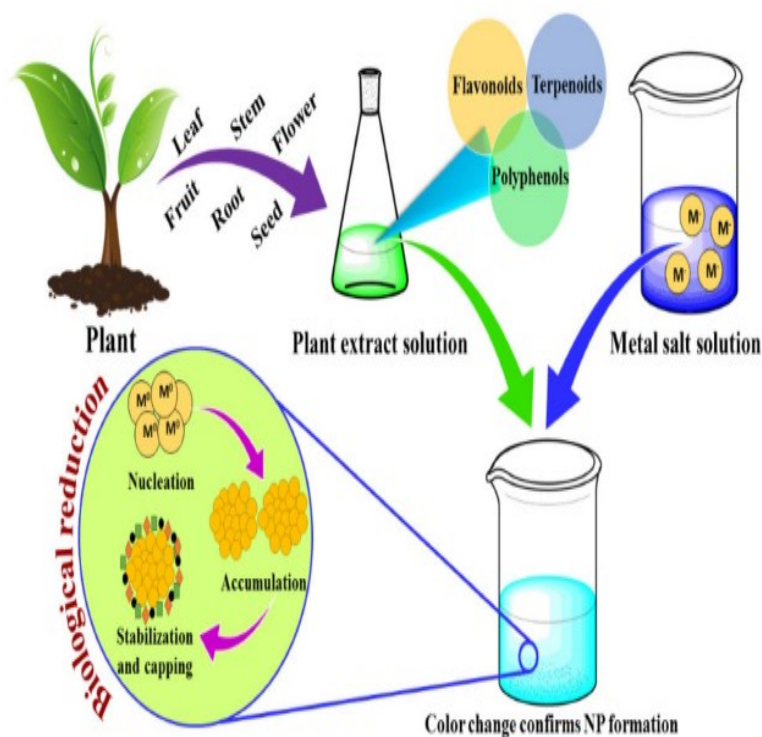
Source: (Dikshit *et al.* 2021)

REFERENCES

Ahmed, S., Chaudhry, S.A., Ikram, S. (2017), A review on biogenic synthesis of ZnO nanoparticles using plant extracts and microbes: a prospect towards green chemistry. Journal of Photochemistry and Photobiology B: Biology, 166: 272–284.

Burlacu, E., Tanase, C., Coman, N. A., Berta, L. (2019), A review of bark-extract-mediated green synthesis of metallic nanoparticles and their applications. Molecules, 24(23): 4354.

Chen, A., Hernandez-Vargas, J., Han, R., Cortazar-Martínez, O., Gonzalez, N., Patel, S., Keitz, B. K., Luna-Barcenas, G., Contreras, L. M. (2021), Small RNAs as a New Platform for Tuning the Biosynthesis of SilverNanoparticles for Enhanced Material and Functional Properties, CS Applied Material Interfaces, 13, 36769−36783.

Devi, R., Gayathri, R. (2014), Green Synthesis of Zinc Oxide Nanoparticles by using Hibiscus rosa-sinensis. International Journal of Current Engineering and Technology, 44(44): 2444–2446.

Gour, A., Jain, N. K. 2019. Advances in green synthesis of nanoparticles. Artificial cells, nanomedicine, and biotechnology, 47(1): 844–851.

Guilger-Casagrande, M., de Lima, R. (2019), Synthesis of Silver Nanoparticles Mediated by Fungi: A Review, Frontiers Bioenergy Biotechnology,7, 1-16.

Hasan, S. (2015), A review on nanoparticles: their synthesis and types. Res. J. Recent. Sci., 2277: 2502.

Iravani, S. (2014), Bacteria in nanoparticle synthesis: current status and future prospects. International scholarly research notices, 1: 359316.

Irivana, S. (2011), Green synthesis of metal nanoparticles using plant, Green Chemistry, 10, 13, 2638-2650.

Jiang, J., Pi, J., Cai, J. (2018), The advancing of zinc oxide nanoparticles for biomedical applications. Bioinorganic chemistry and applications, 1062562: 1-19.

Kaur, P. (2018), Biosynthesis of nanoparticles using eco-friendly factories and their role in plant pathogenicity: a review. Biotechnology Research and Innovation, 2 (1): 63–73.

Khandel, P., Shahi, S. K. 2018. Mycogenic nanoparticles and their bio-prospective applications: current status and future challenges. Journal of Nanostructure in Chemistry, 8(4): 369–391.

Leela, A., Vivekanandan, M. (2008), Tapping the unexploited plant resources for the synthesis of silver nanoparticles. African Journal of Biotechnology, 7 (17): 1-4.

Makarov, V. V., Love, A. J., Sinitsyna, O. V., Makarova, S. S., Yaminsky, I. V., Taliansky, M. E., Kalinina, N. O. (2014),Green Nanotechnologies: Synthesis of Metal Nanoparticles Using Plants, 20 (6), 35-45.

Mohammadi, F. M. , Ghasemi, N. (2018), Influence of temperature and concentration on biosynthesis and characterization of zinc oxide nanoparticles using cherry extract. Journal of Nanostructure in Chemistry, 8 (1): 93–102.

Mohammadlou, M., Maghsoudi, H., Jafarizadeh-Malmiri, H. (2016), A review on green silver nanoparticles based on plants: Synthesis, potential applications and eco-friendly approach. International Food Research Journal, 23 (2): 446-463.

Omomowo, I. O., Adenigba, V. O., Ogunsona, S. B, Adeyinka, G. C., Oluyide, O. O, Adedayo, A. A., Fatukasi, B. A. (2020), Antimicrobial and antioxidant activities of algal-mediated silver and gold nanoparticles. IOP Conference Series: Materials Science and Engineering. IOP Publishing, pp. 12010.

Mughal, B., Zaidi, S. Z. J., Zhang, X., Hassan, S. U. (2021), Biogenic Nanoparticles: Synthesis, Characterisation and Applications, Applied Science, 11, 2598-2612.

Njagi, E. C., Huang, H., Stafford, L., Genuino, H., Galindo, H. M., Collins, J. B., Hoag, G. E., Suib, S. L. (2011), Biosynthesis of Iron and Silver Nanoparticles at Room TemperatureUsing Aqueous Sorghum Bran Extracts, Langmuir, 27 (1), 264–271.

Pantidos, N , Horsfall, L. E. 2014. Biological synthesis of metallic nanoparticles by bacteria, fungi and plants. Journal of Nanomedicine & Nanotechnology, 5(5): 1-10.

Rajeshkumar, S., Kannan, C., Annadurai, G. (2012), Green synthesis of silver nanoparticles using marine brown algae Turbinaria conoides and its antibacterial activity. International Journal of Pharma and Bio Sciences, 3(4): 502–510.

Romano, I., Vitiello, G., Gallucci, N., Girolamo, R. D., Cattaneo, A., Poli, A., Donato, P. D. (2022), Extremophilic Microorganisms for the Green Synthesis of Antibacterial Nanoparticles, Microorganisms 10, 1885-1905.

Seabra, A. B., Haddad, P., Nelson, D. (2013), Biogenic synthesis of nanostructured ironcompounds: applications and perspectives, 7 (3), 90-99.

Sefaoğlu, M. 2020. Yeşil sentez yöntemiyle çinko nanopartiküllerin mikrosistemlerde üretimi ve karakterizasyonu. Gümüşhane University, MSc. Thesis, 77 page, Gümüşhane.

Sintubin, L., Verstraete, W., Boon, N. (2012), Biologically Produced Nanosilver: Current State and Future Perspectives, Biotechnology and Bioengineering, 109 (10), 2422-2436.

OBSERVATIONS ON HATCHING PERIOD OF *MERTENSIELLA CAUCASICA* (WAGA, 1876) (URODELA: SALAMANDRIDAE)

Ufuk BÜLBÜL[1]

1. INTRODUCTION

Arrival order of amphibians to breeding grounds and the abiotic conditions affecting time of breeding shape the biotic relationships which impress population abundance through time (Boone et al., 2002).

The inhabitation of larvae of newts occurs in ponds at different altitudes and at various times, throughout the winter and spring. The larvae living at the highland areas had longer growth periods. In addition, the conditions of the highland populations in the spring season and at the beginning of summer were similar to those of the lowland populations at the end of the winter and the beginning of spring. Long-term adaptation of larval development to different breeding zones occurs from the moment they hatch in the pond until they reach metamorphosis (Pearlson and Degani, 2011). The researches related to timing of hatching show a switch point that may indicate adaptive plasticity in response to environmental factors which cause mortality of egg or hatchling (Sih and Moore, 1993). Werner (1986) and Rowe and Ludwig (1991) put forward the timing of any switch point (including hatching) should be influenced by determinants which affect rates of growth or mortality in the appropriate and contiguous life-history stages.

---

[1] Prof. Dr., Karadeniz Technical University, Faculty of Science, Department of Biology, ufukb@ktu.edu.tr, ORCID: 0000-0001-6691-6968.

In the great crested newt, hatching rates of the eggs are dependent on temperature. Development changes in accordance with the type of pond and the date of egg laying. For instance, it may take two weeks for an egg to hatch out in a shallow, unshaded, and warm pond in June, while in a heavily tree shaded and cool pond or if laid earlier in February it could take three times as long (Langton et al., 2011).

Among amphibian populations, the size and number of deposited eggs may change significantly within a single species and even among females in the same population. Changes in size and number of the eggs may be interdependent and influenced by various internal and external factors (Kaplan and Salthe, 1979; Kaplan and Cooper, 1984; Rafińska 1991; Kalezić et al., 1994; Vučić et al., 2020). The females of newts (during the beginning of the breeding period) have a certain number of formed yolked oocytes that characterize the maximum number of eggs which might be laid in a given season. However, some eggs may not be deposited (Bell, 1977; Verrel and Francillon, 1986; Arntzen and Hedlund, 1990; Vučić et al., 2020).

Females of amphibians may retain or reabsorb part of the oviductal eggs and oocytes if the circumstances for oviposition and/or insemination are suboptimal, showing that egg deposition may be constrained environmentally (Cogălniceanu et al., 2013; Vučić et al., 2020). The continuity of ponds is one of the external agent affecting the period of oviposition (Kurdíková et al., 2011; Vučić et al., 2020).

The Caucasian salamander, *Mertensiella caucasica* (Figure 1) is endangered amphibian species classified in the VU (Vulnerable) category in the IUCN Red List. It occurs in a limited area in the northeast Anatolia (Kars, Artvin, Rize, Trabzon, Bayburt, Gümüşhane, Giresun, and Ordu provinces) and the western spurs of the Trialeti Mountain Ridge,

Meskhetian and Lazistanian ridges in Georgia. There are important fluctuations in the Georgian populations of *M. caucasica* and probably significant declining has been continuing in the Turkish populations during the past decades (Kaya et al., 2009).

Figure 1. A Male Individual of *M. caucasica* in Ağaçbaşı Population.

The literature provides information about ecology, habitat characteristics and conservation status of *M. caucasica* (Tarknishvili and Serbinova 1993; Tarknishvili 1994; Tarknishvili 1996; Tarknishvili and Serbinova 1997; Tarknishvili et al., 2008; Sayım et al., 2009; Tarknishvili and Kaya 2009). Current knowledge related to breeding of the Caucasian salamander was limited to the findings of Muskhelishvili (1964), Darevsky and Polozhikhina (1966), and Tarknishvili and Serbinova (1993). These researchers made considerable observations on the Georgian populations of *M. caucasica*. Most recent record on the hatching period of a Turkish population of the species was given by Bülbül and Koç (2022).

The present study gives additional knowledge on duration of embryonal development in a Turkish population of the Caucasian salamander.

2. RESULTS AND CONCLUSION

During the field surveys in 2021, a breeding population of *Mertensiella caucasica* in Ağaçbaşı Plateau of Köprübaşı district of Trabzon province (N: 40° 41ʹ 648ʹʹ and E: 40° 05ʹ 126ʹʹ, 1936 m altitudes a.s.l.) was observed (Figure 2).

Figure 2. The Map Showing the Study Area in Trabzon Province
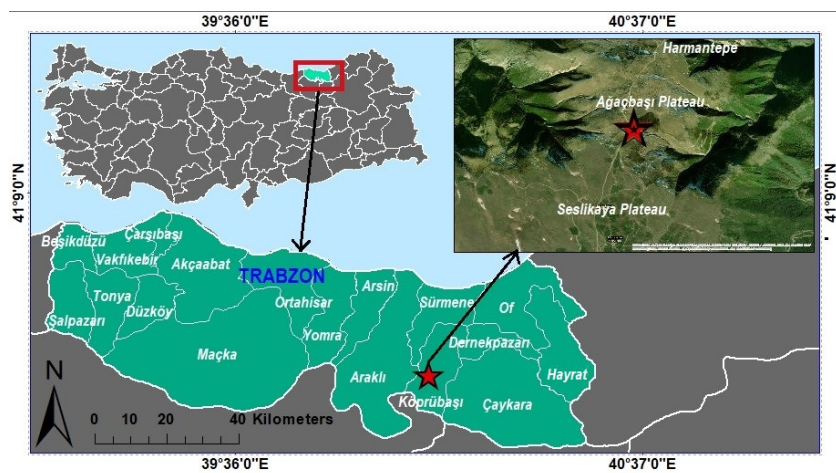
The length of the inhabited location is nearly 80 m. Salamanders breed in a small stream near a pathway. There is a natural environment consisting of small herbaceous plants around the stream.

The first observation in the study area was performed on 9 July 2021 around 3 p.m. The average air temperature (during the two-hour worktime) was 17 °C, while the stream water temperature was 14.5 °C. Twenty shaped embryos waiting in their gelatin egg cases and one degraded egg gelatin without any

embryos were found under a small rock with the bottom in contact with water (Figure 3).

Figure 3. The Eggs Containing inside Shaped Embryos of *M. Caucasica*

There were also older larvae, which were found under the small stones, in the study area (Figure 4).

Figure 4. General View of an Old Larva of *M. caucasica*.

Bülbül and Koç (2022) found 24 eggs of *M. caucasica* from Kayabaşı Plateau of Trabzon province on 9 June 2018 and

they observed the shaped embryos about three weeks after finding the eggs. Considering these findings, it can be assumed that the 20 embryos observed in the Ağaçbaşı population were left under the rock in the form of eggs at least 3 weeks ago (on June 18, 2021) or a little while ago.

Findings of Tarknishvili and Serbinova (1993) indicate that in females of *M. caucasica*, more than three days pass between fertilization and egg laying. It can be figured out that individuals of *M. caucasica* starts the breeding activities in the Ağaçbaşı population almost in the second half of June 2021. Similarly, Tarknishvili and Serbinova (1993) notified that the breeding period of the Caucasian salamander in habitats of the species takes place from the second half of June to early July and most of the females found in July are ready for egg deposition. However, Bülbül and Koç (2022) reported an earlier beginning time to breed (beginning of June) in the Kayabaşı population. These results exactly indicate that duration of breeding in the Caucasian salamander may differ according to the environmental circumstances.

The number of the eggs in both studies (20 in Ağaçbaşı population and 24 in Kayabaşı population) were compatible with the results of Tarknishvili and Serbinova (1993) who specified that each female deposits 11-24 eggs.

The second trip to the Ağaçbaşı site was made on 30 July 2021 around 1.30 p.m. The air temperature was 18.5 °C while the stream water temperature was about 16 °C. It was observed that 17 of the 20 embryos were healthy and active. However, 3 eggs were found to be damaged. The embryonal development was almost being completed and at that time a larva was seen to have hatched from the egg (Figure 5). It was estimated that the time elapsed from the date of laying the eggs under the rock (approximately 18 June 2021 or shortly before) to the time when

the first larvae hatched from the egg (30 July 2021) in the Ağaçbaşı population was at least 45 days.

Figure 5. The Arrow Shows the Larva Newly Hatched from The Egg. The remaining larvae are about to hatch.

Consistent with this, Tarknishvili and Serbinova (1993) stated that development of egg in *M. caucasica* takes 45 days until hatching in laboratory conditions, where the average temperature is 14.8 °C. The egg development may be extended to 48-51 days when the air temperature varies from 6 to 26 °C. In addition, Bülbül and Koç (2022) reported that the period of egg development took about 50 days in the Kayabaşı population of *M. caucasica*.

Finally, 18 more eggs were found under another rock during the day of the second visit (30 July 2021) to Ağaçbaşı (Figure 6). Of these, four had not yet shaped embryos, while thirteen had shaped embryos. One egg was damaged and there was no live embryo in it.

Figure 6. The Eggs and Shaped Embryos Found Under Another Rock During the Day of The Second Visit.

It is understood that the time of laying these eggs, in which shaped embryos can be seen, under the rock by a female individual coincides with the beginning of July. These findings clearly show that adult individuals of Caucasian salamander in the Ağaçbaşı population begin their breeding activities in June and continue in July.

In conclusion, findings of the present study revealed that period when *M. caucasica* begins its breeding activities and durations of egg laying, embryo development, and larval hatching of the Caucasian salamander may change depending on varied ecological conditions. Ongoing observations, which will be carried out in various environmental conditions along longer periods in the Georgian and Turkish populations of *M. caucasica*, may reveal different results.

3. ACKNOWLEDGEMENTS

REFERENCES

Arntzen J. W. and Hedlund L. (1990). Fecundity of the newts *Triturus cristatus*, *T. marmoratus* and their natural hybrids in relation to species coexistence. Holarctic Ecology, 13(4): 325-332.

Bell G. (1977). The life of the smooth newt (*Triturus vulgaris*) after metamorphosis. Ecological Monographs, 47(3): 279-299.

Boone M. D., Scott D. E., and Niewiarowski P. H. (2002). Effects of hatching time for larval Ambystomatid salamanders. Copeia, 2002(2): 511-517.

Bülbül U. and Koç H. (2022). Notes on breeding of *Mertensiella caucasica* (Waga, 1876) (Urodela: Salamandridae) from Black Sea coast of Turkey. Russian Journal of Herpetology, 29(6): 364-366.

Cogălniceanu D., Buhaciuc E., Tudor M., and Rosioru D. (2013). Is reproductive effort environmentally or energetically controlled? The case of the Danube crested newt (*Triturus dobrogicus*). Zoological Science, 30(11): 924-928.

Darevsky I. S., and Polozhikhina V. F. (1966). On the reproductive biology of the Caucasian salamander-*Mertensiella caucasica* (Waga). Zoologicheskii Zhurnal, 45(3): 465-466 [in Russian].

Kalezić M. L., Cvetković D., Đorović A., and Džukić G. (1994). Paedomorphosis and differences in life-history traits of two nieghbouring crested newt (*Triturus carnifex*) populations. Herpetological Journal, 4(4):151-158.

Kaplan R. H. and Salthe S. N. (1979). The allometry of reproduction: an empirical view in salamanders. American Naturalist, 113(5): 671-689.

Kaplan R. H. and Cooper W. S. (1984). The evolution of developmental plasticity in reproductive characteristics: an application of the "adaptive coin-flipping" principle. American Naturalist, 123(3): 393-410.

Kaya U., Tuniyev B., Ananjeva N., Orlov N., Papenfuss T., Kuzmin S., Tarkhnishvili D., Tuniyev S., Sparreboom M., Ugurtas I., and Anderson S. (2009). *Mertensiella caucasica*. The IUCN Red List of Threatened Species 2009: e.T13198A3418986.

Kurdíková V., Smolinský R., and Gvoždík L. (2011). Mothers matter too: Benefits of temperature oviposition references in newts. PLoS One, 6(8): e23842.

Langton T. E. S., Beckett C. L., and Foster J. P. (2001). Great crested newt conservation handbook. Froglife, Halesworth.

Muskhelishvili T. A. (1964). New findings about reproduction of the Caucasus salamander (*Mertensiella caucasica*). Soobsch Akad Nauk Gruz SSR, 36(1): 183-185.

Pearlson O. and Degani G. (2011). Water and ecological conditions of striped newt, *Triturus v. vittatus* (Urodela), breeding sites at various altitudes near the southern limit of its distribution. Herpetologica Romanica, 5: 27-42.

Rafińska A. (1991). Reproductive biology of the fire-bellied toads, *Bombina bombina* and *B. variegata* (Anura: Discoglossidae): egg size, clutch size and larval period length differences. Biological Journal of Linnean Society, 43(3): 197-210.

Rowe L. and Ludwig D. (1991). Variation in size and timing of metamorphosis in complex life histories. Ecology, 72: 413-427.

Sayım F., Başkale E., Tarkhnishvili, D., and Kaya U. (2009). Some water chemistry parameters of breeding habitats of the Caucasian salamander, *Mertensiella caucasica* in the Western Lesser Caucasus. Comptes Rendus Biologies, 332(5): 464-469.

Sih A. and Moore R. D. (1993). Delayed hatching of salamander eggs in response to enhanced larval predation risk. The American Naturalist, 142(6): 947-960.

Tarkhnishvili D. N. and Serbinova I. A. (1993). The ecology of the Caucasian Salamander (*Mertensiella caucasica* Waga) in a local population. Asiatic Herpetological Research, 5: 147-165.

Tarkhnishvili D. N. (1994). Interdependences between populational, developmental and morphological features of the Caucasian Salamander, *Mertensiella caucasica*. Mertensiella, 4: 315-325.

Tarkhnishvili D. N. (1996). The distribution and ecology of the amphibians of Georgia and the Caucasus: a biogeographical analysis. Zeitschrift für Feldherpetologie, 3: 167-196.

Tarkhnishvili D. N. and Serbinova I. A. (1997). Normal development of the Caucasian Salamander (*Mertensiella caucasica*). Advances in Amphibian Research in the Former Soviet Union. 2: 13-30.

Tarkhnishvili D. N., Kaya U., Gavashelishvili A., and Serbinova, I. (2008). Ecological divergence between two evolutionary lineages of the Caucasian Salamander: Evidence from the GIS analysis. Herpetological Journal, 18: 155-163.

Tarkhnishvili D. N. and Kaya U. (2009). Status and conservation of the Caucasian Salamander (*Mertensiella*

caucasica). In: N. Zazanashvili and D. Mallon (eds.), Status and protection of globally threatened species in the Caucasus. CEPF, WWF, Contour Ltd., Tbilisi, pp. 157-164.

Verrell P. A. and Francillon H. (1986). Body size, age and reproduction in the Smooth newt, *Triturus vulgaris*. Journal of Zoology, 210: 89-100.

Vučić C., Ivanović A., Nikolić S., Jovanović J., and Cvijanović M. (2020). Reproductive characteristics of two *Triturus* species (Amphibia: Caudata). Archives of Biological Sciences, 72(3): 321-328.

Werner E. E. (1986). Amphibian metamorphosis: growth rate, predation risk and the optimal size at transformation. American Naturalist, 128: 319-341.

ADVANCED APPLICATIONS OF TRANSITION METAL-BASED MATERIALS FOR ELECTROCATALYSIS

Yasemin TORLAK[1]

1. INTRODUCTION

Fossil fuels are generally used as the main energy source, and it is known that fossil fuels will run out in the near future. In addition, the damage caused by the use of fossil fuels to the environment and human health is known by almost all masses. Therefore, energy problems arising from the depletion of fossil fuels will definitely increase the huge demand for clean energy. Hydrogen energy is promising in this respect because the combustion reaction releases high amounts of energy and it is an environmentally friendly fuel (Li et al. 2021; You and Sun 2018). As a result of the negative effects of non-renewable resources, researchers have begun to investigate renewable resources, which are very important for the future of the world, by working in various fields to ensure the long-term sustainability of energy and humanity. Concern about countries' energy dependency and increasingly dangerous global climate change lead societies to seek alternative clean energy sources. Although renewable energy sources such as biomass, geothermal, solar and wind energy are abundant and clean energy sources, these energy sources need an intermediate carrier. For this reason, they do not have usability, especially in

---

[1] Öğr. Gör. Dr. Yasemin TORLAK, Pamukkale University, Cal Vocational High School, Denizli, Turkey, e-mail: ytorlak@pau.edu.tr, ORCID: 0000-0001-5964-2532.

applications requiring transportation. Can be produced from fossil fuels, water and biomass

Hydrogen is a good energy carrier for such energy sources. Also hydrogen; It stands out with its low volume, high storage capacity, efficiency and environmentally friendly nature. From this perspective, it can be said that the appropriate solution is "hydrogen", a promising energy carrier. Hydrogen, an environmentally friendly, green and efficient energy, is being evaluated as a clean energy source that can cope with this potential crisis. In renewable energy applications for sustainable development. The application of electrocatalysis plays a very important role, including storage, transformation and utilization. As a clean energy source, for example, hydrogen can be produced from the splitting of water via the electrocatalytic hydrogen evolution reaction (HER) and oxygen evolution reaction (OER).(Greeley and Markovic 2012; Zhao, Adair, and Sun 2019a) Because it provides a suitable alternative to produce clean energy sources, which include two half reactions, hydrogen evolution reaction (HER) and oxygen evolution reaction (OER) [5], which occur by electrocatalytically splitting water into hydrogen and oxygen.

Water electrolysis in alkaline media occurs through two half-cell reactions:. The first of these is the oxidation of water at the anode ($4OH^- \rightarrow 2H_2$ (g) + $2H_2O + 4e^-$), which is known as the oxygen evolution reaction (OER), that is, the reduction reaction of water. The other is the ion at the cathode ($4H_2O + 4e^- \rightarrow 2H_2(g) +, 4OH^-$) also known as the hydrogen evolution reaction (HER). (Jamesh and Sun 2018) In the anodic OER reaction, the splitting of water occurs due to four electron transfer processes and O-O bond formation. As reference catalysts, noble metal oxides (RuO_2 and IrO_2) are selected for OER. However, their large-scale application is hampered by high cost and relatively low long-term stability. Therefore, the

development of non-noble metal-based electrocatalysts for OER is of great importance.(Roger, Shipman, and Symes 2017)

Oxygen evolution reaction (OER) is an important half reaction usually involved in sustainable energy conversion technology applications. Transition metals play an important role in carrying out these reactions.(Zhao, Adair, and Sun 2019b) Especially in the last few years, the electrocatalytic oxygen evolution reaction (OER) has an important place among electrode reactions. In addition, it has been the focus of attention in the development of catalysts that are both efficient and more cost-effective in photoelectrochemical cell studies. The stability of transition group metal oxides during the reaction and their easy synthesis make them good candidates as electrocatalysts. Especially while these reactions take place, structural transformations such as surface amorphization of some metal oxides and surface oxidation of metal oxide compounds are very important. In this review, the latest developments in the production of transition metal-based materials for the hydrogen evolution reaction (HER) and oxygen evolution reaction (OER) and their use as catalysts in electrolytic applications are summarized. In addition, information was given about information that would contribute to understanding the structural transformation in the mechanism involving metal oxide-based OER electrocatalysts for a better understanding of catalytic mechanisms and that would benefit the design of high-activity catalytic materials to be produced from now on. Some environmental factors affect the structural stability of metal oxides and changes during the OER reaction have been examined. Some general information is presented outlining which factors affect this structural change process. Oxides (Grimaud et al. 2017; Song et al. 2018), (oxy)hydroxides (Huang et al. 2015; Zhan et al. 2015), sulfides (Xu et al. 2020), selenides (Liu et al. 2014; Xia et al. 2016), phosphides(Jiang et

al. 2015), phosphates(Huang et al. 2018)   are known as effective electrocatalysts for OER. Among electrocatalysts, transition metal hydroxides are the most well-known electrocatalysts because they can be easily prepared and have high activity (Deng and Tüysüz 2014; Hutchings et al. 2015).

Basic salts of the transition metal group can generally be formulated as $M^{2+}(OH)^{2-}{}_x(A^{m-})x/m$. If it has another anion such as $nH_2O(A = CO_3{}^{2-}, NO_3{}^-, F^-, Cl^-$, etc.), it is expressed this way when compared to transition metal hydroxides. In addition, these basic salts of the transition metal contain abundant base active sites, unique channel structures and special electronic configurations, which enable them to increase OER performance. In this way, a very important step will be taken to develop low-cost, non-precious metal-based electrocatalysts in electrocatalytic applications for water separation and commercialization of water electrolysis.

In conclusion, studies have shown that one of the most promising catalysts for OER is the use of transition metal basic salts in the electrocatalytic system. However, more detailed and comprehensive studies on these transition metal basic salts are required. This review summarizes all the important points needed for the separation of minerals and OER in transition metal basic salt-based electrocatalysts. All readers of this review will gain a better understanding of how to improve concepts such as structure, composition, and efficiency for electrocatalytic application, as well as methodically provide basic guidelines for the creation of molecular electrocatalysts for storing the resulting energy and its transformation into different states.

2. TRANSITION METAL BASIC SALTS FOR OER AND WATER SLITTING

In general, it is known in this section that the properties, energy conversion and catalytic performance of transition metal basic salts depend on the anion typeIn general, it is known in this section that the properties, energy conversion and catalytic performance of transition metal basic salts depend on the anion type. In particular, it is summarized how important the impact of these anions is on OER performance. During the OER reaction, it is observed that a certain part or all of the transition metal basic salts undergo oxidation, depending on the reactants involved. Obtaining bifunctional electrocatalysts that can be effective simultaneously during HER and OER reactions will be remarkable in practical applications. It is very important to conduct research on the applications in which these salts will be included as catalysts, their catalytic activities and how they will benefit HER reactions. Thanks to these researches, it is easier to determine whether metal basic salts or metal hydroxides are more suitable for transition to these reactions (Dai et al. 2020). There are not many detailed reports on the general partitioning of water into pure transition metal basic salts for OER and HER due to their weak intrinsic activity. In particular, in order to increase this electrocatalyst property, the crystal structures of transition metals and their synergistic interactions for application should be examined in detail. Moreover, different modification strategies have been implemented to improve the HER activity of metal basic salts, including morphology crystal structure or size design (Lu et al. 2019), modulation of electronic structure (Hui et al. 2019), and interface engineering (S. Q. Liu et al. 2021). As a result, bimetallic and heterostructured basic salts have generally been preferred as HER and other water splitting catalysts. In this section,

information is given about the developments of modified transition metal basic salts in recent years.

Figure 1. Summary Scheme of Structures of Transition Metal Basic Salts for HER and OER
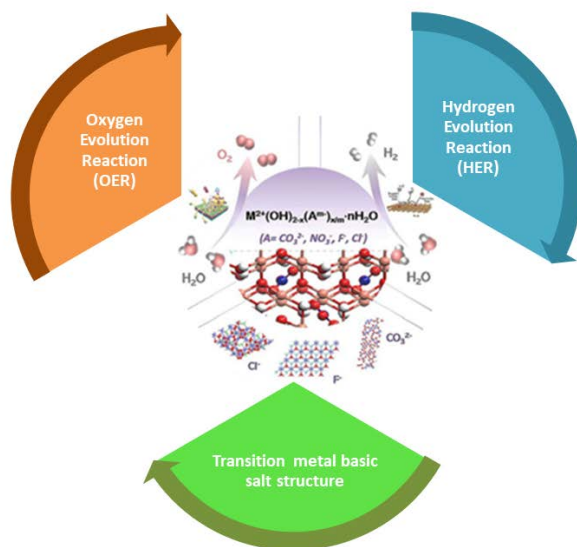
Many transition metals whose oxidation state can be easily changed can be used as catalysts. However, there are very few transition metals with lower overvoltages than platinum. Although platinum's struggle to become the best catalyst continues, its use is gradually decreasing. But today there are special applications for making small crystals, and excellent catalysts can be made with coatings of a few mg/cm2 on graphite. In addition, studies on the electrocatalytic reduction of oxygen have focused on various oxides such as cobaltites, delafocytes and perovskites. Fe and Co phthalocyanines and porphyrins adsorbed in solution or on the carbon surface are also studied catalysts for oxygen release.

Apart from these, other transition metals, for example, can be used as electrode materials in electrochemical determinations because they provide the low potential required to oxidize aliphatic alcohols. Nickel, cobalt and copper catalyze oxidation processes at the electrode due to the formation of oxy hydroxides. Therefore, mono, di and trisaccharides can be determined successfully from the sample with chemically modified electrodes made using Ni and Co. Another development in this field is that the electrocatalytic behavior of chemically modified electrodes made of Ni and Co can be examined with electrochemical techniques, X-ray photoelectron spectroscopy and scanning electron microscopy. In addition, modified glassy carbon or carbon powders with metal and metal oxide catalysts; Another important point is the use of electroactive analytes such as carbohydrates, amino acids and sulfhydryl compounds for the determination of constant potential amperometry.(Deng and Tüysüz 2014; Song et al. 2018; Zhang et al. 2018, 2021)

3. REACTION MECHANISM

A brief summary of the mechanism of OER on transition metal oxides in alkaline media is shown in Figure 1. Here "M" represents the active site. In the first step, an OH⁻ radical is introduced into the active site to obtain M-OH by one-electron oxidation of the OH⁻ anion. (Suen et al. 2017) Then, combined proton and electron removals from M-OH yield M-O. As a result of the nucleophilic attack of the OH⁻ anion on M-O combined with an electron oxidation, the hydroperoxide intermediate M-OOH is obtained. Another proton-coupled electron transfer causes O_2 to be released into the medium and the free active site to be renewed. Then, the combination of the two M-O species directly gives the result O_2 and M. The

mechanism briefly outlined here underlies most of the proposed OER mechanisms. (Song et al. 2018; Suntivich et al. 2011)

Figure 2. A Brief Summary of the OER Mechanism
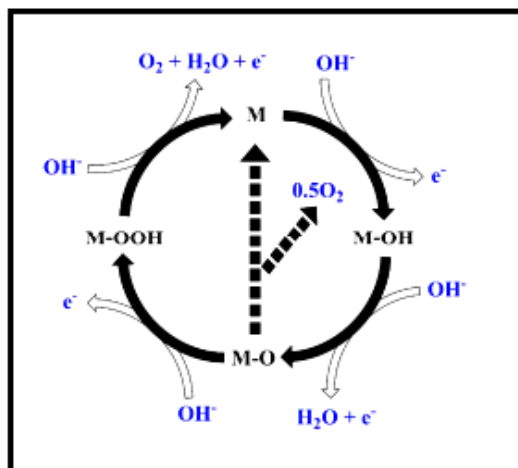
4. ADVANCED IN ELECTROCHEMICAL TUNİNG PROPERTİES

4.1.Electrochemical Tuning Devices

Electronic structure tuning of an electrocatalyst is one of the most effective strategies to increase its efficiency during the water electrolysis process. Accordingly, electrocatalysts containing multiple metals are more advantageous in tuning their electronic structures compared to those containing single metals. Lithium-ion batteries (LIBs) are the most suitable reactors in which small size lithium ions are combined with different parent materials and used as intermediaries to react with catalysts in electrolytes of organic nature for electrochemical tuning.

In the field of catalysis, LIB applications have a wide potential window and the inclusion of transition metal-based compounds into the structure and act as a multifunctional

structure provides a difference. It has been shown that Li-S batteries may also be suitable for electrochemical tuning like LIBs. Additionally, metal oxide cathodes can be used for Zn-based batteries for electrochemical tuning. LIB has a wider potential window than zinc-based battery applications, however, zinc-based batteries provide easier adaptation to ambient atmospheres with aqueous electrolytes and easier use without the need for airtight environments (Lu et al. 2018; Meng et al. 2018). Electrochemical tuning device configurations generally include column batteries, Swagelok cells, button batteries and pouch cells. Of these configurations, the cells most commonly installed in electrochemistry laboratories are coin cells, and these cells are compatible with LIBs, ZBs, and metal-air batteries. Button batteries are easy to install and stable for testing. However, small material loadings may only be suitable for experimental studies. Structural and morphological damage may occur during catalytic application, and negative experimental results may also occur due to material contamination. Like coin-type cells, columnar (Zhang et al. 2018) and Swagelok type (Guo et al. 2019) batteries may also experience some problems due to material contamination during device transfer. To eliminate these problems, using a Li-MnO$_2$ cell as a button cell or a Li-O$_2$ battery for bifunctional electrocatalysis is preferred for electrochemical tuning as they have similar structures except for oxygen entry.

4.2. Electrochemical Tuning Based on Conversion Reactions

Conversion reactions were carried out using Li cells to convert CuO microspheres into Cu nanoparticles (NPs). Electrochemical mill (ECM) was used for this (Zhang et al. 2005). Electrochemically reduced metal (M) is formed as a result of the reaction between transition meal oxides and lithium MO + 2Li$^+$ + 2e$^-$ ↔ M + Li$_2$O) during discharge. The formation

of M/Li$_2$O nanocomposites prevents the unstable progression of Li$_2$O matrices (Li et al. 2019). The obtained M and Li$_2$O are trapped in the nanoporous structure and their structure is preserved here. Since the transformation reactions in LIBs occur reversibly, a larger active surface area occurs with this metal oxide structure, which has high porosity. For example, thanks to this method, metallic Pt nanoparticles of 2-8 nm size with 78% nanoporosity are obtained and this structure is then oxidized with methanol. It acts as an electrocatalyst in reactions. A different study showed that Cu nanoparticles were obtained by the conversion reaction of CuO and the contributing factors were investigated (Zhang et al. 2008). By controlling conditions such as current discharge density and operating temperature, it is examined how the morphology of Cu changes depending on this reaction. As a result of the research, it has been reported that smaller sized Cu nanoparticles are formed at a temperature as low as 0°C and at low current densities such as below 0.064 mAcm^{-2}. By using electrochemical tuning configurations and methods based on the transformation reaction, the growth rate, size and morphology of the crystal structure can also be controlled.

4.3. Electrochemical Tuning Based on Insertion Reactions

Lithium content can be quantitatively adjusted to certain extents through electrochemical addition reactions. Structural features and content ratios of the main hosts are preserved. Mobile guest ions are reversibly incorporated or deintercalated into or out of these host material structures. These addition reactions were implemented in the first commercial LIB application, which enabled the addition of lithium to layered titanium disulfide in the first Li-based battery and was based on the addition of Li$^+$ between the graphite anode and LiCoO$_2$ cathode (Zhang et al. 2008). The small size of the Li$^+$ ion makes

it easier for it to adjust the properties of the parent material, such as crystallographic phase and electronic structure, and allows it to settle into van der Waals spaces more easily. For example, MoS_2 and WS_2 can exfoliate because they have weakly bonded planes. Zhang et al. tried to optimize the disadvantages of chemical insertion methods by considering factors such as poor controllability of the degree of lithium intercalation, high reaction temperature and long processing time. As a result, they proposed the electrochemical lithiation process to control exfoliation under normal conditions (F. Liu et al. 2021). Cui et al. has made it more comprehensive by applying electrochemical adjustment processes in aqueous HER and OER environments through lithium intercalation or deintercalation in organic electrolytes. For example, in different studies, different electrode materials with 1D channels such as polyanionic metal phosphates or 3D channels such as pinel-type lithium metal oxides have been incorporated into addition reactions for ionic diffusion to produce active electrocatalysts (Lu et al. 2018).

5. CONSTRUCTION OF METAL OXIDE-BASED HETEROSTRUCTURE/COMPOSITES

In addition to adjusting the activity of transition metal basic salts in HER or OER reactions, forming transition metal basic compıunds and electrocatalytic materials for the separation of OER and HER and water can be considered as another effective strategy. The aim of these reactions is to ensure the formation of the heterostructure of active materials and to develop materials such as metal basic salts and Pt group metal nanoparticles, metal sulphides, nitrides and carbides, thus ensuring that both their physical and chemical properties are adjusted according to the application. Two methods are used to increase the performance of electrode materials. The first of

these is to increase the exchange current density, and the second is to increase the active surface area of the electrode. In practice, both methods are used. Although noble metals show the highest catalytic activity in this process, the fact that noble metals are expensive and the electrode surfaces passivate very quickly and lose their activity over time limits their usage areas on a large-scale industrial scale. Nanocomposites obtained by dispersing metal nanoparticles into a conductive polymer matrix are another research topic that has been studied intensively in recent years. With these hybrid nano-materials, physically more stable and chemically more reactive structures are obtained and catalytic active materials are developed in many processes. It is known that nano-sized metals show much higher catalytic activity compared to larger-sized metal particles. Reducing the costs of electrode materials by coating cheaper metals such as nickel, copper, titanium and tungsten with platinum or by developing electrocatalysts obtained by dispersing platinum micro particles into the polymer matrix is one of the important goals of electrochemical technology in industrial applications. Moreover, although many methods are used in the preparation of platinum-based materials in the literature, the cheapest and simplest method among them is the electrochemical method. (Habibi et al. 2008)

Cretu et al. investigated the catalytic effects of aniline and benzylamine used in different amounts on hydrogen formation at the platinum electrode, in an electrolyte environment containing sulfuric acid, and found that the exchange current density increased as the amine concentration increased. They explained this result with the increasing proton concentration at the metal-solution interface due to hydrogenation of nitrogen atoms.(Crețu, Kellenberger, and Vaszilcsin 2013)

Corte et al. (2012) examined the catalytic hydrogen formation reaction on Ni-Pani composite electrodes prepared by the electrodeposition method. From the linear Tafel polarization curves, they stated that the hydrogen evolution reaction proceeds through the Volmer step and, according to the results of electrochemical impedance spectroscopy, it catalyzes the PAni reaction on the nickel electrode.(Dalla Corte et al. 2012) Today, it is known that the most active catalysts in electrocatalytic hydrogen production are Pt group metals, but their use as solid metal electrodes is limited due to the high costs of these metals (Habibi et al. 2008; Rao and Trivedi 2005; Winther-Jensen et al. 2010). Therefore, new lower-cost electrodes need to be developed for the HER. There is an increasing number of studies in the literature examining the electrolytic hydrogen formation reaction in electrodes modified with different metals, metal oxides and different conductive polymers.

For HER, it makes more sense to combine transition metal basic salts and non-noble metal-based catalysts as they are cheaper in price than noble metal-based materials. For example, Luo and co-workers synthesized a 3D hierarchical heterostructured $Cu_3N@CoNiCHs@copper$ foam electrode material by the hydrothermal method. They explained that the material they synthesized was an effective catalyst for the general decomposition of water. Thanks to the synergistic interaction between the Cu3N compound, which has electron-rich Cu regions, and the CoNiCH compound, which has electron-deficient Co regions, a composite with higher OER and HER activity was obtained. Thanks to this composite, the $Cu_3N@CoNiCHs@CF$ electrode was advantageous as it required a low cell voltage of 1.58 V to reach 10 mAcm^{-2} (S. Q. Liu et al. 2021).

6. CONCLUSIONS AND FUTURE PERSPECTİVES

The simplest method of obtaining hydrogen, which is accepted as the energy of the future as an alternative and clean energy source, is the electrolysis of water. However, overvoltage occurring in the electrochemical system increases the cost of the method and thus reduces its applicability. In this respect, the development of electrode materials with low overvoltage, high catalytic activity and stability over time is a very important issue in electrochemical systems. One of the most practical and preferred ways to produce hydrogen is the electrochemical decomposition of water. Among the types of electrocatalysts studied so far for electrochemical water splitting, transition metal oxide compounds are the latest to improve electrocatalytic OER and HER due to their well-defined and highly versatile porous structures, large surface area, distinctive physicochemical properties, as well as their outstanding chemical and mechanical stability advantages. It has attracted great attention in recent times and provides superiority over traditional heterogeneous catalysts.

In this review, various electrochemical tuning methods are summarized for the more comprehensive development of electrocatalysts. Electrochemical tuning can be preferred as a method for activating electrochemically inactive materials by selecting appropriate conditions, as the potential in existing electrocatalysts is both easy and effective in optimizing the conditions. It is essential to adjust the crystallinity and cage types, electronic structures, and crystal phases electrochemically by adapting the size and morphology of the compounds in the structure in order to increase the electrocatalytic activity. However, care must be taken when performing electrochemical adjustment as it may affect many properties of the electrode materials at the same time. In addition to these advantages, one

of the current problems that need to be solved is the negative effects of electrochemical adjustment and transfer of materials between electrocatalytic devices, such as mass loss, structural damage and atmospheric pollution. The other is negative situations such as the removal of some conductive additives or the separation of binders during the purification processes of active materials before being incorporated into the electrocatalytic electrodes. Installations should be designed where electrochemical adjustment and electrocatalysis reactions can occur simultaneously. These issues should be taken into account in future research and development on this topic.

REFERENCES

Creţu, Raluca, Andrea Kellenberger, and Nicolae Vaszilcsin. 2013. "Enhancement of Hydrogen Evolution Reaction on Platinum Cathode by Proton Carriers." *International Journal of Hydrogen Energy* 38(27):11685–94. doi: 10.1016/j.ijhydene.2013.07.004.

Dai, Mimi, Haiyan Fan, Guoguang Xu, Min Wang, Si Zhang, Luhua Lu, and Yuegang Zhang. 2020. "Boosting Electrocatalytic Oxygen Evolution Using Ultrathin Carbon Protected Iron–Cobalt Carbonate Hydroxide Nanoneedle Arrays." *Journal of Power Sources* 450(November 2019):227639. doi: 10.1016/j.jpowsour.2019.227639.

Dalla Corte, Daniel A., Camila Torres, Patricia Dos Santos Correa, Ester Schmidt Rieder, and Célia De Fraga Malfatti. 2012. "The Hydrogen Evolution Reaction on Nickel-Polyaniline Composite Electrodes." *International Journal of Hydrogen Energy* 37(4):3025–32. doi: 10.1016/j.ijhydene.2011.11.037.

Deng, Xiaohui, and Harun Tüysüz. 2014. "Cobalt-Oxide-Based Materials as Water Oxidation Catalyst: Recent Progress and Challenges." *ACS Catalysis* 4(10):3701–14. doi: 10.1021/cs500713d.

Greeley, Jeffrey, and Nenad M. Markovic. 2012. "The Road from Animal Electricity to Green Energy: Combining Experiment and Theory in Electrocatalysis." *Energy & Environmental Science* 5(11):9246. doi: 10.1039/c2ee21754f.

Grimaud, Alexis, Oscar Diaz-Morales, Binghong Han, Wesley T. Hong, Yueh Lin Lee, Livia Giordano, Kelsey A. Stoerzinger, Marc T. M. Koper, and Yang Shao-Horn. 2017. "Activating Lattice Oxygen Redox Reactions in Metal Oxides to Catalyse Oxygen Evolution." *Nature Chemistry* 9(5):457–65. doi: 10.1038/nchem.2695.

Guo, Yuanyuan, Zhengfei Dai, Jun Lu, Xiaoqiao Zeng, Yifei Yuan, Xuanxuan Bi, Lu Ma, Tianpin Wu, Qingyu Yan, and Khalil Amine. 2019. "Lithiation-Induced Non-Noble Metal Nanoparticles for Li-O 2 Batteries." *ACS Applied Materials and Interfaces* 11(1):811–18. doi: 10.1021/acsami.8b17417.

Habibi, B., M. H. Pournaghi-Azar, H. Razmi, and H. Abdolmohammad-Zadeh. 2008. "Electrochemical Preparation of a Novel, Effective and Low Cast Catalytic Surface for Hydrogen Evolution Reaction." *International Journal of Hydrogen Energy* 33(11):2668–78. doi: 10.1016/j.ijhydene.2008.03.014.

Huang, Jianwen, Yinghui Sun, Yadong Zhang, Guifu Zou, Chaoyi Yan, Shan Cong, Tianyu Lei, Xiao Dai, Jun Guo, Ruifeng Lu, Yanrong Li, and Jie Xiong. 2018. "A New Member of Electrocatalysts Based on Nickel Metaphosphate Nanocrystals for Efficient Water

Oxidation." *Advanced Materials* 30(5):1–9. doi: 10.1002/adma.201705045.

Huang, Junheng, Junting Chen, Tao Yao, Jingfu He, Shan Jiang, Zhihu Sun, Qinghua Liu, Weiren Cheng, Fengchun Hu, Yong Jiang, Zhiyun Pan, and Shiqiang Wei. 2015. "CoOOH Nanosheets with High Mass Activity for Water Oxidation." *Angewandte Chemie - International Edition* 54(30):8722–27. doi: 10.1002/anie.201502836.

Hui, Lan, Dianzeng Jia, Huidi Yu, Yurui Xue, and Yuliang Li. 2019. "Ultrathin Graphdiyne-Wrapped Iron Carbonate Hydroxide Nanosheets toward Efficient Water Splitting." *ACS Applied Materials and Interfaces* 11(3):2618–25. doi: 10.1021/acsami.8b01887.

Hutchings, Gregory S., Yan Zhang, Jian Li, Bryan T. Yonemoto, Xinggui Zhou, Kake Zhu, and Feng Jiao. 2015. "In Situ Formation of Cobalt Oxide Nanocubanes as Efficient Oxygen Evolution Catalysts." *Journal of the American Chemical Society* 137(12):4223–29. doi: 10.1021/jacs.5b01006.

Jamesh, Mohammed Ibrahim, and Xiaoming Sun. 2018. "Recent Progress on Earth Abundant Electrocatalysts for Oxygen Evolution Reaction (OER) in Alkaline Medium to Achieve Efficient Water Splitting – A Review." *Journal of Power Sources* 400(July):31–68. doi: 10.1016/j.jpowsour.2018.07.125.

Jiang, Nan, Bo You, Meili Sheng, and Yujie Sun. 2015. "Electrodeposited Cobalt-Phosphorous-Derived Films as Competent Bifunctional Catalysts for Overall Water Splitting." *Angewandte Chemie - International Edition* 54(21):6251–54. doi: 10.1002/anie.201501616.

Li, Jing, Sooyeon Hwang, Fangming Guo, Shuang Li, Zhongwei

Chen, Ronghui Kou, Ke Sun, Cheng Jun Sun, Hong Gan, Aiping Yu, Eric A. Stach, Hua Zhou, and Dong Su. 2019. "Phase Evolution of Conversion-Type Electrode for Lithium Ion Batteries." *Nature Communications* 10(1). doi: 10.1038/s41467-019-09931-2.

Li, Siwei, Peng Miao, Yuanyuan Zhang, Jie Wu, Bin Zhang, Yunchen Du, Xijiang Han, Jianmin Sun, and Ping Xu. 2021. "Recent Advances in Plasmonic Nanostructures for Enhanced Photocatalysis and Electrocatalysis." *Advanced Materials* 33(6):1–19. doi: 10.1002/adma.202000086.

Liu, Fangming, Le Zhang, Lei Wang, and Fangyi Cheng. 2021. "The Electrochemical Tuning of Transition Metal-Based Materials for Electrocatalysis." *Electrochemical Energy Reviews* 4(1):146–68. doi: 10.1007/s41918-020-00089-w.

Liu, Shao Qing, Min Rui Gao, Subiao Liu, and Jing Li Luo. 2021. "Hierarchically Assembling Cobalt/Nickel Carbonate Hydroxide on Copper Nitride Nanowires for Highly Efficient Water Splitting." *Applied Catalysis B: Environmental* 292(December 2020):120148. doi: 10.1016/j.apcatb.2021.120148.

Liu, Youwen, Hao Cheng, Mengjie Lyu, Shaojuan Fan, Qinghua Liu, Wenshuai Zhang, Yuduo Zhi, Chengming Wang, Chong Xiao, Shiqiang Wei, Bangjiao Ye, and Yi Xie. 2014. "Low Overpotential in Vacancy-Rich Ultrathin CoSe2 Nanosheets for Water Oxidation." *Journal of the American Chemical Society* 136(44):15670–75. doi: 10.1021/ja5085157.

Lu, Wangting, Xuwen Li, Feng Wei, Kun Cheng, Wenhui Li, Youhua Zhou, Wanquan Zheng, Lei Pan, and Geng Zhang. 2019. "Fast Sulfurization of Nickel Foam-

Supported Nickel-Cobalt Carbonate Hydroxide Nanowire Array at Room Temperature for Hydrogen Evolution Electrocatalysis." *Electrochimica Acta* 318:252–61. doi: 10.1016/j.electacta.2019.06.088.

Lu, Zhiyi, Kun Jiang, Guangxu Chen, Haotian Wang, and Yi Cui. 2018. "Lithium Electrochemical Tuning for Electrocatalysis." *Advanced Materials* 30(48):1–8. doi: 10.1002/adma.201800978.

Meng, Jing, Fangming Liu, Zhenhua Yan, Fangyi Cheng, Fujun Li, and Jun Chen. 2018. "Spent Alkaline Battery-Derived Manganese Oxides as Efficient Oxygen Electrocatalysts for Zn-Air Batteries." *Inorganic Chemistry Frontiers* 5(9):2167–73. doi: 10.1039/c8qi00404h.

Rao, Chepuri R. K., and D. C. Trivedi. 2005. "Chemical and Electrochemical Depositions of Platinum Group Metals and Their Applications." *Coordination Chemistry Reviews* 249(5–6):613–31. doi: 10.1016/j.ccr.2004.08.015.

Roger, Isolda, Michael A. Shipman, and Mark D. Symes. 2017. "Earth-Abundant Catalysts for Electrochemical and Photoelectrochemical Water Splitting." *Nature Reviews Chemistry* 1. doi: 10.1038/s41570-016-0003.

Song, Fang, Lichen Bai, Aliki Moysiadou, Seunghwa Lee, Chao Hu, Laurent Liardet, and Xile Hu. 2018. "Transition Metal Oxides as Electrocatalysts for the Oxygen Evolution Reaction in Alkaline Solutions: An Application-Inspired Renaissance." *Journal of the American Chemical Society* 140(25):7748–59. doi: 10.1021/jacs.8b04546.

Suen, Nian Tzu, Sung Fu Hung, Quan Quan, Nan Zhang, Yi Jun Xu, and Hao Ming Chen. 2017. "Electrocatalysis for the

Oxygen Evolution Reaction: Recent Development and Future Perspectives." *Chemical Society Reviews* 46(2):337–65. doi: 10.1039/c6cs00328a.

Suntivich, Jin, Kevin J. May, Hubert A. Gasteiger, John B. Goodenough, and Yang Shao-Horn. 2011. "A Perovskite Oxide Optimized for Oxygen Evolution Catalysis from Molecular Orbital Principles." *Science* 334(6061):1383–85. doi: 10.1126/science.1212858.

Winther-Jensen, Bjorn, Kevin Fraser, Chun Ong, Maria Forsyth, and Douglas R. MacFarlane. 2010. "Conducting Polymer Composite Materials for Hydrogen Generation." *Advanced Materials* 22(15):1727–30. doi: 10.1002/adma.200902934.

Xia, Chuan, Qiu Jiang, Chao Zhao, Mohamed N. Hedhili, and Husam N. Alshareef. 2016. "Selenide-Based Electrocatalysts and Scaffolds for Water Oxidation Applications." *Advanced Materials* 28(1):77–85. doi: 10.1002/adma.201503906.

Xu, Yijie, Afriyanti Sumboja, Yun Zong, and Jawwad A. Darr. 2020. "Bifunctionally Active Nanosized Spinel Cobalt Nickel Sulfides for Sustainable Secondary Zinc-Air Batteries: Examining the Effects of Compositional Tuning on OER and ORR Activity." *Catalysis Science and Technology* 10(7):2173–82. doi: 10.1039/c9cy02185j.

You, Bo, and Yujie Sun. 2018. "Innovative Strategies for Electrocatalytic Water Splitting." *Accounts of Chemical Research* 51(7):1571–80. doi: 10.1021/acs.accounts.8b00002.

Zhan, Yi, Guojun Du, Shiliu Yang, Chaohe Xu, Meihua Lu, Zhaolin Liu, and Jim Yang Lee. 2015. "Development of

Cobalt Hydroxide as a Bifunctional Catalyst for Oxygen Electrocatalysis in Alkaline Solution." *ACS Applied Materials and Interfaces* 7(23):12930–36. doi: 10.1021/acsami.5b02670.

Zhang, D. W., C. H. Chen, J. Zhang, and F. Ren. 2005. "Novel Electrochemical Milling Method to Fabricate Copper Nanoparticles and Nanofibers." *Chemistry of Materials* 17(21):5242–45. doi: 10.1021/cm051584c.

Zhang, Da Wei, Chun Hua Chen, Jin Zhang, and Fei Ren. 2008. "Fabrication of Nanosized Metallic Copper by Electrochemical Milling Process." *Journal of Materials Science* 43(4):1492–96. doi: 10.1007/s10853-007-2274-6.

Zhang, Xian, Renji Zheng, Mengtian Jin, Run Shi, Zhong Ai, Abbas Amini, Qing Lian, Chun Cheng, and Shaoxian Song. 2021. "NiCoS X@Cobalt Carbonate Hydroxide Obtained by Surface Sulfurization for Efficient and Stable Hydrogen Evolution at Large Current Densities." *ACS Applied Materials and Interfaces* 13(30):35647–56. doi: 10.1021/acsami.1c07504.

Zhang, Xiao, Zhimin Luo, Peng Yu, Yongqing Cai, Yonghua Du, Daoxiong Wu, Si Gao, Chaoliang Tan, Zhong Li, Minqin Ren, Thomas Osipowicz, Shuangming Chen, Zheng Jiang, Jiong Li, Ying Huang, Jian Yang, Ye Chen, Chung Yen Ang, Yanli Zhao, Peng Wang, Li Song, Xiaojun Wu, Zheng Liu, Armando Borgna, and Hua Zhang. 2018. "Lithiation-Induced Amorphization of Pd3P2S8 for Highly Efficient Hydrogen Evolution." *Nature Catalysis* 1(6):460–68. doi: 10.1038/s41929-018-0072-y.

Zhao, Yang, Keegan Adair, and Xueliang Sun. 2019a. "Toward Clean Energy Devices: From a Fundamental

Understanding to Practical Applications." *Matter* 1(5):1119–26. doi: 10.1016/j.matt.2019.10.016.

Zhao, Yang, Keegan Adair, and Xueliang Sun. 2019b. "Toward Clean Energy Devices: From a Fundamental Understanding to Practical Applications." *Matter* 1(5):1119–26. doi: 10.1016/j.matt.2019.10.016.

A THEORETICAL STUDY ON THE SOLAR CELL MODELLED WITH CU₂SNS₃ FABRICATED BY SPIN COATING

Silan BATURAY[1]

Serap YIGIT GEZGIN[2]

Bedrettin MERCİMEK[3]

Hamdi Sukur KILIC[4]

1. INTRODUCTION

The limitations of typical sources with fossil fuels, as well as the ever-increasing worldwide need for energy, place a premium on energy conversion via solar technology, which should approach the terawatt scale. Photovoltaic (PV) market is based on solar cells manufactured with silicon (Si) wafer, copper (Cu) Indium (In) Gallium (Ga) Selenium (Se) (CIGS), and cadmium tellur (CdTe) materials. Some prominent disadvantages of these mentioned elements are the high cost of In, Ga and Te, and the high processing cost of Si as well as the toxicity of Cd element. Many researchers are interested in triple Cu-Sn-S(Se, Ge) polycrystalline structure system, which are I-IV-VI group semiconductors because of their optical, structural, thermal, morphological, electrical, and mechanical behaviors [1, 2].

---

[1] Doç. Dr., Dicle Üniversitesi/ Fen Fakültesi/ Fizik Bölümü, silanbaturay2019@gmail.com, ORCID ID: 0000-0002-8122-6671

[2] Doç. Dr., Selçuk Üniversitesi/ Fen Fakültesi/ Fizik Bölümü, serap.gezgin@selcuk.edu.tr, ORCID ID: 0000-0003-3046-6138

[3] Prof. Dr., Necmettin Erbakan Üniversitesi/ Eğitim Fakültesi/ Kimya Öğretmenliği, bmercimek@erbakan.edu.tr, ORCID ID: 0000-0002-3407-6906

[4] Prof. Dr., Selçuk Üniversitesi/ Fen Fakültesi/ Fizik Bölümü, hamdisukurkilic@selcuk.edu.tr, ORCID ID: 0000-0002-7546-4243.

Cu_2SnS_3, a *p*-type semiconductor compound, is used in solar cells suitable energy band gap width (between 0.93eV and 1.51eV) and high absorption coefficient ($>10^4$ cm^{-1}) [3, 4]. It is one of most important materials for solar energy conversion systems and PV applications [5, 6]. In addition, Cu_2SnS_3 contains eco-friendly elements, which are plentiful in the crust of earth and it does not indicate any toxic behaviors. Also Cu_2SnS_3 (CTS) is also one of the hopeful elements for lithium-ion batteries and photo-catalysis applications due to its conductivity and crystal structure at room temperature [7, 8].

A large number of investigations have been conducted to establish relationships between Cu_2SnS_3 materials deposition processes and the resulting structure, morphology, and electrical conduction. However, obtaining Cu_2SnS_3 in its pure kestrite phase is difficult for solar cell applications [9]. During the synthesis of Cu_2SnS_3, a variety of secondary and/or tertiary phases such as Cu_2S, SnS, and Cu_3SnS_4 were produced. Furthermore, band gap width, defects, and unregulated stoichiometry, as well as secondary or tertiary impurity phases, can all have an effect on the optoelectronic characteristics of Cu_2SnS_3 [10]. In the reports obtained so far, Cu_2SnS_3 samples formed using different physical and chemical samples deposition techniques; chemical bath deposition [11], sputtering [12], SILAR [13], spray pyrolysis [14], doctor blade [15], and spin coating [16]. Among these methods, spin coating stands out due to some advantages such as controllability, cheap, simple and easy to apply. It is a fabrication method and the magnification parameters are easy to determine and does not require vacuum atmosphere.

A modeling software system employed recently to determine the productivity of solar cell formed by layers has grown in relevance. A theoretical software SCAPS-1D, among others, is one of the most commonly and regularly used software

in this sector. PV behaviors of a solar cell have been calculated using physical aspects such as energy band width, electron affinity, and dielectric permittivity of solar cell layers, thickness of obtained thin film, contact work role, and so on.

It is an important critical investigation to establish how experimentally produced thin film affects efficiency by modeling it in the structure of solar cell using thin film characteristic parameters. In this work, a Cu_2SnS_3 at 30 sccm and 40 sccm sulphur flow rates samples-based solar cell is created and modeled using SCAPS-1D simulation program, and the influence of various rear connections on the productivity of solar cells generated for this work is explored, and the data obtained are evaluated. Crystal structure and optical properties are examined after annealing process. Thus, based on these criteria that have a major impact on efficiency, it has been concluded that consistent interpretations of solar cell behavior are attainable. As a consequence, because CTS is a novel material in solar cell applications, such a research on CTS solar cells with SCAPS program is very unusual in literature, and it can be assumed that this work will shed light on solar cell experimental efficiency enhancement investigations.

2. THE EXPERIMENTAL

In the current work, Cu_2SnS_3 (CTS) thin films with different annealing time at sulphur atmosphere were fabricated on cleaned glass substrate using a solution comprising 0.389 g copper (II) acetate ($Cu(CH_3COO)_2 \cdot H_2O$) (Purity $\geq$97%, Sigma/Aldrich), 0.220 g tin (II) chloride dehydrate ($SnCl_2.2H_2O$) (Purity $\geq$97%, Sigma/Aldrich), and 0.444 g thiourea (CH_4N_2S) (Purity 97%, Sigma/Aldrich) fabricated under optimized conditions. The molar ratios of Cu/Sn/S elements in the solutions were 2/1/3. Thiourea was added to stoichiometric requirement to

be compensated for the loss of sulfur. Each chemical is separately dissolved and then mixed with glacial acetic acid and ethanol for six hours at room temperature while being stirred magnetically. Tin (II) chloride dehydrate was added to the thiourea/copper (II) acetate solution after the thiourea solution had first been gradually blended into the copper (II) acetate solution. After that, the solutions were shaken for four hours at room temperature to produce a clear, homogenous solution.

Prior to the deposition process, the glass substrates were cleaned by boiling them in a sufficient amount of a mixture of NH_3, H_2O_2, and H_2O_2 at 105 °C. They were then rinsed in a suitable amount of HCl, H_2O_2, and H_2O_2 at 105 °C to remove any leftover waste. Following a three-minute cleaning in deionized water, the glass substrates were dried. The final solutions were obtained, the substrates were cleaned, and the resultant solution was coated using spin coating for 63 seconds in air at a velocity of 1500 rpm. The obtained sample names CTS-A and CTS-B for annealed 30 sccm and 40 sccm sulphur flux rate, respectively. These films were separately annealed at 550 °C in 30 and 40 sccm H_2S:Ar atmosphere (1:9) using a quartz furnace connected to gas system to improve the optical properties and compensate for the loss of sulfur, if any, in the as-grown thin films. These studies enabled us to decide the best substrate sulphur flux rate among these to obtain samples. After this process, the thin films to be annealed under sulphur flux were kept in 10 % H_2S + 90 % Ar atmosphere at 550 °C temperature in the quartz furnace.

The effect of sulfurization on the optical and theoretically calculated solar cell parameters of CTS thin films are studied in this work. The optical parameters of CTS-A and CTS-B thin films were studied by X-Ray Diffractometer (XRD) system functioned at 40 kV and 40 mA. XRD system is set up with the range of $\theta - 2\theta$ with a resolution of steps of 0.01° to investigate crystallite analysis of the obtained samples. The conclusions of the

absorbance and energy band of the samples were investigated by Shimadzu UV-3600 spectrophotometer between 300-1100 nm. CTS-A and CTS-B samples-based solar cell is created and modeled using SCAPS-1D simulation program, and the influence of various rear connections on the productivity of solar cells generated for this work is investigated.

3. RESULT AND DISCUSSION

3.1. Structural Properties

Fig. 1. XRD spectra of CTS-A and CST-B thin film
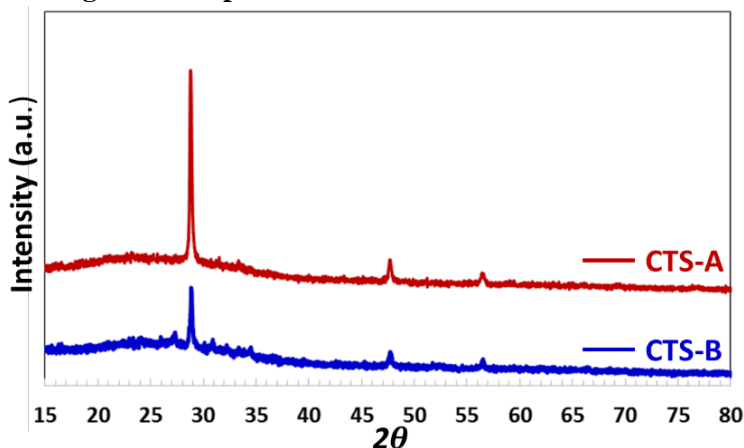
CTS-A and CTS-B samples have been revealed to have mainly tetragonal Cu_2SnS_3 and orthorhombic Cu_3SnS_4 phases, as demonstrated in Figure (Fig) 1 [17]. Their orientations may be shown to be in (112/222), (200/040), (220/044), and (312/262) planes from XRD data created on about $2\theta=28.8^o$, 33.3^o, 47.6^o, and 56.4^o angles, respectively.

The crystallite sizes of the obtained samples are calculated by Scherer equation:

$$D = \frac{0.94\lambda}{\beta cos\theta} \qquad (1)$$

The main crystallite size (D) of CTS-A and CTS-B samples have been calculated to be 42.85 and 40.81 nm, respectively. CTS-A sample has the increase crystallite size while CTS-B has the minimum crystallite size value. In addition, when the sulphur flux rate increased from 30 sccm to 40 sccm, the crystallite size of CTS-B sample decreased. The obtained samples' dislocation density (δ) and micro-strain (ε_{str}) values are determined by Equation (Eq) (2) and Eq (3) as following:

$$\delta = \frac{1}{D^2} \qquad (2)$$

$$\varepsilon_{str} = \frac{\beta}{4tan\theta} \qquad (3)$$

The dislocation density (δ) and micro-strain (ε_{str}) of CTS-A were 5.45×10^{16} lines/m^2 and 0.84×10^{-3} while CTS-B' dislocation density (δ) and micro-strain (ε_{str}) were 6.02×10^{16} lines/m^2 and 0.88×10^{-3}, respectively. Compared to CTS-B thin film, CTS-A thin film exhibits a lower dislocation density and microstrain values, which indicate a more developed crystal structure with fewer lattice defect numbers. [18]. Some modifications in the crystal structure of the CTS-A sample allow for enhanced transmission of minority charge carriers in the CTS solar cell's absorber layer. As a result, the solar cell's series resistance is reduced, and its PV performance is improved.

3.2. The Optical Properties of CTS-A and CTS-B Samples

Fig. 2. a) The absorption spectrum and b) the energy band graph of CTS-A and CTS-B thin film
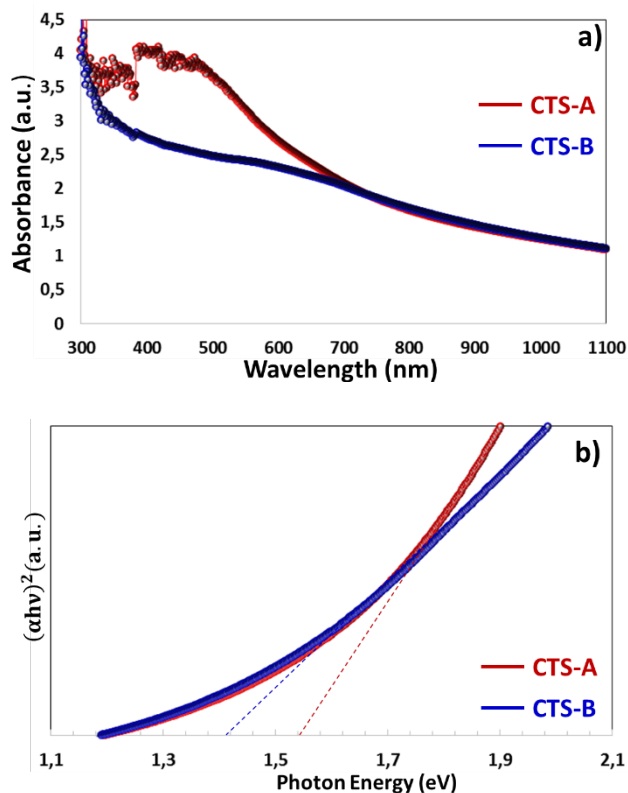
Figure 2 presents the absorption spectra of CTS-A and CTS-B samples. CTS-A thin film absorbs photons more than CTS-B film absorbs in Vis region. The larger crystal size and grain size of CTS-A thin film causes it to absorb more photons. The energy band curve in the Fig. 2b was obtained by using Tauc equation of $Ah\nu = A\left(h\nu - E_g\right)^{1/2}$. The band gaps of samples are determined from the curve intersecting the *x*-axis. The band gaps of CTS-A and CTS-B samples were obtained to be 1.55 eV and 1.42 eV, respectively, [17].

3.3. Mo/*p*-CTS/*n*-CdS/i-ZnO/AZO Solar Cell Modelled by SCAPS-1D Simulation

Fig. 3. Image of Modelled Mo/CTS/n-CdS/i-ZnO/AZO Solar Cell
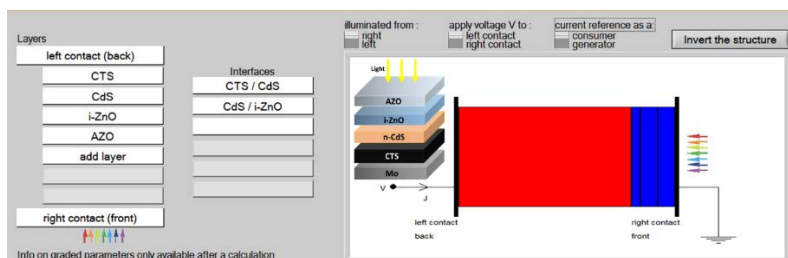
In the study, there were modelled that two different solar cells based on CTS-A and CTS-B samples produced at 30 sccm and 40 sccm sulphur flow, using SCAPS-1D simulation layer [19-21], respectively. Molybdenum (Mo) is the back contact-Cu_2SnS_3 (CTS-A ve CTS-B) is the absorber layer-*n*-CdS is buffer layer-i-ZnO is window layer-Al doped ZnO (AZO) is front transparent electrode layer in Mo/CTS/*n*-CdS/i-ZnO/AZO solar cell. The physical parameters of the layers forming the device used to calculate the PV parameters of the solar cell are presented in the Table-1.

Table 1. The Physical Parameters of the Semiconductor Layers That form CTS-A/CdS the Solar Cell

Layers	AZO[22]	i-ZnO[23]	n-CdS[24]	CTS-A
Band Gap (eV)	3.3	3.3	2.4	1.55
Electron affinity (eV)	4.6	4.6	4.4	4.2
Dielectric permittivity (relative)	9	9	10	14.15
CB effective density of states (cm^{-3})	2.20×10^{18}	2.20×10^{18}	$1.80 * 10^{18}$	$2.20 * 10^{18}$
VB effective density of states (cm^{-3})	1.80×10^{19}	1.80×10^{19}	$2.40 * 10^{19}$	$1.80 * 10^{19}$
Electron/Hole thermal velocity (cm/s)	1.00×10^7	1.00×10^7	$1.00 * 10^7$	$1.00 * 10^7$

Electron/Hole mobility (cm²/Vs)	100/25	100/25	100/25	100/25
Shallow donor density (cm⁻³)	1.00×10^{20}	1.00×10^{5}	$1.00 * 10^{18}$	0
Shallow acceptor density (cm⁻³)	0	0	0	$2.70 * 10^{16}$
Thickness (nm)	100	100	50 nm	1 µm

The physical parameters of layers forming the device used to calculate PV parameters of the solar cell are given in the table. The thickness, absorption coefficient, band gap and calculated dielectric permittivity of experimentally produced CTS-A and CTS-B samples are given in the Table. The parameters of other layers are given based on the literature. In this study, firstly, the operating performances of CTS-A and CTS-B were calculated depending on the density of acceptor defects (N_a), and the efficiency of the CTS-A solar cell showed higher efficiency. Secondly, the electrical parameters of the CTS-A solar cell were calculated under the light and its performance was interpreted, depending on the neutral interfacial defect density (N_t), radiation recombination coefficient (B_r) and Auger electron recombination coefficient.

3.3.1. The Effect of The Acceptor Defect Density İn CTS Samples on The Solar Cell Performance

Fig. 4. The PV Parameters (a-d) and e) $J - V$ Characteristics of CTS-A solar Cell Modelled Depending N_a value.
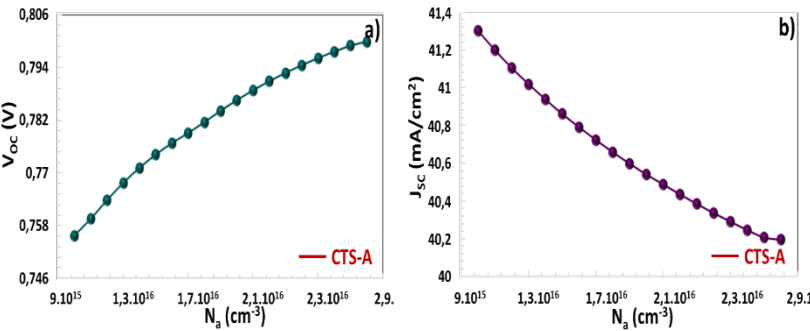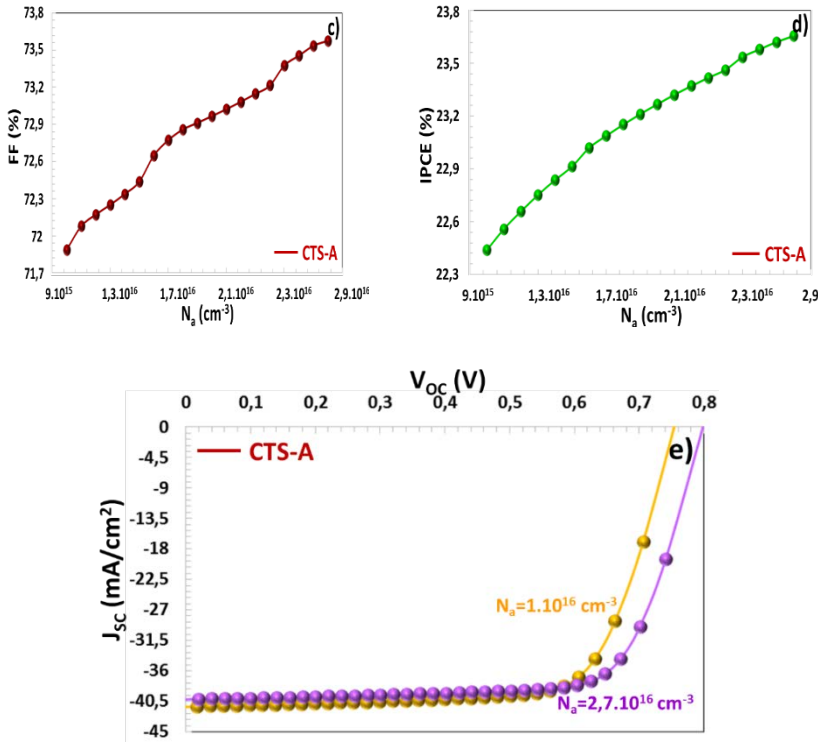
Fig. 4 that presents the operating parameters of the CTS-A solar cell for an illumination environment depending on the acceptor defect density of $N_a = 1.0 \times 10^{16} cm^{-3}$ and $2.7 \times 10^{16} cm^{-3}$. After $N_a = 2.7 \times 10^{16}$ cm^{-3}, the program did not respond. N_a is a parameter that allows the hole density in the valance band of the semiconductor to increase. It enhances the hole intensity and therefore the *p*-type feature in absorber semiconductors [25, 26]. As the N_a value rise, charge accumulation in the depletion region and V_{OC} (open circuit voltage) and FF (Fill Factor) values can increase. According to Fig. 4, when N_a was increased from 1.0×10^{16} to 2.7×10^{16} cm^{-3}, V_{OC}, FF and efficiency (IPCE) increased parabolic from 0.7557 V to 0.7998 V, from 71.88% to 73.57% and from 22.43% to 23.65%, respectively, but J_{SC} (short circuit current) decreased

from 41.302 mA/cm^2 to 40.194 mA/cm^2. The $J - V$ characteristic in the Fig. 4e confirms this change.

PV parameters of the CTS-B solar cell produced at 40 cc sulphur flow were calculated for $N_a = 1.0x10^{16}$ cm^{-3} and $8.0x10^{16}$ cm^{-3} range. As seen in Fig. 5, when N_a was increased from $1.0{\times}10^{16}$ to $8.0{\times}10^{16}$ cm^{-3}, V_{OC}, FF and $IPCE$ increased parabolically from 0.7320 V to 0.7998 V, from 71.24% to 74.78% and from 20.78% to 22. 36%, respectively, but Jsc decreased from 39.85 mA/cm^2 to 37.38 mA/cm^2.The PV performance of CTS-B solar cell showed similar characteristics to CTS-A, but it had slightly lower electrical parameters for the same Na values. This can be attributed to the fact that the CTS-B solar cell has a lower absorption spectrum and a lower amount of photo-excited electron-hole pairs are formed in it.

Fig. 5. The PV Parameters (a-d) and e) $J - V$ Characteristics of CTS-B Solar Cell Modelled Depending N_a Value.
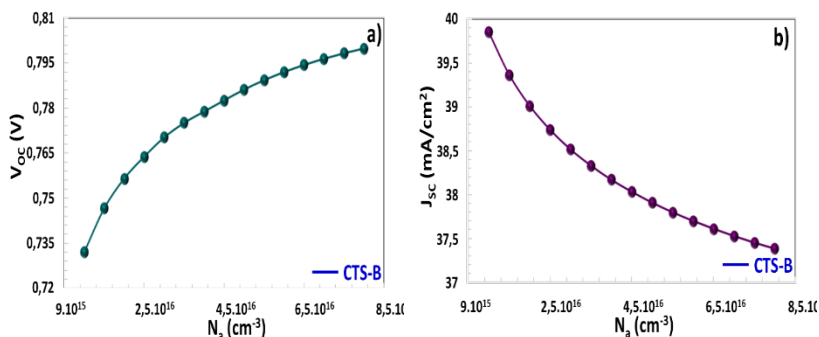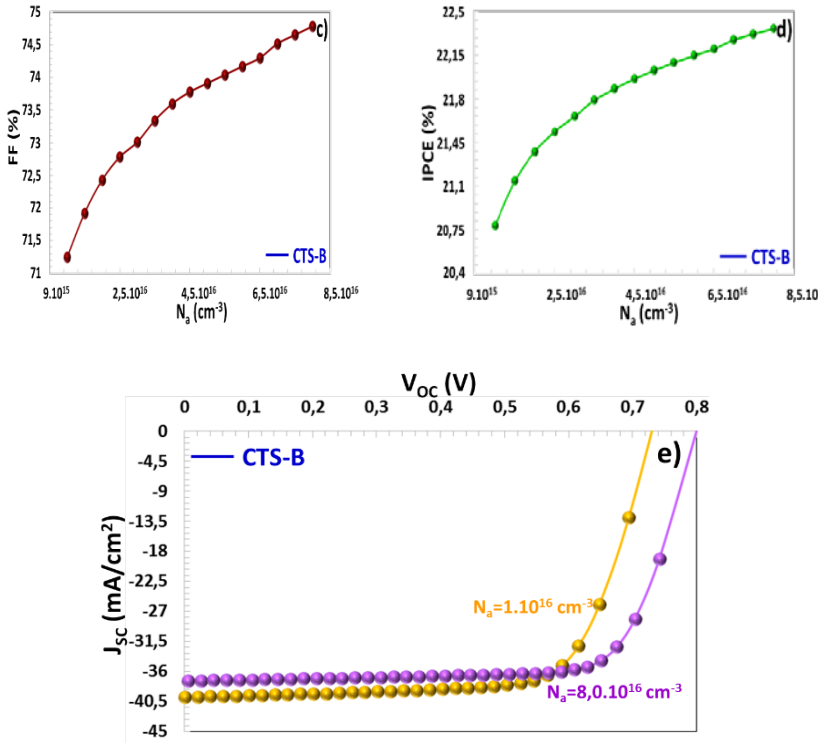
3.3.2. The PV Performance of Solar Cell Depending the Recombination Coefficients

According to the position-dependent energy band characteristics shown in Fig. 6a, CTS-A and *n*-CdS heterojunction structure exhibits a cliff-like band structure [27]. Electron transition from the conduction band of *p*-type CTS-A to the conduction band of *n*-CdS occurs easily. However, recombination can occur during the charge transition from the valence band of CdS to the valence band of CTS. Despite this, the cliff-like band structure facilitates charge accumulation in the CTS-A solar cell and enables high efficiency.

Fig. 6. a) The Energy Band and b) the Generation Characteristics of CTS-A Solar Cell Modelled Depending Position (x)
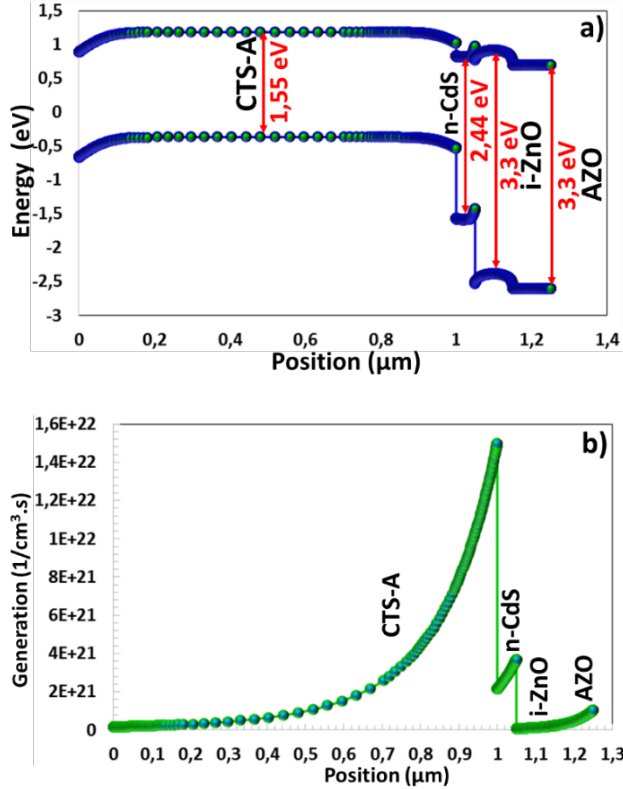
Fig. 6b shows the charge generation characteristics depending on the position in each layer forming CTS-A solar cell. The generation at the contact point (x=0) of Mo contact and CTS-A semiconductor that is 1.63×10^{20} $1/cm^3$s. In the depletion region, the charge formation at the contact point of CTS-A and *n*-CdS semiconductors is 1.5×10^{22} $1/cm^3$s at x=1 µm (in CTS-A absorber layer) and 2.15×10^{21} $1/cm^3$s x=1.0001 µm (in CdS buffer layer). Since photo-excited charge carriers are formed in the CT-AS thin film, which is the absorber layer, the formation is highest at x= 1 µm [28, 29]. Since lower photons are transmitted in the x=0 region, the number of photo-excited charge carriers is

low. In addition, CdS semiconductor has a transparent structure and transmits a high amount of light to the CTS-A. Therefore, less photo-excited charges were generated in CdS thin film (x=1.0001µm).

Fig. 7. The generation/recombination characteristic depending on the thickness of the layers formed the CTS-A solar cell for the radiative recombination coefficient between 10^{-18} and 10^{-2} cm³/s
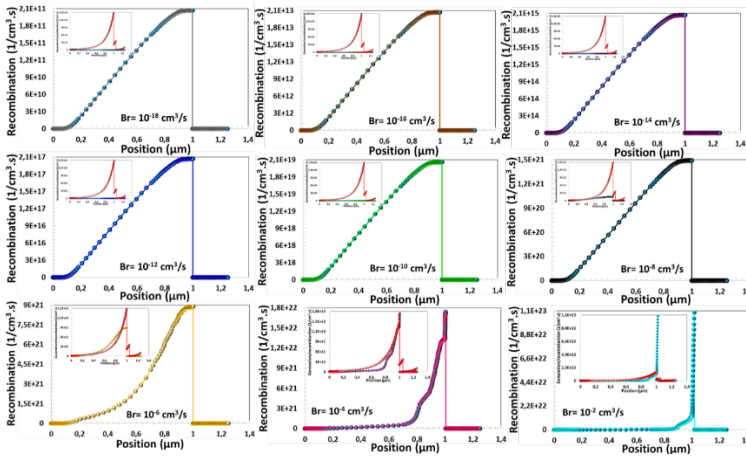
When the hole in the valence band and the electron in the conduction band of the semiconductor that recombine, the excess energy that is emitted as the photon [30]. This event is expressed as the radiative recombination. In the study, the amount of recombined charge depending on the positions of the samples formed the solar cell that was calculated for the $B_r = 10^{-6}$ and $10^{-2} cm^3 s$ range. Radiative recombination took place within CTS-1 absorber layer. When B_r was increased from 10^{-18} and 10^{-2} cm³/s, the amount of the radiative recombination in the absorber layer that increased from 2.1×10^{11} 1/cm³s to 1.8×10^{22} 1/cm³s, according to Fig. [31]. In particular, charge combination occurred in the $B_r = 10^{-6}$ and $10^{-2} cm^3 s$ range, which negatively affected the photo-excited charge formation.

The PV parameter changes characteristics depending B_r value are presented in the Fig. 8. There is no change in the values of PV parameters when $B_r = 10^{-18}$ and $10^{-18} cm^3 s$. However, after the Br= 10^{-7} cm³/s value, these values started to decrease. This is due to the fact that a radiative recombination significantly reduces the number of photo-excited charge carriers, as seen in the Fig. 7. $V_{OC} = 0.7986\,V$, $J_{SC} = 40.2328mA/cm^2$J, $FF = 73.49\%$, $IPCE = 23.61$ for $B_r = 10^{-18}cm^3/s$, while $V_{OC} = 0.7986\,V$, $J_{SC} = 21.9810\,mA/cm^2$, $FF = 41.18\%$, $IPCE = 5.32\%$ for $B_r = 10^{-2}cm^3/s$. The PV parameters decreased significantly after $B_r = 10^{-8}\ cm^3 s$.

Fig. 8. (a-d) The PV parameters and e) $J - V$ characteristic depending the radiative recombination coefficient between 10⁻¹⁸ and 10⁻² cm³/s

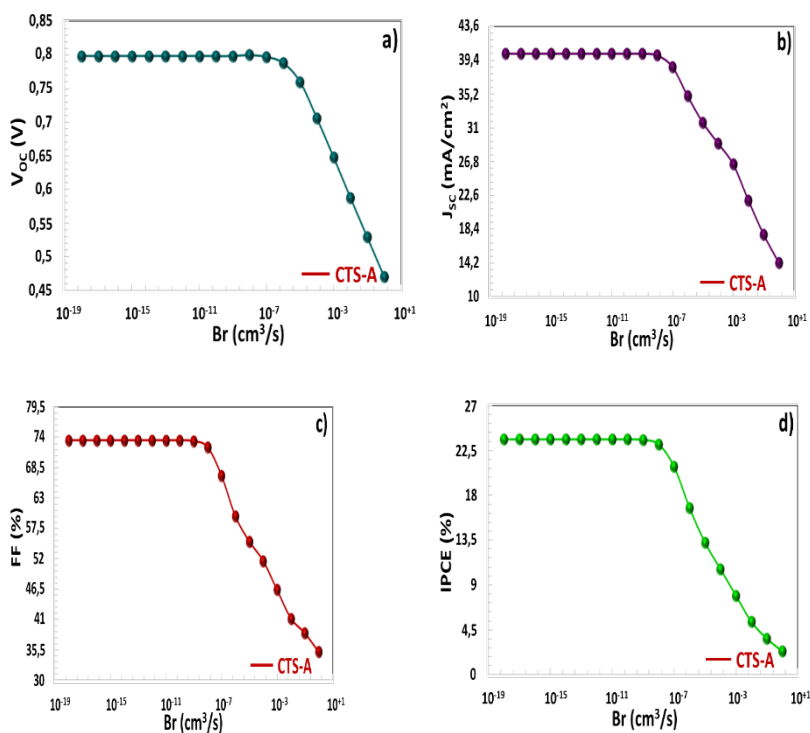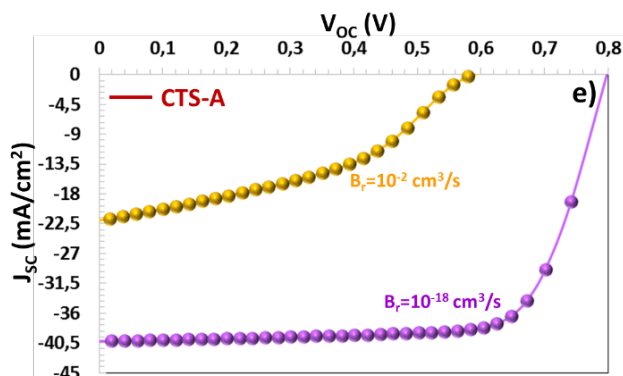**Fig. 9. The generation/recombination characteristic depending on the thickness of the layers formed CTS-A solar cell for the Auger Electron Capture Coefficient (AECC) between 10^{-28} and 10^{-18} cm^6/s.**
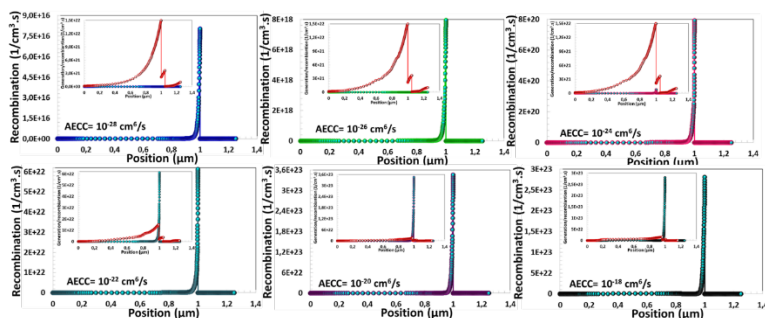
Auger is a non-radiative recombination process. When electrons and holes recombine, the excess energy released is transferred to the electron. Thus, this electron is excited to a higher energy level in the energy band. Fig. 9 shows position-dependent generation/recombination characteristics for Auger electron capture coefficient (AECC) [32, 33]. In $AECC = 10^{-28}$ and 10^{-24} cm^6/s range, the amount of recombination occurred in CTS-A thin film is lower than that of photo-excited charge carriers. In this region, the performance of solar cell may

not be affected much by A. In $AECC = 10^{-20}$ and 10^{-18} cm^6/s regions, the recombination rate [31] significantly exceeds formation. This situation may play a role in reducing the efficiency of solar cell for $AECC = 10^{-20}$ and 10^{-18} cm^6/s.

According to characteristics shown in Fig. 10, the electrical parameters of CTS-A solar cell under light did not change in $AECC = 10^{-20}$ and 10^{-18} cm^6/s, as mentioned above. $V_{OC} = 0.7986\,V$, $J_{SC} = 40.2328\,mA/cm^2$, $FF = 73.49\%$, IPCE=23.61 for AECC=10^{-28} cm^6/s, while $V_{OC} = 0.3638\,V$, $J_{SC} = 6.9663\,mA/cm^2$, $FF = 33.43\%$, $IPCE = 0.84\%$ for $AECC = 10^{-8}cm^6/s$. Because too high number of recombination occurred for $AECC = 10^{-8}cm^6/s$, the performance of solar cell was poor. For the performance of solar cell to improve, $AECC$ should not exceed $AECC = 10^{-22}$ cm^6/s.

Fig. 10. (a-d) The PV parameters and e) $J - V$ characteristic depending the $AECC$ values between $AECC = 10^{-28}$ and 10^{-8} cm^3/s
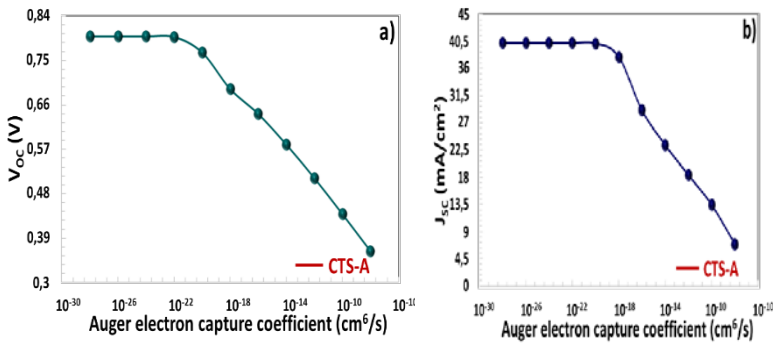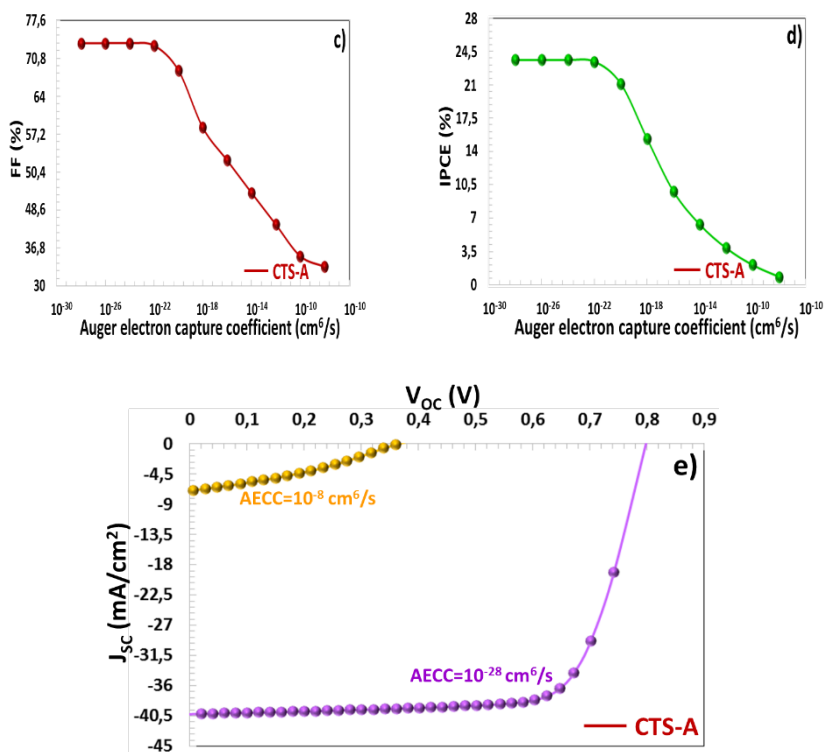
3.3.3. PV Properties of CTS-A Solar Cell Depending the Neutral Interface Defect Density

Fig. 11. (a-d) PV parameters and e) $J - V$ characteristic depending the N_t values between 10^7 and 5.10^{18} cm^{-3}
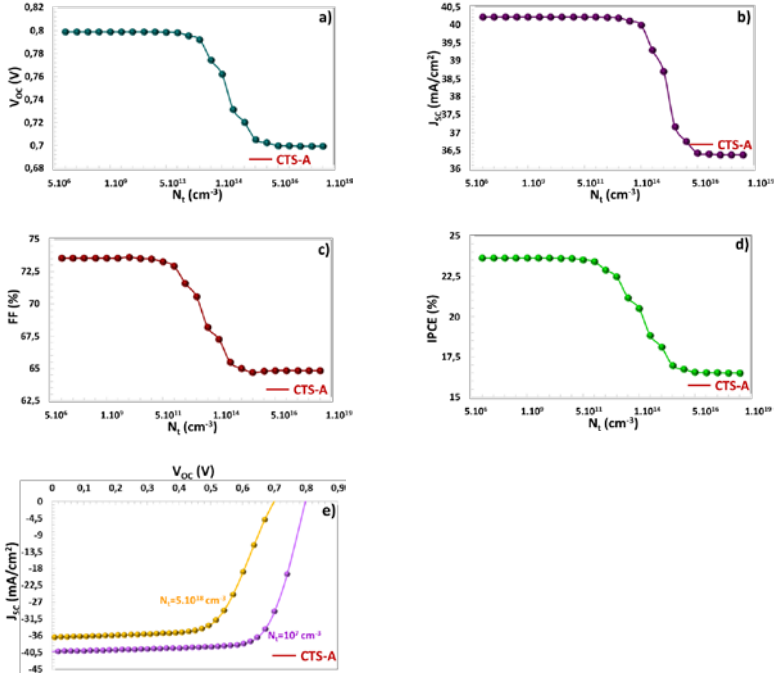
In heterojunction solar cells, interfacial defect structures may occur between p and n semiconductors due to pinholes, cracks, sagging bonds, and unequal lattice structure [34, 35]. These interfacial defects play a role as recombination centers, limit charge accumulation in the deposition region, and negatively affect all electrical parameters of solar cells [36]. In this study, there was no change in the parameters of solar cell between N_t values of 10^7 cm^{-3} and 5×10^{11} cm^{-3}. As N_t increased from 10^{12} cm^{-3} to 10^{16} cm^{-3}, PV parameters decreased significantly and then reached a stable value. $V_{OC} = 0.7986\,V$, $J_{SC} = 40.2328\,mA/cm^2$, FF=73.49%, IPCE=23.61 for $N_t = 10^7\,cm^{-3}$, while $V_{OC} = 0.6994\;V$, $J_{SC} = 36.3913\,mA/cm^2$, $FF = 64.83\,\%$, $IPCE = 16.50\%$ for $N_t = 5.1018\,cm^6/s$.

4. CONCLUSIONS

CTS-A and CTS-B samples were produced using the spray pyrolysis technique at 30 sccm and 40 sccm sulphur flow. The dislocation density and micro-strain value of CTS-A were found to be 5.45×10^{16} lines/m^2 and 0.84×10^{-3} while the dislocation density and micro-strain value of CTS-B were 6.02×10^{16} lines/m^2 and 0.88×10^{-3}. The band gaps of CTS-A and CTS-B samples were found to be 1.55 eV and 1.42 eV, respectively. Mo/CTS-A&CTS-B/n-CdS/i-ZnO/AZO solar cells were modelled with SCAPS and N_a-based PV parameters were calculated for their samples. A cliff-like band structure has formed between CTS-A and n-CdS semiconductors. The highest charge generation within CTS-A thin film is 1.5×10^{22} 1/cm^{3}s. Some more improved PV performance was observed for CTS-A thin film. CTS-A solar cell showed the highest efficiency for $N_a = 2.7 \times 10^{16} cm^{-3}$. After $B_r = 10^{-8}\ cm^3/s$, $AECC = 10^{-22}\ cm^6/s$ and $N_t = 5 \times 10^{11} cm^{-3}$, the efficiency of solar cells becomes lower and therefore these values should not be exceeded for high performance.

- Dicle University Scientific Research Project (BAP) Coordination for the support with the number FEN.18.007 project,

REFERENCES

1. Ghediya, P.R., et al., Electrical Properties of Compact Drop-Casted Cu_2SnS_3 Films. Journal of Electronic Materials, 2020. 49: p. 6403-6409.

2. Orletskii, I.G.e., et al., Structural, optical, and electrical properties of Cu_2SnS_3 samples produced by sol gel method. Physics of the Solid State, 2017. 59: p. 801-807.

3. Vanalakar, S., et al., Fabrication of Cu_2SnS_3 thin film solar cells using pulsed laser deposition technique. Solar Energy Materials and Solar Cells, 2015. 138: p. 1-8.

4. Dias, S., B. Murali, and S. Krupanidhi, Solution processible Cu_2SnS_3 samples for cost effective photovoltaics: Characterization. Materials Chemistry and Physics, 2015. 167: p. 309-314.

5. Patel, B., et al., Electrical properties modulation in spray pyrolysed Cu_2SnS_3samples through variation of copper precursor concentration for photovoltaic application. Journal of Analytical and Applied Pyrolysis, 2018. 136: p. 35-43.

6. He, M., et al., Fabrication of sputtered deposited Cu_2SnS_3 (CTS) thin film solar cell with power conversion efficiency of 2.39%. Journal of Alloys and Compounds, 2017. 701: p. 901-908.

7. Wen, Z., et al., Hierarchical bimetallic sulfides Cu_3SnS_4- Cu_2SnS_3/NC: Toward high-rate performance anode for

lithium-ion battery. Journal of Alloys and Compounds, 2023. 932: p. 167644.

8. Rahaman, S., et al., Effect of copper concentration on CTS samples for solar cell absorber layer and photocatalysis applications. Superlattices and Microstructures, 2020. 145: p. 106589.

9. Zhou, J., et al., Preparation and characterization of Cu_2ZnSnS_4 microparticles via a facile solution route. Materials Letters, 2012. 81: p. 248-250.

10. Seboui, Z., A. Gassoumi, and N. Kamoun-Turki, Evolution of sprayed Cu_2ZnSnS_4. Materials science in semiconductor processing, 2014. 26: p. 360-366.

11. Shelke, H., et al., Photoelectrochemical (PEC) studies on Cu_2SnS_3 (CTS) samples deposited by chemical bath deposition method. Journal of colloid and interface science, 2017. 506: p. 144-153.

12. Kim, I.Y., et al., Influence of annealing temperature on the properties and solar cell performance of Cu_2SnS_3 (CTS) thin film prepared using sputtering method. Journal of Alloys and Compounds, 2016. 688: p. 12-17.

13. Shelke, H.D., et al., Facile synthesis of Cu_2SnS_3 samples grown by SILAR method: effect of film thickness. Journal of Materials Science: Materials in Electronics, 2017. 28: p. 7912-7921.

14. Jia, Z., et al., The photovoltaic properties of novel narrow band gap Cu_2SnS_3 films prepared by a spray pyrolysis method. RSC Advances, 2015. 5(37): p. 28885-28891.

15. Basak, A., et al., Impact of post-deposition annealing in Cu_2SnS_3 thin film solar cells prepared by doctor blade method. Vacuum, 2018. 156: p. 298-301.

16. Dahman, H., et al., Structural, morphological and optical properties of Cu_2SnS_3 thin film synthesized by spin coating technique. Vacuum, 2014. 101: p. 208-211.

17. Candan, I., et al., Production of Cu_2SnS_3 samples depending on the sulphur flow rate and annealing temperature time. Journal of Optoelectronics and Advanced Materials, 2023. 25(3-4): p. 191-202.

18. Chamekh, S., N. Khemiri, and M. Kanzari, Effect of annealing under different atmospheres of CZTS samples as absorber layer for solar cell application. SN Applied Sciences, 2020. 2: p. 1-8.

19. Khaaissa, Y., et al., Experimental and numerical simulation of deposition time effect on ZnS samples for CZTS-based solar cells. Optical and Quantum Electronics, 2021. 53(9): p. 1-21.

20. Shafi, M.A., et al., Optimization of Electrodeposition Time on the Properties of Cu_2ZnSnS_4 Samples for Thin Film Solar Cell Applications. 2021.

21. Khemiri, N., S. Chamekh, and M. Kanzari, Properties of thermally evaporated CZTS samples and numerical simulation of earth abundant and non toxic CZTS/Zn (S, O) based solar cells. Solar Energy, 2020. 207: p. 496-502.

22. Adewoyin, A.D., et al., Development of CZTGS/CZTS tandem thin film solar cell using SCAPS-1D. Optik, 2019. 176: p. 132-142.

23. AlZoubi, T. and M. Moustafa, Numerical optimization of absorber and CdS buffer layers in CIGS solar cells using SCAPS. Int. J. Smart Grid Clean Energy, 2019. 8: p. 291-298.

24. Barman, B. and P. Kalita, Influence of back surface field layer on enhancing the efficiency of CIGS solar cell. Solar Energy, 2021. 216: p. 329-337.

25. Zhou, X. and J. Han, Design and simulation of C_2N based solar cell by SCAPS-1D software. Materials Research Express, 2020. 7(12): p. 126303.

26. Houimi, A., et al., Numerical analysis of CZTS/n-Si solar cells using SCAPS-1D. A comparative study between experimental and calculated outputs. Optical Materials, 2021. 121: p. 111544.

27. Sylla, A., S. Touré, and J. Vilcot, Theoretical analysis of the effects of band gaps and the conduction band offset of ZnS-CIGS layers, as well as defect layer thickness. Int. J. Sci. Res, 2017. 6(11): p. 855-861.

28. Niane, D., et al., Generation and Recombination of a CIGSe Solar Cell under the Influence of the Thickness of a Potassium Fluoride (KF) Layer. American Journal of Materials Science and Engineering, 2018. 6(2): p. 26-30.

29. Abderrezek, M. and M.E. Djeghlal, Contribution to improve the performances of Cu_2ZnSnS_4 thin-film solar cell via a back surface field layer. Optik, 2019. 181: p. 220-230.

30. Raj, V., et al., Design of Ultrathin InP Solar Cell Using Carrier Selective Contacts. IEEE Journal of Photovoltaics, 2020. 10(6): p. 1657-1666.

31. Salem, M.S., et al., Analysis of hybrid hetero-homo junction lead-free perovskite solar cells by SCAPS simulator. Energies, 2021. 14(18): p. 5741.

32. Fu, H. and Y. Zhao, Efficiency droop in GaInN/GaN LEDs, in Nitride Semiconductor Light-Emitting Diodes (LEDs). 2018, Elsevier. p. 299-325.

33. Staub, F., U. Rau, and T. Kirchartz, Statistics of the Auger recombination of electrons and holes via defect levels in the band gap—application to lead-halide perovskites. ACS omega, 2018. 3(7): p. 8009-8016.

34. Srivastava, A., et al., Numerical simulations on CZTS/CZTSe based solar cell with ZnSe as an alternative buffer layer using SCAPS-1D. Materials Today: Proceedings, 2021. 43: p. 3735-3739.

35. Meher, S., L. Balakrishnan, and Z. Alex, Analysis of Cu_2ZnSnS_4/CdS based photovoltaic cell: a numerical simulation approach. Superlattices and Microstructures, 2016. 100: p. 703-722.

36. Et-taya, L., T. Ouslimane, and A. Benami, Numerical analysis of earth-abundant Cu_2ZnSn $(S_xSe_{1-x})_4$ solar cells based on Spectroscopic Ellipsometry results by using SCAPS-1D. Solar Energy, 2020. 201: p. 827-835.

EXAMINATION OF PROPERTIES AND APPLICATION AREAS OF COMPOSITES

Ahmet B. DEMİRPOLAT[1]

Mustafa DAĞ[2]

Ercan AYDOĞMUŞ[3]

1. INTRODUCTION

In this research, the production, usage areas, and applications of composite materials have been evaluated. The use of organic and inorganic fillers in polymer composites and their benefits are discussed. Its effect on polymer composites, that is, its advantages and disadvantages, is discussed. The physical and chemical properties of composite materials are evaluated. The properties of metal, ceramic, and polymer composites used today are compared. Some studies in the literature and their originality are discussed in this study.

Amidst the pursuit of economic ascendancy in our globalized world, competition in both production and technology has become an inescapable reality. The consequential surge in production bears a direct impact on the depletion of natural resources, while pollution serves as its indirect aftermath. Scientists, cognizant of the repercussions of pollution and waste, have embarked on initiatives aimed at

---

[1] Doç. Dr., Malatya Turgut Özal Üniversitesi, Arapgir Meslek Yüksek Okulu, Elektronik ve Otomasyon/Makine, ahmetb.demirpolat@ozal.edu.tr, ORCID: 0000-0003-2533-3381

[2] Arş. Gör. Dr., Çankırı Karatekin Üniversitesi, Mühendislik Fakültesi, Kimya Mühendisliği Bölümü, mudag@karatekin.edu.tr, ORCID: 0000-0001-9540-3475

[3] Doç. Dr., Fırat Üniversitesi, Mühendislik Fakültesi, Kimya Mühendisliği Bölümü, ercanaydogmus@firat.edu.tr, ORCID: 0000-0002-1643-2487

combatting, mitigating, and recycling waste, often investigating its potential as a source of energy [1]. An examination of the primary sources of pollution reveals industrialization, the unrestrained utilization of resources, deforestation, air pollution, and the application of fertilizers and pesticides in agriculture as significant contributors. The array of substances causing the most pollution spans both natural and human-made materials, emanating from the indispensable consumption and production activities in our lives [2]. Diverse methods for waste disposal exist, encompassing recycling, incorporation as raw material in various processes, and incineration. In instances where recycling or reusing proves impractical, responsible disposal methods must be employed to safeguard the health of living organisms and the environment.

Globally, waste management has emerged as the paramount approach, encompassing the minimization of medical, domestic, hazardous, and non-hazardous waste. This comprehensive management style involves the collection of waste at its source, storage, the establishment of transportation stations when necessary, recycling, and rigorous monitoring and control processes. A recent paradigm shift towards sustainable waste management has taken root as a prioritized policy worldwide. This involves minimizing waste generation, curbing the unnecessary depletion of natural resources, maximizing the recycling of waste materials, and treating waste as a viable economic input.

This study endeavors to address the issue of waste by integrating waste into polymer composites as additives and filling materials. The overarching goal is not only waste elimination but also the creation of polymer composites imbued with novel properties, contributing to a more sustainable and resource-conscious approach.

1.1.Organic and Inorganic Supplements

The surge in waste production on a global scale, attributed to rapid population growth during the industrialization process, urbanization, escalating economic demands, an increase in the standard of living, and technological progress, has given rise to a myriad of challenges. These challenges have compelled a paradigm shift towards waste management, grounded in the zero waste principle, mandating a reassessment of waste production and consumption. The outright disposal of waste, coupled with neglect of recycling, recovery, and optimization processes, precipitates substantial resource issues, encompassing both energy and raw materials [3].

In response to these challenges, diverse measures have been implemented for the disposal of various types of waste. Illustrative examples abound. Directives from the European Union and corresponding regulations in our country regulate accumulators and batteries to minimize environmental risks and mitigate impacts on human health. Medical wastes, posing threats to both the environment and human health, arising from healthcare providers and medical interventions, are meticulously collected and subjected to specialized processing.

Hazardous wastes, warranting separate evaluation for human and environmental well-being, undergo management in compliance with Turkey's Waste Management Regulation. The management of construction and demolition waste adheres to a regimen focused on reduction, environmentally safe transportation, recycling, and disposal to obviate environmental risks. The implementation of the Regulation on the Control of Excavation Soil, Construction, and Demolition Waste is integral to this approach. End-of-life tires are managed according to a designated regulation, and electrical and electronic equipment (E-waste) is subjected to a regulatory framework upon reaching

the end of its useful life. To facilitate disposal and reuse, these materials are incorporated into various matrices as raw materials, engendering the potential for the acquisition of new properties. The infusion of composite materials into their structure as filling and additive materials is explored for this purpose [4–7].

1.2.Composite materials

The term "composite" inherently denotes materials consisting of two or more components. Composite materials, by definition, are materials created through the amalgamation of two or more distinct components at the macro level along an interface. It is noteworthy that the components constituting composite materials generally retain their individual properties [8]. In historical contexts, millennia before the formal conceptualization of composite materials, they found practical application in the form of adobe layers composed of straw, utilized in house construction. In contemporary settings, composite materials come into play when conventional materials prove insufficient, necessitating enhancement of their properties.

A pivotal milestone in the evolution of composite materials occurred with the discovery of glass fiber in Europe during the early 1930s, marking the commencement of the production of modern composite materials that have since permeated global markets. When scrutinized through the lens of material sciences, these materials can be aptly characterized as modern and high-tech. A salient feature of composite materials lies in their homogeneity at the microlevel structure [9].

To attain recognition as a composite material, certain criteria must be met, including:

-Humane Composition: The material must exhibit compatibility with human applications, ensuring safety and suitability for various uses.

-Multiple Components: A true composite material must consist of different components, and these components must be comprised of two distinct material combinations.

-Three-Dimensional Combination: The materials constituting the composite must effectively combine in three dimensions, demonstrating an integrated structure.

-Enhanced Properties: Composite materials are required to manifest superior properties compared to the individual components they are composed of. In essence, they must exhibit characteristics that surpass those inherent to each constituent material on its own.

-Matrix-Based Classification: Composite materials can be categorized based on the matrix, which is the primary material used. Examples include metal-ceramic composites, metal-polymer composites, and polymer-ceramic composites, each representing different combinations of materials within the composite structure.

1.3. Structure of Composite Materials

The fabrication of composite materials involves the utilization of at least one primary material and at least one reinforcing element. The physical structure of the reinforcement element and the main material within the composite is contingent upon the production method employed and the intended shape during the composite manufacturing process. These materials and reinforcement elements, created through various techniques, sustain their designated forms by establishing a connecting point referred to as the interface. This interface is crucial for preserving their properties without degradation.

The primary objective behind creating composite materials is the enhancement of specific properties inherent in

traditional materials employed in the past. This improvement spans various aspects, such as mechanical properties, chemical properties, thermal properties, physical properties, and cost considerations. Essentially, the production of composite materials aims to elevate and refine the characteristics of materials beyond what traditional counterparts can offer [9].

1.4.Classification of Composite Materials

Composite materials encompass diverse geometric components that confer mechanical strength, along with polymeric, ceramic, or metal materials responsible for binding these components together. The classification of composites spans various methods, but the most prevalent categorization is based on the matrix and reinforcement materials present within them.

a) Classification of Composite Materials According to Matrix Material:

-Metal Matrix Composites: These composites feature main materials composed of metals and a blend of different metals. The secondary phase, or reinforcement, embedded in the metal-based structure can take varied geometric shapes. Metal matrix composites can exhibit superior properties based on the reinforcements incorporated. For instance, combining the high elastic modulus of ceramics with the plastic deformation properties of metals can yield materials with high resistance to abrasion and tensile forces.

-Ceramic Matrix Composites: Notable for their resistance to high temperatures and lightness (density: 1.5-3.0 g/cm3), ceramic matrix composites find utility in environments with extreme temperatures. However, their hard and brittle nature, coupled with low ductility and toughness, makes them susceptible to sudden temperature changes. To address these weaknesses, they are often reinforced with fibers, maintaining a

rigid and brittle structure while exhibiting excellent insulating properties [9].

-Polymer Matrix Composites: Predominantly composed of petrochemical-derived materials, polymer matrix composites are the most extensively utilized composites today. Known for corrosion resistance, durability, ease of processing, moldability, and high load capacity, they are divided into two subtypes [10].

Polymer matrix composites are divided into two: thermoset and thermoplastic matrix composites.

1) Thermoset Matrices: Typically in liquid form, they are used in the production of fiber-reinforced composites, with low viscosity preferred for fiber-reinforced composite manufacturing [11].

2) Thermoplastic Matrices: These matrices undergo melting through heat and solidification through cooling, endowing them with the capability to be reshaped. They can exist in amorphous or semi-crystalline structures [9].

b) Classification of Composites According to Reinforcing Material

-Fiber Reinforced Composites: Among the most prevalent composites, these are frequently reinforced with glass fibers, primarily due to their cost-effectiveness. The properties of these composites are intricately tied to the extensions of the fibers within the composite. The widespread use of glass as a reinforcing material contributes to the popularity of fiber-reinforced composites [10].

-Particle Reinforced Composites: In this type, the dimensions of the reinforcement material and the advantageous properties it imparts to the composite material are crucial. Particles are inclined to enhance the strength of the composite

material rather than its hardness. This type is notable for its strength augmentation.

-Layered Composites: Characterized as both antiquated and extensively utilized, layered composites are lighter than metals yet boast high strength values. Despite incorporating a high number of layers, they exhibit notable strength, high wear resistance, and commendable thermal expansion properties. This type is a well-established class of composites.

-Mixed Composites: These composites feature more than one reinforcing element, each contributing to the composite structure. Despite incorporating diverse reinforcing elements, they maintain a similar composite structure. This versatility in composition allows for tailored combinations of reinforcing materials, offering a range of properties within a single composite [10].

1.5. Advantages and Disadvantages of Composite Materials

Composites are highly esteemed for their diverse properties, presenting a range of advantages over metals. The low specific gravity of composite materials bestows advantages for their utilization in construction applications. Additionally, the inherent properties of fiber-reinforced composites, such as corrosion resistance, thermal insulation, sound insulation, and electrical insulation, contribute to their superiority in sectors where these characteristics are paramount. The unique combination of these properties positions composites as versatile materials, making them particularly valuable in various industries and applications [12, 13].

1.6. Advantages of Composite Materials

-High Strength: Composite materials exhibit remarkable strength values, surpassing many materials in terms of tensile,

bending, impact, and pressure resistance. This heightened strength contributes to their suitability in applications where robust structural integrity is crucial [12, 13].

-Lightweight: Despite their high strength, composite materials offer superior strength-to-weight ratios compared to unreinforced plastic materials and metals. This characteristic contributes to their use in industries where lightweight structures are advantageous [12, 13].

-Design Flexibility: Composite materials provide designers with considerable flexibility, allowing them to shape these materials into complex, simple, large, decorative, or functional forms based on their creative vision and functional requirements [12, 13].

-Ease of Shaping: The malleability of composite materials allows for the cost-effective production of large and intricate parts in a single molding process, leading to savings in both materials and labor.

-Electrical Properties: Properly chosen materials in composite manufacturing can result in materials with exceptional electrical properties. This means that composites can function as either good conductors or excellent insulators, depending on the application requirements [12, 13].

-Dimensional Stabilization: Thermoset composite materials demonstrate the ability to maintain their shape and functionality even under mechanical stresses, providing stability in various applications [12, 13].

-Resistance to Corrosion and Chemical Effects: Composites are resistant to damage from weather conditions, corrosion, and chemical factors, making them suitable for diverse industrial applications [14, 15].

-Permanent Coloring: Colors are typically integrated into composite materials during the molding process, providing a lasting aesthetic appeal without the need for frequent maintenance [14, 15].

-Resistance to Heat and Fire: Composites with low thermal conductivity coefficients find common use in environments requiring high-temperature operations, showcasing resilience against heat and fire.

-Vibration Damping: The inherent structure of composites imparts natural vibration damping and shock absorption properties, making them suitable for applications where these features are beneficial.

-Low Cost: Composite production costs are economical compared to traditional materials like steel, aluminum, and metal mixtures. Ongoing efforts to reduce unit costs have solidified the acceptance of composites, with engineers and designers attesting to their cost-effectiveness and performance in various end uses and applications [14, 15].

1.7.Disadvantages of Composite Materials

-Air Voids and Fatigue: The presence of air voids in polymer-based composites negatively affects the material, particularly in terms of fatigue. Air voids can compromise the structural integrity and fatigue resistance of the composite, impacting its long-term durability.

-Anisotropic Mechanical Properties: The mechanical properties of composites vary in different directions. This anisotropic behavior means that the material may exhibit different strengths or responses to stress and strain depending on the direction in which the forces are applied. This can complicate the design and engineering of composite structures.

-Lower Ductility and Toughness Compared to Ceramics: Composites generally possess lower ductility and toughness when compared to ceramic materials. This characteristic may limit their use in applications where high levels of ductility and toughness are essential.

-Unpredictable Mechanical Properties: Despite advancements in composite technology, the mechanical properties of composite materials can still be somewhat unpredictable. Variations in manufacturing processes, material composition, and other factors can contribute to challenges in precisely predicting how a composite material will behave under specific conditions.

-Limitations in Precision Manufacturing: The presence of fibers in composite materials can pose challenges in precision manufacturing processes such as drilling and cutting. The opening of fibers during these operations can affect the accuracy and precision of manufacturing, limiting the extent to which certain operations can be carried out with high precision.

These disadvantages highlight areas where composite materials may pose challenges or limitations, emphasizing the importance of careful consideration in their selection and application in various industries. Advances in composite technology continue to address some of these drawbacks, contributing to the ongoing improvement of these materials.

1.8. Usage Areas of Composite Materials

The versatility of composite materials is evident in their wide-ranging applications, and the primary usage areas, along with the advantages they offer, can be delineated as follows:

-Urbanism: Housing Construction: Composites find application in housing construction, contributing to structural elements and environmental aesthetics.

-Home Appliances: Composite materials are utilized in the production of complex parts, facilitating ease of assembly and providing protection from electrical effects in various home appliances such as microwave ovens, storage tanks, kitchen counters, and serving trays.

-Electrical/Electronic Industry: Composites with excellent insulation properties play a vital role in the electrical and electronic industry. They are used in insulators, antennas, panel boxes, lighting, circuit breakers, and other components.

-Aviation Industry: Composites have become indispensable in the aviation industry, finding applications in glider bodies, aircraft fuselages, interior decoration, helicopter equipment, and spacecraft. Their use is crucial to enhance resistance and strength while maintaining lightweight characteristics. Composites, replacing conventional materials like aluminum alloys, are favored for their low weight and high strength.

-Automotive Industry: Composites are extensively used in the automotive industry, especially in bodywork, interior parts, tires, springs, shafts, brake and clutch pads. The primary goal is to achieve maximum fuel economy by minimizing the total weight of vehicles.

-Construction Machinery: Composite materials contribute to the reduction of parts and provide electrical insulation in the construction of machine covers and cabins for construction machinery.

-Construction Sector: Composites are employed in various applications within the construction sector, ranging from building facade protection to cold storage, construction molds, and bus stops. They offer design flexibility, ease of transportation, and convenience in assembly.

-Renewable Energy: Composites play a crucial role in renewable energy, particularly in the construction of wind turbines. Glass fiber, in long lengths, is used in the blades of wind turbines, contributing to their strength and durability [16].

-Sports Equipment: Composites are widely used in the production of sports equipment, including water skis, snow skis, surfboards, sports shoes, and golf clubs, among others. Their use enhances performance and durability.

-Agricultural Sector: Composite materials are of significant importance in the agricultural sector, particularly in the manufacturing of water pipes and the construction of irrigation channels. These materials can be tailored to provide features such as light transmittance, corrosion resistance, and easy assembly [14,15].

1.9.Industrial Wastes Used in Composites

The clay waste utilized in the experimental studies comprises residues generated after the refinement of rock salt extracted from salt mines. This waste is a heterogeneous mixture containing various components such as clay, stone, soil, limestone, gypsum, and others. The refining process results in approximately 75% of the daily raw salt feed being transformed into refined salt, which is subsequently released to the market. Consequently, the residual 25% constitutes the average daily amount of clay waste released as a byproduct of the refined rock salt process. For the specific investigation outlined in this study, clay samples sourced from process equipment known as the saturator and decanter, representing segments of the salt factory waste, were employed.

1.10. Polyurethane Polymer Composites

Various resins are available for the production of polyurethanes, and by adjusting the proportions of different components such as silicones, catalysts, blowing agents,

isocyanates, and polyols, polyurethanes with diverse properties can be obtained [17]. Polyurethanes can be categorized based on their content, synthesis methods, and specific applications, leading to different classes that serve specific purposes. These classes include hard, flexible, water-based, vegetable oil-based, adhesive, binder, coating, sealing, and elastomers, each tailored to meet distinct requirements.

Some notable types of polyurethanes include:

- Hard (Rigid) Polyurethane Sponges: Polyurethane foams with a rigid structure, often used in applications where firmness and support are essential.

- Flexible Polyurethane Sponges: Polyurethane foams with a flexible and pliable structure, commonly utilized in applications where comfort and flexibility are key, such as in cushioning and padding.

- Thermoplastic Polyurethanes: Polyurethanes with thermoplastic properties, allow them to be molded and remolded upon heating. These are versatile materials used in various industries for their adaptability.

- Coatings, Adhesives, Sealants, and Elastomers: Polyurethanes designed for specific applications such as coatings, adhesives, sealants, and elastomers, each tailored to provide specialized properties in terms of protection, bonding, sealing, and flexibility.

These examples showcase the versatility of polyurethanes and how their properties can be customized to suit a wide range of applications, from rigid foams to flexible coatings and adhesives.

1.11. Biopolymer Composite Raw Materials

Polyols, integral in producing polyurethane sponges, refer to liquid-phase oligomers or polymeric compounds

containing two or more hydroxyl groups. These polyols encompass various types, including polyether polyols, polyester polyols, hydroxyl-terminated polyolefins, and hydroxyl-containing vegetable oils [18].

-Polyether and Polyester Polyols: These compounds find use in both flexible and hard sponges. Polyester polyols, specifically, are prevalent in constructing hard sponges within the construction industry due to their high ignition temperatures and fire-retardant properties.

-Production of Polyether Polyols: Polyether polyols are produced through anionic polymerization of alkylene oxides in the presence of initiators and catalysts. They offer a broad range of functionality and equivalent weights, allowing precise control to achieve the desired hardness and flexibility in polyurethane sponges.

The versatility of polyols, such as polyether and polyester polyols, plays a pivotal role in tailoring the properties of polyurethane sponges. This flexibility in formulation enables the creation of sponges with specific hardness, flexibility, and fire-resistant characteristics, catering to diverse industrial and construction applications [19].

Animal and vegetable oils are crucial sources of polyols for polyurethane production. Vegetable oils, such as soybean oil, castor oil, sunflower oil, palm oil, and similar varieties, make up 76% of the global production of around 110 million tons per year, primarily used in human food applications. Soybean oil, the most produced vegetable oil globally, constitutes 25% of total oil and animal fats production, followed by palm oil at 18%. In the polyurethane industry, vegetable oil-based polyols favor oils with the highest unsaturation ratio. Chemical reactions convert double bonds, indicative of unsaturation, into hydroxyl groups. Unsaturated vegetable oils include soybean oil, sunflower oil, corn oil, olive oil, and cottonseed oil, while fish oil represents animal oils [20].

A concise overview of literature research in this domain is exemplified by the following studies:

Hasgül (2013) conducted a review titled "Synthesis, characterization, and investigation of potential adsorption capacities of new polymer/clay composite hydrogels with carrageenan additives" [21], Bayram et al. (2022) delved into the subject with a study on "Preparation and properties of n-nonadecane-containing structurally stable composite phase change materials with modified kaolinite clay added poly(styrene-co-divinyl benzene) matrix" [22], Sevim (2007) explored the synthesis and characterization of organoclay/polyvinyl alcohol (PVA) nanocomposites in a study titled "Clay/PVA: Synthesis and Characterization of Organoclay/PVA Nanocomposites" [23], Alparslan (2013) focused on "Synthesis and characterization of polymer-clay composites" [24], Artuk (2016) investigated the experimental behavior of fiber and fly ash added polymer hollow piles in soft clay soils [25], Bulut et al. (2022) scrutinized "The effect of nanoclay particle addition on the axial and lateral buckling properties of basalt fiber reinforced composite plates" [26].

These scholarly contributions collectively contribute to the broader understanding of the synthesis, characterization, and applications of polymer and clay composites in various contexts.

2. CONCLUSIONS

In this research, commonly used polymer composites and their application areas are evaluated. The advantages and disadvantages of the composites preferred according to the intended use were compared. It is seen that the preferred additives are used in the construction, polymer industry, automotive, aviation industry, ballistics, and household goods production of composites.

REFERENCES

[1] P. Hayaloğlu, S. Artan, and B. Seyhan, "Türkiye'de Çevre Kirliliği, Dışa Açıklık ve Ekonomik Büyüme İlişkisi," Yönetim ve Ekonomi Araştırmaları Dergisi, vol. 13, no. 1, pp. 308–325, 2015.

[2] A. Karasu, Yüksek Lisans Tezi, "Çevresel atıklar, nedenleri, çevresel atıkların geri dönüştürülmesi ve yenilenebilir enerji olanaklarının araştırılması," 2013.

[3] B. Eren, Ü. Fen, B. Dergisi, F. Kunt, and Y. Gündüz, "Control of Recyclable Wates and Zero Waste Project Applications: Example of Necmettin Erbakan University," Bitlis Eren Üniversitesi Fen Bilimleri Dergisi, vol. 11, no. 2, pp. 519–528, Jun. 2022.

[4] S. S. Hossain and P. K. Roy, "Sustainable ceramics derived from solid wastes: a review," Journal of Asian Ceramic Societies, vol. 8, no. 4, pp. 984–1009, Oct. 2020.

[5] G. Ahmetli, M. Dag, H. Deveci, and R. Kurbanli, "Recycling studies of marble processing waste: Composites based on commercial epoxy resin," J Appl Polym Sci, vol. 125, no. 1, 2012.

[6] J. Hidalgo-Crespo, M. Soto, J. L. Amaya-Rivas, and M. Santos-Méndez, "Carbon and water footprint for the recycling process of expanded polystyrene (EPS) post-consumer waste.," Procedia CIRP, vol. 105, pp. 452–457, Jan. 2022.

[7] M. A. Khodabandeh, G. Nagy, and Á. Török, "Stabilization of collapsible soils with nanomaterials, fibers, polymers, industrial waste, and microbes: Current trends," Constr Build Mater, vol. 368, p. 130463, Mar. 2023.

[8] Z. Wang, A. Zulifqar, and H. Hu, "Auxetic composites in aerospace engineering," Advanced Composite

Materials for Aerospace Engineering, pp. 213–240, 2016.

[9] A. Kaya and F. Kar, "Properties of concrete containing waste expanded polystyrene and natural resin," Constr Build Mater, vol. 105, pp. 572–578, Feb. 2016.

[10] "Mechanics and Analysis of Composite Materials - Valery V. Vasiliev, Evgeny V. Morozov - Google Kitaplar." Accessed: Dec. 18, 2023.

[11] M. Itoh, K. Inoue, N. Hirayama, M. Sugimoto, and T. Seguchi, "Fiber reinforced plastics using a new heat-resistant silicon based polymer," J Mater Sci, vol. 37, no. 17, pp. 3795–3801, Sep. 2002.

[12] U. Yilmaz, C. Evci, K. Harp Okulu, S. Bilimleri Enstitüsü, and T. Yönetimi Anabilim Dalı Başkanı, "Havacılık ve savunma sektöründe kompozit malzemelerin geleceği," kho.msu.edu.tr, vol. 14, pp. 77–109, 2015.

[13] Y. Özdemir, "Biyo-kompozit Malzemelerin Mekanik Özelliklerinin Geliştirilmesi," 2019, Accessed: Sep. 12, 2022.

[14] Y. Bulut, Mühendis, and undefined 2011, "Selüloz Esasli Doğal Liflerin Kompozit Üretiminde Takviye Materyali Olarak Kullanimi," dergipark.org.tr, Accessed: Sep. 12, 2022.

[15] M. Bulut, "Türkiye'de kompozit malzeme üretimi ve kompozit malzeme sektörünün genel değerlendirilmesi," Yüksek Lisans Tezi, 2014

[16] S. Karabağ, "Rüzgar Türbini Kanadı İmalatı," İzmir Rüzgâr Sempozyumu ve Sergisi, pp. 23–24, 2011.

[17] J. O. Akindoyo, M. D. H. Beg, S. Ghazali, M. R. Islam, N. Jeyaratnam, and A. R. Yuvaraj, "Polyurethane types, synthesis, and applications – a review," RSC Adv, vol. 6, no. 115, pp. 114453–114482, Dec. 2016.

[18] K. Ashida, "Polyurethane and related foams: Chemistry and technology," Polyurethane and Related Foams: Chemistry and Technology, pp. 1–155, Sep. 2006.

[19] D. Jones, "Pharmaceutical applications of polymers for drug delivery," 2004.

[20] F. H. Otey, B. L. Zagoren, and C. L. Mehltretter, "Rigid urethane foams from glycoside polyethers," Industrial and Engineering Chemistry Product Research and Development, vol. 2, no. 4, pp. 256–259, Dec. 1963.

[21] Hasgül and Banu, "Karragenan katkılı yeni polimer/kil kompozit hidrojellerinin sentezi, karakterizasyonu ve potansiyel soğurum kapasitelerinin araştırılması," Jan. 2013.

[22] S. Bayram, H. H. Mert, and M. S. Mert, "Modifiye edilmiş kaolinit kil katkılı poli(stiren-ko-divinil benzen) matrise sahip n-nonadekan içeren şekilce kararlı kompozit faz değiştiren maddelerin hazırlanması ve özelliklerinin belirlenmesi," Journal of the Faculty of Engineering and Architecture of Gazi University, vol. 38, no. 1, pp. 435–450, Jun. 2022.

[23] S. İşçi, "Kil/PVA ve organokil/PVA nanokompozitlerin sentezi ve karakterizasyonu," 2007.

[24] M. Alparslan, "Polimer-kil kompozitlerinin sentezi ve karakterizasyonu," Yüksek Lisans Tezi, 2013.

[25] F. Artuk, "Lif ve Uçucu Kül Katkılı Polimer İçi Boş Kazıkların Yumuşak Kil Zeminlerindeki Davranışının Deneysel Olarak Araştırılması," 2016.

[26] M. Bulut, Ö. Özbek, Ö.Y. Bozkurt, A. Erkliğ, "Effect of nano clay particle inclusion on axial and lateral buckling characteristics of basalt fiber reinforced composites," Journal of the Faculty of Engineering and Architecture of Gazi University 37:4, 1985-1995, 2022.

[27] "İstanbuk Teknik Üniversitesi Fen Bilimleri Enstitüsü Mimarlık Anabilim Dalı Çevre Kontrolü ve Yapı Teknolojisi Programı".

INVESTIGATION OF COLOR REMOVAL CONDITIONS IN METHYL ORANGE AND ERIOCHROME BLACK T USING A PHASE EXTRACTION COLUMN SYSTEM VIA *AGARICUS CAMPESTRIS*/AMBERLITE XAD-4 BIOCOMPOSITE MATERIAL.

Vahap YÖNTEN[1]

Hilal Çelik KAZICI[2]

Mehmet Rıza KIVANÇ[3]

Mustafa Emre AKÇAY[4]

1. INTRODUCTION

1.1. Adsorption

It can be defined as the process of concentrating and concentrating ions or molecules in one phase on the surface of another phase. Activated carbon is frequently used in the remediation of polluted air or water. In short, by immobilising liquids and gases on the solid surface. The process of accumulation can also be called adsorption. The substance showing accumulation is called adsorbate, The adsorbent is the

[1] Prof. Dr., Van Yüzüncü Yıl University/ Engineering Fak. /Enviromental Eng. Department, vahapyonten@yyu.edu.tr ,ORCID: 0000-0003-3069-6371

[2] Assoc. Prof., Van Yüzüncü Yıl University / Science Faculty. / Chemistry Department, hilalkazici@yyu.edu.tr, ORCID: 0000-0001-6391-1811

[3] Assoc. Prof., Van Yüzüncü Yıl University / Vocational School of Health Sciences / Health Technician Department, mr.kivanc@yyu.edu.tr, ORCID: 0000-0002-9667-1225

[4] Assis. Prof., Van Yüzüncü Yıl University / Science Faculty /Biology Department, memreakcay@yyu.edu.tr, ORCID: 0000-0002-9215-3383

material that immobilizied on the surface. Three types of adsorption were known, physical, chemical, exchange (such as ion exchange) Physical adsorption may be due to low interaction or Van Der Walls' forces of the adsorbed molecule. Adsorbed molecule on the solid surface is not attached to a place, it is in a mobile state on the surface. However, The adsorbate accumulates on the surface of material and forms a loose layer. Physical adsorption is usually reversible (reversible). Chemical adsorption is a more powerful as a result of its action (formation of chemical compounds). Usually adsorbate is adsorbed on the surface forms a layer one molecule thick, the molecules do not move on the surface. When the entire adsorbent surface is covered with this mono molecular layer, the adsorbent adsorption capacity is exhausted. This type of adsorption is very rarely reversible (irreversible). In order to remove the adsorbed substance, processes such as heating the adsorbent to high temperatures are applied. Exchange adsorption is by electrical attraction between the surface and adsorbate material. Ion exchange is inform in this class. Here, the attraction between the adsorbate and the adsorbent surface, which have opposite electrical charges, gains importance. Ions with high electric charge and small diameter ions adsorb better adsorption. Despite all these adsorption types, hard to explain an adsorption mechanism with a single adsorption type The speed and rate of adsorption is a function of the adsorbent surface. For this, materials with a large surface area in proportion to their mass, such as activated carbon (1000 m^2/g), , composite and etc. are used.

Pressure during adsorption of gases If it is increased, the adsorbent will stick more amount of pollutant material solutions the same rule applies for adsorption. The adsorption of the solution will be adsorbed two depends on the nature of the substance and its concentration in solution. Temperature also depends on is an important factor (Sawyer, 1978).

1.1.1. Adsorption isotherms

Adsorption isotherms are graphs expressing the equilibrium between the adsorbing substance (q_e, mg g^{-1}) and the non-adsorbing substance (C_e, mg L^{-1}) based on pH and temperature parameters. These isotherms describe the equilibrium concentrations of pollutant solutions prepared at non-identical concentrations with the adsorbent. In our study, Freundlich, Temkin, Langmuir and Harkins-Jura equations were used to define these isotherms. With the help of these equations, the surface properties of the adsorbent and the adsorber-adsorbed relationship were defined. Also, the maximum adsorption capacity, adsorption density and heat of adsorption can be determined (Elmorsi et al, 2014). In this study, linear forms of the above equations were used to describe the equilibrium data.

1.1.2. Langmuir Adsorption isotherm

This isotherm model (Equation 1) assumes that the adsorption process takes place in a single layer and on a homogeneous surface, and that all active points have equal affinity and the same energy for the molecules to be adsorbed. (Langmuir, 1918).

$$log q_e = log k_L \times log\ C_e^{1/n}$$

Here c_e is the equilibrium concentration of water in the medium (mg L^{-1}), q_e is the equilibrium adsorption capacity (mg g^{-1}), k_L is the Langmuir adsorption constant (L mg^{-1}) and qm, the adsorbent maximum adsorption capacity (mg g^{-1}) shows.

1.1.3. Freundlich Adsorption isotherm

Freundlich isotherm is valid for heterogeneous surfaces in monolayer cases is given below.

$$q_e = k_F \times C_e^{1/n}$$

Here k_F and n are experimentally determined fixed adsorption parameters. When $1/n = 1$, the reaction is linear. When $1/n < 1$, adsorbed with increasing concentration. The reaction is said to be taking place in such a way that there is an increase in the amount. Conversely, when $1/n > 1$ For $1/n < 1$, Langmuir and Freundlich model is concave downwards, so that both models can be calibrated to similar data. (Freundlich., 1906)

1.1.4. Temkin Adsorption isotherm

In this model, the interactions of indirect pollutant/pollutant interactions over time are important. It also predicts a decrease in temperature due to increased surface coverage in the layer. (Vijayaraghavan et al. 2006). Temkin isotherm only in the middle range ion concentrations (Israel and Eduok., 1940). The formula of the related isotherm is given below given.

$$q_e = (RT/\ b_T)\ lnA_T + (RT/\ )C_e$$

1.1.5. Harkins-Jura Adsorption isotherm

With the adsorption equation proposed by Harkins and Jura (Jura and Harkins., 1946) The aforementioned difficulties have been overcome in gas-solid systems. Adsorptive the film is of condensed type and therefore the surface pressure is the same as that of the bare surface the difference of the surface tensions of the film-coated surface is a linear function of the area per molecule function. It is surprising that no attempt has been made to extend the Harkins-Jura equation to solute systems at different temperatures.

The theoretical application of the modified Harkins-Jura equation applicable to solute adsorption are given below (Iyer et al., 1942).

$$1/q_e^2 = B_{HJ}/A_{HJ} - (1/A_{HJ})gC_e$$

Isotherms similar to the Harkins-Jura isotherm are obtained for the adsorption of solutes from dilute and ideal solutions on a solid surface

1.2.Fungi

White-rot fungi belong to the class Basidiomycetes and analyse the components of wood and cause the formation of a white residue in the wood. Under natural conditions only those living organisms that are said to degrade lignin efficiently on dead or living wood white rot fungi (Eriksson et al., 1990; Eaton and Hale, 1993). This fungi attack the lignin components of wood, cellulose and they have little effect on haemicellulose and leave them as residues. From cellulose rather, fungi that degrade lignin are called selective degraders. Selective the main reason for the interest in lignin degraders, especially for biotechnological use (Hatakka, 2001; Hofrichter, 2002). White rot fungi, more easily to nitrogen and carbon sources in proteins and carbohydrates found in wood lignin in order to gain access (Hadar et al., 1993). With some fungi many studies carried out for biotechnological purposes have been encountered. These include; Treatment of alcohol factory wastewater (Kahraman and Yesilada, 2001). Treatment of olive oil mill wastewater (Kahraman and Yesilada, 1999; Kahraman and Yesilada, 2001). Use in the decolourisation of dyestuffs and textile factory wastewater (Banat et al., 1996). Removal of lignin from paper pulp (Reid and Paice, 1990). Biological adsorption of heavy metals (Dhawale et al., 1996; Gabriel et all., 1996). Use in the degradation of polyaromatic hydrocarbons (Çagatay, 1997). Use in hormone production (Yesilada et al., 1990), Evaluation of whey (Feijoo et al., 1999).

2. STUDY CONTENT

2.1. Chemicals and Biosorbent Materials

Amberlite XAD-4 Resin was purchased from Merck (Germany) and ion exchange material for biocomposites. For the production of biocomposite material, A. campestris fungus was selected as biological material to bind to resins. This mushroom was collected in Van/TURKEY region and subjected to some processes evaluated. Methyl Orange (MO) and Eriochrome Black T (EBT) were evaluated as pollutant dye selected and provided by Fisher Scientific (USA). Chemical formula of these dyes is shown in Figure 1. 0.1 M NaOH and 0.1 M HCl base and acid, were choosen for pH adjustments of the synthetic dye solutions. These chemicals purchased from Merck (Germany) and they were analytically pure.

Figure 1. Chemical structures of EBT and MO.

2.2. Preparation of Biocomposite Materials

The mushrooms were collected from Van province in Turkey. Mushroom sample, contaminants washed several times for pollutant. They dried at room temparature. The dried fungal biomass was dried in a porcelain container to obtain a fine powder ground in a mortar and pestle. The dried cells were left for 24 hours at a temperature of 1°C to ensure complete death. 12 dried

in the oven at 70°C and the powder cells are stored in dryers until the next use stored. Preparation of *A. campestris* on amberlite resin and immobilization was carried out as follows: 0.1 g of cork powder, 1 g of amberlite resin with 2 ml of ultrapure water. The mixture was wetted several times with 2 ml of ultrapure water so that increases the immobilization efficiency and ensures complete mixing. After these processes, the mixture was dried in an oven for 24 hours to increase the immobilization efficiency heated at 50°C for hours. The resulting product was then ground to a size of less than 120 microns and used as adsorbent for dyes. Amberlite turbidity analyses to determine the efficiency of the resin immobilization of the fungus completed. Turbidity analyses were performed using the whole mushroom amount (0.1 g) of amberlite resin on the immobilized (Yonten et al., 2015; Ahmed and Yönten., 2022)
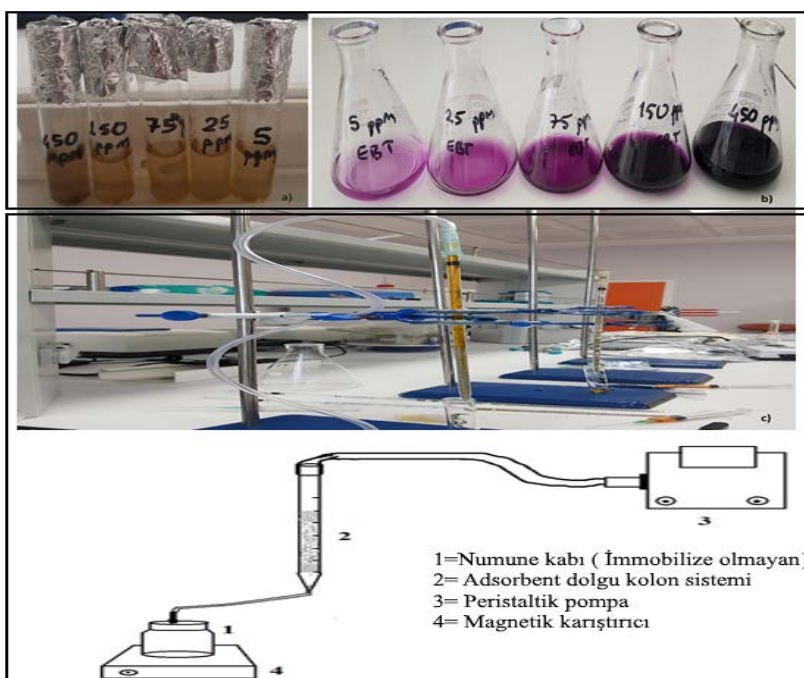
2.3.Biosorption Expermental

All biosorption processes were carried out on 2 ml fixed bed glass phase as shown in Figure 2. columns were used. Prepared in 10 mL, different concentrations of synthetic the dyestuff solutions were placed in a Hanna HI 2211 (China) for pH measurements. More then 0.1 M NaOH and 0.1 M HCl acid for pH adjustments in adsorption experiments Synthetic dye solutions for which pH measurements were made were taken in certain sample volumes injected into fixed bed glass columns at constant flow rate. Contact time, flow rate pH (3, 5, 7, and 9), and initial pH (3, 5, 7, and 9), keeping constant (0.23 min/ml) and temperature (24 °C) concentration (10, 30, 75 and 150 mg/L) sample volume (1, 2, 5 and 10 ml), adsorbent amount or bed thickness (0.2, 0.5, 1.0 and 1.5 g) was taken and experimental design was made. After the end of the adsorption periods, the supernatants from the samples were placed in a centrifuge. The samples were transferred to a WTW 6100 UV spectrometer

(Germany) for dye analysis were placed. UV analyses were performed at 617 nm for EBT and 467 nm for MO.

2.4.Characterization

Characterisation is very important for the proof of adsorption process. Here, it is important to prove the process by expressing the interaction between the pollutant and the adsorbent with images and pictures. The morphological structures before and after the process were imaged by SEM EDX (Scanning Electron Microscopy, Element Detection X-Ray) and the presence of active functional groups formed by the attachment of the pollutant on the surface of the adsorbent was imaged by FTIR (Fourier Transform Infrared Spectroscopy).

Figure 2. a) Post adsorption process b) pre-adsorption process c) fixed bed image and schematic representation of the column.

2.5.Desorption Studies

All biosorption experiments, 86 mg/L dye concentration, flow rate (0.23 min/ml), time (60 minutes) and amount of adsorbent (0.3 g) at fixed parameters fixed bed glass with columns. After the biosorption process, the same biosorption conditions four different desorbing solutions (10 ml each of Acetonitrile, Methanol, Ethanol and water) under desorption experiments were carried out. After the adsorption times were over supernatants from the samples were placed in a centrifuge.

3. RESULT

3.1.Effect of pH on removal

The effect pH plays an important role in the adsorption process, affecting not only the surface charge of the adsorbent and the dissociation of functional groups at the active sites of the adsorbent, but also the chemistry of the dye solution (Huang et al., 2017). The pH values of the sample solutions were adjusted between 2 and 9 with NaOH and H_2SO_4 and passed through fixed bed phase extraction columns (fixed initial concentration 86 mg L_{-1} , sample volume 5 mL, 0.5 g adsorbent and room temperature 24 °C). The adsorption-pH variation of MO and EBT dyes is shown in Figure 3 a) and b). In the related Figure 3 a), adsorption was optimum at pH 5, i.e. in acidic medium, reaching a maximum value of 84.5 ppm. The adsorption of solutions at neutral and basic values is lower than in acidic medium. These results indicate that this adsorbent has a strong adsorption for MO at acidic pH. According to the reviewed literatures, it has been reported that when MO is used, the adsorption or removal is often higher in the acidic range (Öztürk et al., 2015; Yonten et al., 2015; Jiang et al., 2015; Mohammed et al., 2011). In Figure 4 b), while a maximum of 78 ppm of dye is adsorbed at pH 3 in EST adsorption, adsorption decreases towards pH 7 at neutral pH and

adsorption increases towards pH 9, i.e. in basic environment. For both dyes, removal or adsorption is higher in acidic medium. We can express this with the following mechanism. First, MO and EBT dyes are dissolved in water, then the (R - SO$_3$Na) sulfonate groups in the structure of both dyes dissociate and the anionic dye ions,

a) R-SO$_3$Na + H$_2$O → R -SO$_3$ - + Na + Then, due to electrostatic and Van der waals attraction between the dye and the biocomposite materials, adsorption continues as follows.

a) (R - SO3- + Na +) + adsorbent surface → MO or EBT Adsorption

The reason why the adsorption of both dyes increases with pH is the attraction and competition between the OH- ions present in the environment and the ions possessed by the dyes (Huang et al, 2017)

Figure 3. Effect of pH parameter on dyes adsorption a) Methyl Orange, b) Eriochrome Black T.
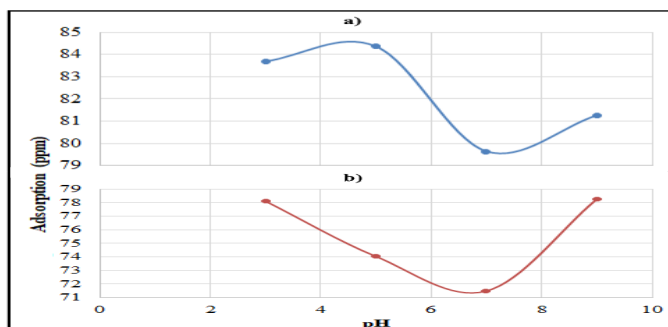

3.2. Effect Of Sample Volume on Removal

Wastewater and industrial effluents consist of organic pollutants with various concentrations. Therefore, it is important to ensure that the sample volume in the water solution to define its effect on the maximum removal capacity dyes amounts are important. To calculate this capacity, as given in Figure 4 1, 2, 5

and 10 mL MO and EST solutions (fixed initial concentration 100 mg L^{-1}, from fixed bed columns under pH neutral conditions (0.5 g adsorbent and room temperature 24°C) passed. In Figure 4 a), the adsorption was the least when taking MO 1 mL sample volume. When the volume was increased, the maximum was 75.6 ppm at a value of 5 mL. However, the related when the parameter was increased to 10 mL, 66.9 ppm was adsorbed. Figure 4 b) On the contrary, maximum adsorption was made while the sample volume was minimum. 1 mL sample volume, an adsorption of approximately 85 ppm is obtained. 18 was realized. However, when the sample volume was increased to 10 mL, the adsorption mininum 52 ppm value, the least removal was achieved

Figure 4. Effect of sample volume on dyes adsorption a) Methyl Orange, b) For Eriochrome Black T
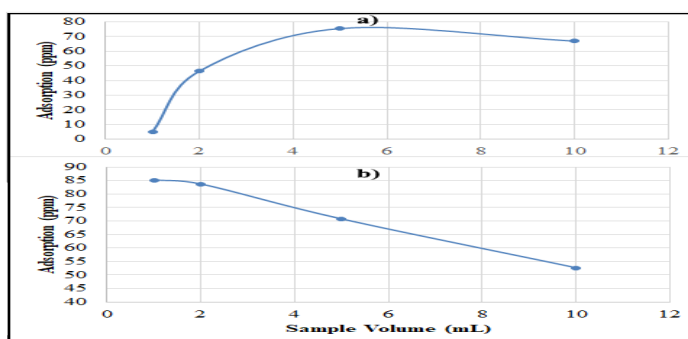
3.3.Adsorption isotherms and compatibility

Adsorption method is generally the preferred process because the adsorbent to be used is cheap and easy to produce. In this process, especially the use of materials that can be evaluated as waste makes this method cheap and effective. Adsorption isotherms are the relations that relate the amount of substance adsorbed on the adsorbent at constant temperature to the equilibrium pressure in the gas or vapor phase and to the equilibrium concentration in solution. As shown in Figure 5 and Figure 6, the interactions between MO and EBT dyes and

biosorbent can be described for the biosorption process by calculating adsorption isotherms. The equations of some important adsorption isotherms used to describe the system are given in the equations below and in our study 4 types of adsorption isotherms and their coefficients are given in the following equations (1, 2, 3, 4) (Langmuir 1918; Freundlich 1906; Temkin and Pyzhev 1940; Harkins and Jura 1946) respectively.

$$log q_e = log k_L \times log\ C_e^{1/n} \tag{1}$$

$$q_e = k_F \times C e^{1/n} \tag{2}$$

$$q_e = (RT/\ )\ ln A_T + (RT/b_T\ ) ln C_e \tag{3}$$

$$1/q_e^2 = B_{HJ}/A_{HJ} - (1/A_{HJ}) x log C_e \tag{4}$$

In the above equations, qe is the amount of dyestuff adsorbed per unit weight of biosorbent (mg/g), C_e is the equilibrium concentration of dyestuff (mg/L); K_F, K_L, b_T, B, A and n are constants that give the adsorption capacity and concentration estimates, respectively. K_L is a measure of the intensity of the biosorption process (L/mg) and qm is the adsorption capacity (mg/g). Q_m and K_L can be found from the slope and shift of a normal plot of $1/q_e$ versus $1/C_e$. In equation (1), the slope n^{-1}, ranging from 0 to 1, is a measure of adsorption intensity or surface heterogeneity. K_F, a constant for the system in Equation (2), is an adsorption coefficient and can be defined as the overall capacity of dye adsorbed onto the corks per unit equilibrium concentration. The results of the isotherms can be determined from the slope and intercept of a typical plot of A_T (L/g) versus qe in C_e at the same time that the b_T isotherm binding constant is found using adsorption capacity data from the regression of Equation 3. In Equation 4, B_{HJ} and A_{HJ} are adsorption isotherm constants. The Harkins-Jurassic adsorption isotherm describes multilayer adsorption and can be explained by the presence of heterogeneous pore distribution in Equation 4

Table 1. Regression coefficients and isotherm constants of adsorption isotherms

Adsorbent	Langmuir			Freundlich			Temkin			Harkins-Jura		
	q_m	K_L	R^2	K_F	n^{-1}	R^2	B_T	$LN\ K_T$	R^2	A_{HJ}	B_{HJ}	R^2
Metyhl Orange	0,21	0,054	0,015	1,01	0.99	80	$7,24*10^{-5}$	-5,59	98	125	$5,5*10^{-5}$	35
Eriocrom Blacy T	-0,21	0,03	16	-0,68	0,41	65	$1,5*10^{-4}$	6680	96	0.501	1.43	25

All values given in Table 1 are found with the help of the above equations and adsorption constants and coefficients of isotherms were found.

Figure 5. a) Langmuir b) Freudlich c) Temkin and d) Harkins-Jura for methyl orange removal adsorption isotherms for Methyl Orange. When Figure 5 and Table 1 are examined, the coefficients and regression constants of the related isotherms are given. Based on these values for MO, the R^2 values of the Temkin adsorption model for Methyl Orange with a numerical data of approximately Temkin Model of removal on *A. Campestris* biomaterial it is clearly seen that it fits.
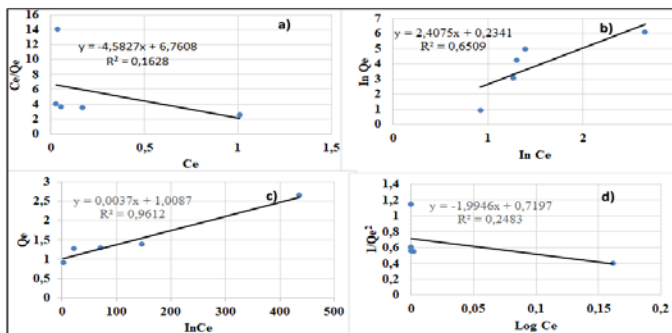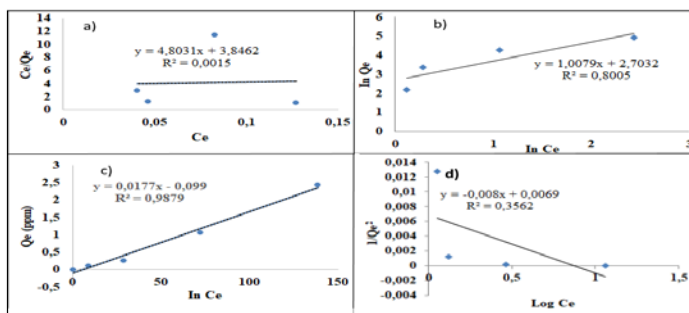
Figure 6. a) Langmuir b) Freudlich c) Temkin and d) Harkins-Jura Adsorption Isotherms for Eriocrom Blact T

As seen in Table 2, the coefficients and regression constants of the isotherms are given. Based on these values taken as a basis for EBT, it is reported that the removal of EBT on Amberlite XAD-4/*A. Campestris* biomaterial fits the Temkin Model with a numerical data of approximately 98% for the Temkin Adsorption model in R^2 values. The characterisation of biocomposites as adsorbents is based on a rigid substance such as the cell wall, which consists of complex layers of many living materials. This structure is chitin material consisting of N-acetyl glucosamine waste. Amberlite XAD-4, which is handled as a polymer, is a resin consisting of white insoluble beads. This resin is a multi-porous material with high surface area. Therefore, Amberlite XAD-4 gives excellent physical, chemical and thermal stability to the polymeric adsorbent. Here these properties allow the fungi to interact both physically and chemically with the polymeric resin surface. Using these interactions between fungi and XAD-4, dyestuff removal was carried out with the column system schematically illustrated in Figure 2. (Yönten et al. 2016). Figure 7 shows (1) the FTIR image of the biomaterial we obtained in raw form, i.e. the peak of the material before removal, (2) the peak of the material after the adsorption of the MO dye on the biomaterial, and finally (3) the FTIR peak of our second dyestuff EST, which expresses the functional groups after removal on the

biomaterial. Wavelengths between 500 and 4000 cm-1 were analyzed before and after adsorption. In the adsorption of MO and EST dyes on the adsorbent, we can see some moving, disappearing peaks and new peaks appearing in parallel. As seen in Figure 8 (1) (2) and (3), the important band bonds at wavelengths 3288, 2918, 1601, 1445, represent -OH groups, NH elongation, -C = C-, carboxylic acid (C = O) or ester and C - N, C - O, C - C, C- functional groups. Between 1300-600 cm - 1 wavelengths, it is accepted that C - N, C - O, C - C and C- functional groups are observed. In addition, the stretching occurring at about 1030 cm-1 wavelength in Figure 8 (2) and (3) proves that the sulfoxide (SO) group present in the structure of the dyes is immobilized in the biomaterial. The observed peaks at about 2822 cm-1 can be attributed to the stretching vibrations of the C-H alkyl groups of the dyes. The peak at about 1601 cm-1 is due to aromatic C=C or may be C=O vibrational stretching of asymmetric and symmetric dyes (Vázquez et al., 2009).

Figure 7. FTIR spectra of the composite material before adsorption (1), Methyl Orange arrested (2) and Eriochrome Black T arrested (3).
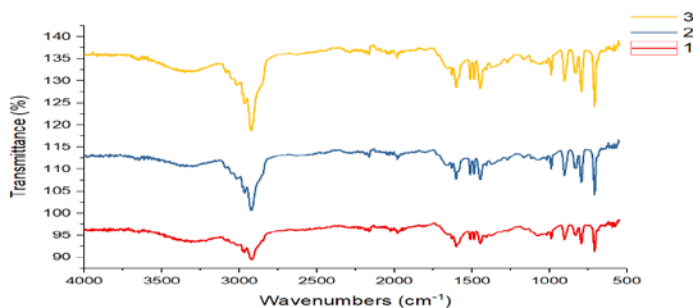
The SEM-EDX image of the pure biocomposite before adsorption is shown in Figure 8 (1), after adsorption of MO to the biosorbent in Figure 9 (2) and after adsorption of EST to the biosorbent in Figure 9 (3). In the related Figure 9 (1), the image of the pure biocomposite in the form of the non-dye-arrested form

is shown. When the EDX image is examined here, we can see that there is no sulfur in the sulfonated compound in the structure of both dyes. At the same time, the potassium in the structure of the fungus forming the biocomposite disappears after the adsorption process. When Figure 9 2) and 3) are examined, both the intense images formed as SEM images and the sulfur element from the dyestuff, which proves this, were calculated as approximately 2.6% for Methyl oranj and approximately 4.47% for EBT. With the help of these data, it was proved that the adsorption process took place.

Figure 8. 1) Pure material before adsorption, 1) biosorbent of MO after adsorption 2) on the biosorbent and 3) on the biosorbent of EBT after adsorption SEM-EDX images.
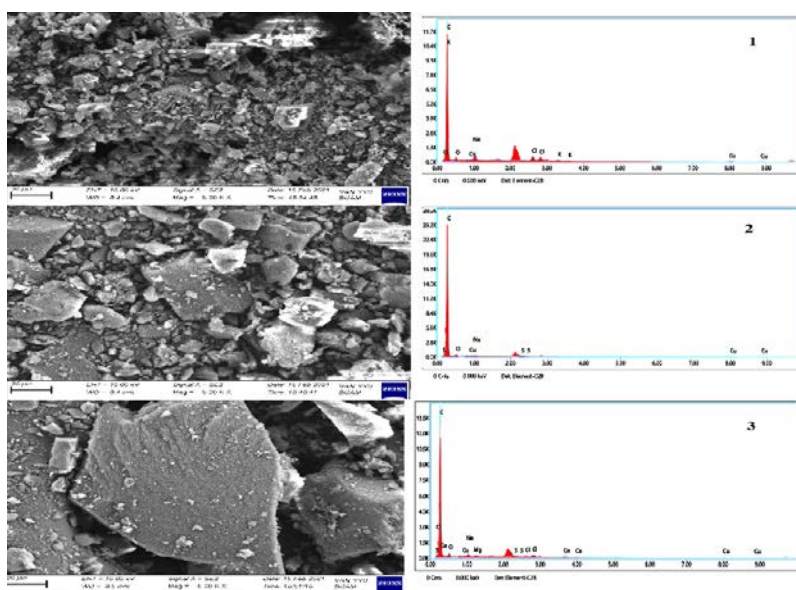
As a result of this study;

a) Adsorption process, recovery, simplicity of design, flexibility, low complete removal of dyes even from concentrated solutions and a cheaper Methyl-Orange and Eriochrome Black T

It has been proven to be highly effective in the removal of dyestuffs.

b) The fixed bed column phase process used as a method is very efficient for optimum removal. practical.

c) Amberlite XAD-4/*A. Campestris* biomaterial used in the process has due to its large surface area, it can be used for the removal of dyestuff from waste water. adsorption technique is considered, the adsorption between the dyestuff ions and the adsorption capacity and adsorbent selectivity values of specific interactions very useful for the enhancement of the efficiency of the product. In addition, SEM-EDX and FTIR characterization process carried out with the devices also shows that the related biosorbent is very suitable. is proved to be the same.

d) Some pH, sample volume and initial concentrations in the medium in the removal process of such parameters were investigated and as a result, it was concluded that the removal of EBT maximum MO at optimum pH 5' and 5 mL dyestuff volume removal was performed. In the removal of EBT, the optimum pH 9 and Maximum removal was achieved at an optimum sample volume of 1 mL.

e) In the adsorption method used for removal, 4 important types (Langmuir, Effects of Freundlich, Temkin and Harkins-Jura Adsorption equations analyzed. In the related equations, Temkin Adsorption Isotherm is used for both dye MO and the highest regression within EST (R^2) coefficients of 96% and He proved that this equation is appropriate with values of 98%.

f) As a result, the preferred biosorbent (Amberlite XAD-4/*A. Campestris*) toxic and synthetically prepared as well as harmful in some industrial effluents effective in the removal of existing Methyl Oranj and Eriochrome Black T dyes are the same as the Amberlite XAD-4/*A. Campestris*. In addition, Amberlite XAD-4/*A. Campestris* as a biocomposite adsorbent for the

removal of other dyes and can be an alternative to materials with low adsorption capacity.

REFERENCE

Ahmed A. A., Yönten V., (2022). Application of Experimental Design Methodology for Adsorption of Brilliant Blue onto Amberlite XAD-4/Agaricus campestris as a New Biocomposite Adsorbent. ARO-The Scientific Journal of Koya University10 (1), pp.10-17

Banat, I. M., Nigam, P., Singh, D., Marchant, R., (1996). Microbial decolorization of textile-dye containing effluents, Bioresource Technol, 58:217-227.

Gabriel, J., Kofronova, O., Rychlovsky, P., Krenzelok, M., (1996). Accumulation and effect of cadmium in the wood-rotting basidiomycete Daedalea quercina, Bull Environ Contam Toxicol, 57:383-390.

Dhawale, S.S., Lane, A.C., Dhawale, S.W., (1996). Effects of mercury on white rot fungus Phanerochaete chrysosporium, Bull Environ Contam Toxicol, 56:835-832.

Elmorsi, T.M., Mohamed, Z.H., Shopak, W., Ismaiel, A.M. (2014). Kinetic and Equilibrium Isotherms Studies of Adsorption of Pb(II) from Water onto Natural Adsorbent. Journal of Environmental Protection, 5, 1667-1681.

Ericsson K.E., Blanchette R.A., Ander P., (1990). Biodegradation of lignin in: microbial and enzymatic degradation of wood and wood components. T.E. Timell (ed.), Springer-Velag GmbH & Co. KG, Berlin, 225–397.

Eaton, R.A., Hale, M.D.C., (1993). Wood decay, Pests and protection. Chapman & Hall, London, 546.

Feijoo, G., Moreira, M.T., Roca, E., Lema, J.M., (1999).Use of cheese whey as a substrate to produce manganase peroxidase by Bjerkandera sp. BOS55, J Ind Microbiol and Biot, 23:86-90

Freundlich H.M.F., (1906) Over the adsorption in solution,J. Phy. Chem. 57, 385-470.

Hadar, Y., Kerem, Z., Gorodecki, B., (1993) .Biodegradation of lignocellulosic agricultural wastes by Pleurotus ostreatus, J Biotechnol, 30:133-139.

Hatakka, A., (2001). Biodegradation of lignin. In: Hofrichter, M., Steinbüchel, A., editors. Biopolymers. Vol 1: Lignin, Humic Substances and Coal. Weinheim, Germany: Wiley-VCH, 129-180.

Harkins, W.D., and Jura, G., (1943). An Adsorption Method for the Determination of the Area of a Solid without the Assumption of a Molecular Area, and the Area Occupied by Nitrogen Molecules on the Surfaces of Solids, J . Chem. Phys.,11: 430 , https://doi.org/10.1063/1.1723871

Hofrichter, M., (2002). Lignin conversion by manganese peroxidase (MnP), Enzyme Microb Technol 30:454-466. https://doi.org/10.1016/S0141-0229(01)00528-2

Huang R., Liu Q., Huo J., Yang B., (2017). Adsorption of methyl orange onto protonated cross-linked chitosan, Arabian J. Chem. 10 (1) 24–32 https://doi.org/10.1016/j.arabjc.2013.05.017.

Israel, U. and Eduok, U. E. (2012). Biosorption of zinc from aqueous solution using coconut (Cocos nuciferaL) coirdust Archives of Applied Science Research, vol. 4, pp. 809–819.

Jura, G., & Harkins, W. D. (1946). Surfaces of solids. XIV. A unitary thermodynamic theory of the adsorption of vapors on solids and of insoluble films on liquid subphases. *Journal of the American Chemical Society, 68*(10), 1941-1952.

Kahraman, S. S., Yesilada,Ö., (1999). Effects of spent cotton on colour removal and chemical oxygen demand lowering in olive mill wastewater by white rot fungi, Folia Microbiologica, 44 (6):673-676.

Kahraman, S., Yesilada, Ö., (2001). Industrial and agricultural wastes as substrates for laccase production by white rot fungi, Folia Microbiol, 46:133-136.

Langmuir, I., (1918). The adsorption of gases on plane surfaces of glass, mica and platinum, J. Am. Chem. Soc.40 1361-1403.

Mohammadi N., Khani H., Gupta V.K., Amereh E., Agarwal S., (2011). Adsorption process of methyl orange dye onto mesoporous carbon material–kinetic and thermodynamic studies, J. Colloid Interface Sci. 362 (2) 457–462 https://doi.org/10.1016/j. jcis.2011.06.067.

Ozturk D., Sahan T., (2015). Design and optimization of Cu (ii) adsorption conditions from aqueous solutions by low-cost adsorbent pumice with response surface methodology, Pol. J. Environ. Stud. 24 (4) 1749–1756.

Reid, D.I., Paice, G.M., (1990). Biological bleaching of kraft pulps by white-rot fungi and their enzymes, FEMS Microbiol Rev, 13:369-376.

Sawyer, C. N. Ve McCarty P. L. (1978). Chemistry For Environmental Engineering, 3rd Ed., McGraw Hill Inc., Singapore, 519,

Temkin, M., V. Pyzhev, (1940). Kinetics of Ammonia Synthesis on Promoted Iron Catalysts,Acta Phy. Chem, URSS 12 327-356.

Vázquez, G., Freire, M. S., González-Alvarez, J., Antorrena, G., (2009). Equilibrium and kinetic modelling of the adsorption of Cd2+ ions onto chestnut shell. Desalination, 249(2): 855-860.

Vijayaraghavan K., T. V. N. Padmesh, K. Palanivelu, and M. Velan, (2006). Biosorption of nickel(II) ions onto Sargassum wightii: application of two-parameter and three-parameter isotherm models, Journal of Hazardous Materials, vol. 133, no. 1–3, pp. 304–308

Yesilada, Ö., Cing, S., Asma, D. (2002). Decolourization of the textile dye Astrazon Red FBL by Funalia trogii pellets, Bioresource Technol, 81:155-157.

Yonten V., Tanyol M., Yildirim N., Yildirim N.C., Ince M., (2015). Optimization of Remazol brilliant blue dye removal by novel biosorbent P. Eryngii immobilized on Amberlite XAD-4 using response surface methodology, Desalin. Water Treat. 57: 15592–15602 .

Yonten V., Ince M.,Tanyol M., Yildirim N., (2015). Adsorption of bisphenol A from aqueous solutions by Pleurotus eryngii immobilized on Amberlite XAD-4 using as a new adsorbent, Desalination and Water Treatment Volume 57, - Issue 47. Water Treat. 57: 22362-22369.

Yönten V., Özgüven A., Ahmed A.A., Akçay M., (2021). Efect of some medium parameters on Brilliant Blue G biosorption by Amberlite resin/*Agaricus campestris* International Journal of Environmental Science and Technology. 18:1709–1718.

OXIDATIVE STRESS: THE MECHANISM AND EFFECT OF REACTİVE OXYGEN SPECIES

Kağan VERYER[1]

1. INTRODUCE

These days, reactive oxygen species (ROS) and free radicals have become important subjects in biological systems. Any substance having one or more unpaired electrons in its outer orbital is referred to as a free radical. While these free oxygen radicals (superoxide (O_2^-), hydroxyl (OH^-), peroxyl (RO_2), and hydroperoxyl (HO_2^-) are examples of compounds that fall under the broad category of ROS, other non-radical oxidative agents include hydrogen peroxide (H_2O_2), hypochlorous acid (HOCl), and ozone (O_3). These substances, known as heavy metals, can also produce these compounds through regular metabolic processes, such as enzymatic reactions, the electron transport system (ETS), signal transduction, nuclear transcription factor activation, gene expression, and involvement in neutrophil and macrophage antimicrobial interactions. (Bayr,2005; Liou and Storz, 2010; Kizildag et al., 2019; Sedefoglu et al., 2022; Jomova et al., 2023).

Antioxidant enzymes and the interactions of different components are the most important processes that the intracellular environment usually consists of to prevent harm from free radicals. (Liang et al., 2023). Some of these compounds can be listed as follows: superoxide dismutase (SOD), catalase,

---

[1] Research Assistant, Osmaniye Korkut Ata University, Faculty of Science and Arts, Department of Biology, kaganveryer@osmaniye.edu.tr 0000-0002-0227-1619

glutathione peroxidase, glutathione, ascorbate (vitamin C), α-tocopherol (vitamin E), and thioredoxin.

Despite the presence of numerous antioxidants within the cell, certain metabolic and ametabolic factors can diminish the level of antioxidants. Cells are specialized structural units where numerous chemical reactions occur, and it is an environment where many redox reactions, including the Electron Transfer System (ETS), take place. This situation leads to the generation of a significant amount of reactive oxygen species. However, exposure to high levels of oxidants is a critical factor contributing to the depletion of antioxidants, leading to the occurrence of a condition known as oxidative stress. If the stress caused by oxidation is not avoided, the cell may experience oxidative damage associated with it. (Brynildsen et al., 2013; Glasaurer, 2013.

1.1. Antioxidant compounds

Compounds capable of neutralizing free radicals are referred to as antioxidants. Antioxidants are frequently divided into groups according to where they come from (natural, synthetic, plant-derived, etc.). Furthermore, vitamins (like C and E), minerals (like manganese and selenium), enzymes (like superoxide dismutase), and other organic materials are commonly included in antioxidants. By reacting with free radicals in the body, these substances create stable molecules that counteract the negative consequences of oxidative damage brought on by free radicals. But antioxidants do more than only squelch free radicals; they are widely used in a wide range of industries (food, medicine, agriculture, packaging, textiles, fuel, etc.). (Yılmaz, 2010; Öğüt, 2014).

Antioxidant compounds, commonly employed in the food and packaging industries, are particularly preferred for the purpose of preventing the oxidation of lipids. (Bayram and

Decker, 2023). This interaction not only preserves the freshness and quality of food products but also ensures flavor and color stability. (Shadidi ve Zhong, 2015). Antioxidants are frequently used in medical applications to stop pharmaceutical industry components from oxidizing and to counteract the negative effects of medications, particularly those linked to oxidative stress. Consistent with their crucial role in preserving the freshness and quality of pharmaceutical components and averting potential negative effects related to oxidative stress, these antioxidants significantly contribute to the stability of color, fragrance, and texture in cosmetic products. (Snezhkina et al., 2019).

1.2. Oxidative damage and its impact on cells

This is connected to oxygen's beneficial and possibly detrimental effects on biological systems. Because oxygen helps to carry electrons across membranes to enable the synthesis of ATP, it is essential for the production of energy within cells, especially during respiration. But this situation also results in the production of free radicals, or reactive oxygen species (ROS), which can damage DNA, lipids, and proteins. (Burton and Jauniaux, 2011; Angelini et al., 2023).

figure 1 The Damages Caused by Reactive Oxygen Species Inside the Cell
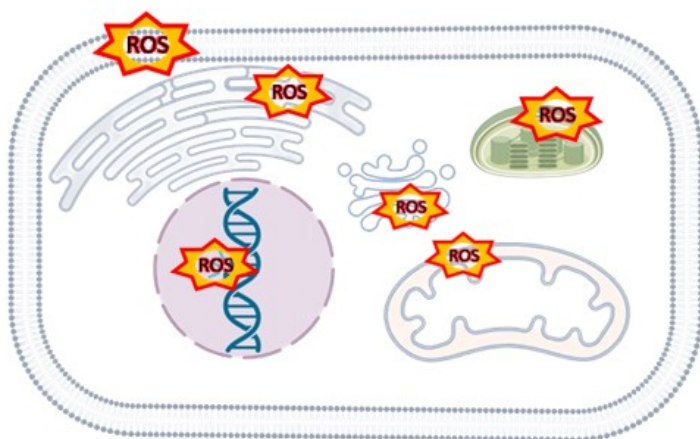
1.3.Proteins

Reactive oxygen species (ROS) can induce oxidative modifications in proteins by attacking specific amino acids within the cell. These modifications have the potential to alter the natural conformation of proteins, thereby impacting the normal functioning of various biological processes within the cell. The occurrence of oxidative damage to a protein can lead to disruptions in fundamental processes such as cellular signal transduction and metabolism. (Zhang et al., 2016).

1.4.Lipids

Oxidative stress can cause lipid molecules in cell membranes to undergo lipid peroxidation. ROS-targeted lipids may cause changes to the membrane's lipid constituents, which would lessen the cell membrane's selectivity and flexibility. As a result, the cell membrane's regular processes are interfered with, making it more difficult for the cell to connect with its environment. This condition may make it difficult for the cell to react effectively, which could cause disruptions to cellular processes and the incapacity of the cell to send out different biological signals. It might potentially cause cell death by compromising the integrity of the cell membrane. (Su et al., 2019; (Bayram and Decker, 2023).

1.5.Nucleic acids (DNA and RNA)

Reactive Oxygen Species (ROS) can interact with nitrogenous structures present in the DNA and RNA chains, which constitute the genetic material, by attacking nucleic acids within the cell. As a result of this interaction, disruptions in base pairs, breaks in DNA chains, and cross-linking can occur. Such damages can significantly compromise the integrity of the genetic material, impair the normal functioning of genes, and lead to disruptions in the biological processes of cells (Wang et al.,

2023). Additionally, mutations can give rise to permanent genetic changes during cell division. (Dong et al., 2023).

In particular, mutations in genes and interruptions in the transport of genetic information across cells can result from alterations in DNA. (Maynard et al., 2009).

Genetic information is extracted from DNA and transported for protein synthesis, a process that is greatly aided by RNA. More specifically, when it comes to ROS, RNA chain disruptions can have a detrimental effect on protein synthesis—a process essential to the cell's essential functions—resulting in the formation of faulty protein structures. Cells may experience normal functionality loss as a result of this condition, and they may even die. Consequently, important cellular functions can be greatly impacted by ROS's effect on nucleic acids. (Qi et al., 2023).

1.6.Mitochondria

Oxidative stress can have negative effects on the electron transport system (ETS) and ATP synthesis in mitochondria. Mitochondria utilize oxygen as the final electron acceptor through the electron transport system. This process leads to the formation of highly reactive byproducts called superoxide (O_2-). Brieflly, mitochondria serve as one of the metabolic sources of reactive oxygen species (ROS) production. (Snezhkina et al., 2019).

Mitochondrial DNA damage: Mitochondrial DNA can be compromised by ROS. Mitochondria possess a small DNA, their own genetic material critical for energy production within the cell. The damage induced by ROS on mitochondrial DNA can disrupt mitochondrial functions. (Snezhkina et al., 2019; Tripathi et al., 2023).

Membrane Damage: ROS have the ability to damage both the inner and outer membranes of mitochondria. This can change the structure of the membranes, compromising their integrity. When the integrity of the mitochondrial membrane is compromised, material may leak out into the intracellular space and damage the cell's organelle structures. (Suski et al. 2011).

Cytochrome C Release: ROS have the ability to cause mitochondria to release cytochrome C. Cells undergo programmed cell death, or apoptosis, which is started by the signaling molecule cytochrome C. This apoptotic pathway may be initiated by ROS-induced mitochondrial and protein damages. (Jiang and Wang, 2004; Qi et al., 2023).

Mitochondria face potential dangers arising from the excessive formation of mitochondrial reactive oxygen species (mtROS) within the cell. To prevent this, mitochondria employ various antioxidant systems. Among these systems, Mn-dependent superoxide dismutase reduces oxidative stress in the cell by eliminating superoxide radicals. Catalase prevents the accumulation of peroxides in the cell by converting hydrogen peroxide into water and oxygen. Glutathione peroxidases, on the other hand, safeguard the integrity of membrane structures, particularly phospholipids, by preventing lipid peroxidation. (Pinegin et al., 2017).

1.7. Ros and antibacterial effect

As a sophisticated component of the immune system, metabolic reactive oxygen species (mROS) assist cellular defense mechanisms against bacterial agents. The immune system uses the generation of reactive oxygen species (ROS), including mitochondrial ROS, as an essential weapon in cellular defense against pathogens. ROS helps defense cells (neutrophils, macrophages, etc.) eliminate bacteria, which in turn interacts directly with pathogens. Basically, organisms use ROS to inflict

cellular damage on pathogens while at the same time using antioxidant systems to protect their own cells. (Mittler et al., 2017; Pinegin et al., 2017).

As a matter of fact, living things use antioxidant systems to protect their own cells from damage while also using reactive oxygen species (ROS) as a defensive mechanism against infection.

2. CONCLUSION

In conclusion, free radicals and reactive oxygen species (ROS) hold significant importance in various aspects of our lives today. While these compounds play a role in numerous biological processes, they also pose a potential threat to cells. Antioxidant systems play a crucial role in preventing free radical damage within cells and combating oxidative stress.

Oxidative damage to cells can occur if oxidative stress is not avoided. Protein oxidative changes can cause problems with basic functions like metabolism and signal transduction in cells. Lipid peroxidation decreases the cell membrane's flexibility, which hinders the membrane's regular functions. Nucleic acid alterations have the potential to damage genetic material and interfere with cell biology by altering its integrity. An extreme environment for oxidative stress is found in mitochondria. Apoptosis can be triggered by mtROS through the release of cytochrome C and damage to mitochondrial DNA. Nevertheless, immune system cells use the overproduction of mtROS within cells to eradicate bacterial cells.

the presence of antioxidant systems that balance the potential dangers of both utilizing ROS in cellular defense against pathogens and causing harm to their own cells demonstrates the intricate balance at work in biological systems. This equilibrium

holds critical importance for cells to maintain normal functionality.

Over time, it has been observed that the number of studies aimed at understanding the ROS mechanism in the literature is increasing. It is anticipated that the utilization of this system, which could be employed in the development of next-generation antibiotics, will enhance the quality of life in the future.

REFERENCES

Angelini, L. L., Dos Santos, R. A. C., Fox, G., Paruthiyil, S., Gozzi, K., Shemesh, M., & Chai, Y. (2023). Pulcherrimin protects Bacillus subtilis against oxidative stress during biofilm development. npj Biofilms and Microbiomes, 9(1), 50.

Bayr, H. (2005). Reactive oxygen species. Critical care medicine, 33(12), S498-S501.

Brynildsen, M. P., Winkler, J. A., Spina, C. S., MacDonald, I. C., & Collins, J. J. (2013). Potentiating antibacterial activity by predictably enhancing endogenous microbial ROS production. Nature biotechnology, 31(2), 160-165.

Burton, G. J., and Jauniaux, E. (2011). Oxidative stress. Best practice & research Clinical obstetrics & gynaecology, 25(3), 287-299.

Dong, X. C., Liu, C., Zhuo, G. C., & Ding, Y. (2023). Potential Roles of mtDNA mutations in PCOS-IR: a review. Diabetes, Metabolic Syndrome and Obesity, 139-149.

Jiang, X., & Wang, X. (2004). Cytochrome C-mediated apoptosis. Annual review of biochemistry, 73(1), 87-106.

Jomova, K., Raptova, R., Alomar, S. Y., Alwasel, S. H., Nepovimova, E., Kuca, K., & Valko, M. (2023). Reactive

oxygen species, toxicity, oxi-dative stress, and antioxidants: Chronic diseases and aging. Archives of toxicology, 97(10), 2499-2574.

Kizildag, N., Cenkseven, S., Koca, F. D., Sagliker, H. A., & Darici, C. (2019). How titanium dioxide and zinc oxide nanoparticles do affect soil microorganism activity?. European Journal of Soil Biology, 91, 18-24.

Liang, J., Gao, Y., Feng, Z., Zhang, B., Na, Z., & Li, D. (2023). Reactive oxygen species and ovarian diseases: Antioxidant strategies. Redox Biology, 102659.

Liou, G. Y., & Storz, P. (2010). Reactive oxygen species in cancer. Free radical research, 44(5), 479-496.

Maynard, S., Schurman, S. H., Harboe, C., de Souza-Pinto, N. C., & Bohr, V. A. (2009). Base excision repair of oxidative DNA damage and association with cancer and aging. Carcinogenesis, 30(1), 2-10.

Pinegin, B., Vorobjeva, N., Pashenkov, M., & Chernyak, B. (2018). The role of mitochondrial ROS in antibacterial immunity. Journal of cellular physiology, 233(5), 3745-3754.

Qi, Q., Yang, S., Li, J., Li, P., & Du, L. (2023). Regulation of redox homeostasis through DNA/RNA methylation and post-translational modifications in cancer progression. Antioxidants & Redox Signaling, 39(7-9), 531-550.

Sedefoglu, N., Zalaoglu, Y., & Bozok, F. (2022). Green synthesized ZnO nanoparticles using Ganoderma lucidum: Characterization and in vit-ro nanofertilizer effects. Journal of Alloys and Compounds, 918, 165695.

Shahidi, F., & Zhong, Y. (2015). Measurement of antioxidant activity. Journal of functional foods, 18, 757-781.

Snezhkina, A. V., Kudryavtseva, A. V., Kardymon, O. L., Savvateeva, M. V., Melnikova, N. V., Krasnov, G. S., & Dmitriev, A. A. (2019). ROS generation and antioxidant defense systems in normal and malignant cells. Oxidative medicine and cellular longevity, 2019.

Su, L. J., Zhang, J. H., Gomez, H., Murugan, R., Hong, X., Xu, D., ... & Peng, Z. Y. (2019). Reactive oxygen species-induced lipid peroxidation in apoptosis, autophagy, and ferroptosis. Oxidative medicine and cellular longevity, 2019.

Suski, J. M., Lebiedzinska, M., Bonora, M., Pinton, P., Duszynski, J., & Wieckowski, M. R. (2012). Relation between mitochondrial membrane potential and ROS formation. Mitochondrial bioenergetics: methods and protocols, 183-205.

Tripathi, D., Oldenburg, D. J., & Bendich, A. J. (2023). Oxidative and Glycation Damage to Mitochondrial DNA and Plastid DNA during Plant Development. Antioxidants, 12(4), 891.

Wang, S., Wang, J., Cai, D., Li, X., Zhong, L., He, X., ... & Bin, J. (2023). Reactive oxygen species-induced long intergenic noncoding RNA p21 accelerates abdominal aortic aneurysm formation by promoting secretary smooth muscle cell phenotypes. Journal of Molecular and Cellular Cardiology, 174, 63-76.

Yılmaz, İ. (2010). Antioksidan içeren bazı gıdalar ve oksidatif stres. Jo-urnal of Turgut Ozal Medical Center, 17(2), 143-154.

Zhang, J., Wang, X., Vikash, V., Ye, Q., Wu, D., Liu, Y., & Dong, W. (2016). ROS and ROS-mediated cellular signaling. Oxidative medicine and cellular longevity, 2016.

ELECTRICAL AND CURRENT-VOLTAGE/CAPACITANCE-VOLTAGE PROPERTIES OF SCHOTTKY DIODES

İlhan CANDAN[1]

Sezai ASUBAY[2]

1. INTRODUCTION TO SEMICONDUCTOR DIODES

Semiconductor diodes are fundamental electronic components that play a pivotal role in modern electronics (Adachi & Sandanayaka, 2020; P. Chen et al., 2021). These devices, constructed from semiconductor materials, exhibit unique electrical properties that enable them to control the flow of electric current in circuits (Jhansi, Balasubramanian, Raman, & Mohanraj, 2022; Panneerselvam, Mohan, Marnadu, & Chandrasekaran, 2022). The most common and widely used type of semiconductor diode is the p-n junction diode.

1.1. Basic structure and operation

At the heart of a semiconductor diode lies the p-n junction, a boundary formed between two differently doped semiconductor regions (CANDAN & ASUBAY, 2023; Li et al., 2023). The p-type region contains positively charged carriers (holes), while the n-type region contains negatively charged carriers (electrons).

---

[1]   Dr., Dicle Üniversitesi, Fen Fakültesi, Fizik Bölümü, ilhan.candan@dicle.edu.tr, ORCID: 0000-0001-9489-5324

[2]   Prof. Dr., Dicle Üniversitesi, Fen Fakültesi, Fizik Bölümü, sezai.asubay@gmail.com, ORCID: 0000-0003-2171-8479

This juxtaposition of charge carriers creates a depletion zone or barrier at the junction (Xia et al., 2022).

1.2. Forward and reverse bias

The behavior of a semiconductor diode can be manipulated by applying an external voltage. When a forward bias is applied, the potential difference aids the movement of charge carriers across the junction, allowing current to flow easily. Conversely, a reverse bias increases the barrier, restricting the flow of current (Greco, Fiorenza, Spera, Giannazzo, & Roccaforte, 2021; Gökçen, Altındal, Karaman, & Aydemir, 2011; Ho et al., 2023).

1.3. Rectification and applications

One of the most notable applications of semiconductor diodes is rectification. Due to their asymmetric conductivity, diodes allow current to flow predominantly in one direction (Majumdar et al., 2023). This property is harnessed in rectifier circuits, converting alternating current (AC) to direct current (DC) essential for various electronic devices.

1.4. Specialized diodes

Beyond the standard p-n junction di ode, there are several specialized types, each designed for specific functions. Zener diodes, for instance, maintain a constant voltage across their terminals, making them crucial in voltage regulation circuits (Saied, 2021). Light-emitting diodes (LEDs) convert electrical energy into light, finding applications in displays, indicators, and lighting (Fakharuddin et al., 2022).

2. INTRODUCTION TO SCHOTTKY DIODES: UNVEILING UNIQUE ELECTRİCAL TRAITS

Schottky diodes stand as distinctive members in the family of semiconductor diodes, renowned for their peculiar electrical properties and applications (Dang et al., 2019; He, Lan, & Liu, 2020). Named after the physicist Walter H. Schottky, these diodes feature a metal-semiconductor junction, setting them apart from traditional p-n junction diodes.

2.1. Metal-semiconductor interface

Unlike conventional diodes, Schottky diodes form a junction between a metal and a semiconductor, typically using metals like platinum, tungsten, or gold (Al-Ahmadi, 2020; Das, Das, Sahu, & Ray, 2023). This metal-semiconductor interface gives rise to a Schottky barrier, a potential energy barrier preventing the flow of majority carriers across the junction (shown in Figure 1).

Figure 1. I-V characteristics of the ZnPc-based Shottky Diodes
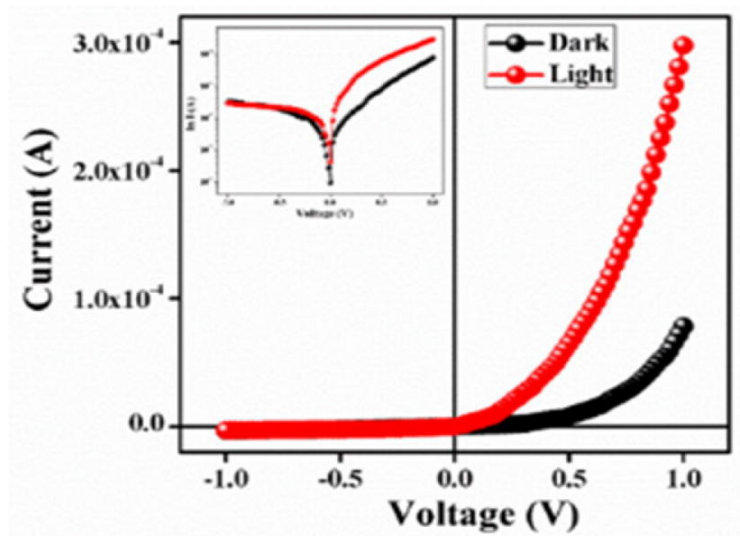
(Al-Ahmadi, 2020).

2.2. Barrier height and speed

A defining characteristic of Schottky diodes is their low forward voltage drop compared to p-n junction diodes. The absence of a depletion region allows for a quicker response to changes in voltage, making Schottky diodes suitable for high-frequency applications (Chand & Kumar, 1996; Osvald, 2009). The barrier height, determined by the work function difference between the metal and semiconductor, contributes to this swift response (given in Table 1).

Table 1. Schottky diode parameters

Condition	On/off Ratio	Conductivity (σ) $(S.m^{-1})$	Photo sensitivity	Ideality factor (η)	Barrier height Φ_B (eV)	Series Resistance (R_S)	
						From *F* vs. *I* (KΩ)	From *G* vs. *I* (KΩ)
Dark	24.27	2.38×10^{-6}		2.82	0.41	9.41	9.61
Light	102.76	1.89×10^{-5}	3.81	1.73	0.32	3.74	3.81

(Al-Ahmadi, 2020)

2.3. Forward bias operation

During forward bias, the Schottky barrier reduces, facilitating the easy flow of electrons from the metal to the semiconductor. This mechanism results in a rapid transition from non-conduction to conduction states, making Schottky diodes ideal for applications requiring fast switching and low power losses (Islam et al., 2020).

2.4. Reverse bias operation

In reverse bias, Schottky diodes exhibit minimal minority carrier storage, contributing to negligible reverse recovery time. This property, known as the lack of the "reverse recovery effect,"

is particularly advantageous in applications where fast turn-off times are critical (Liu et al., 2021).

2.5. Applications

Schottky diodes find extensive use in various electronic circuits and systems (Ezhilmaran et al., 2021). Their low forward voltage drop makes them suitable for power rectification and voltage clamping applications. Additionally, their high-frequency capabilities are leveraged in mixers, detectors, and radio-frequency (RF) devices.

2.6. Challenges and considerations

While Schottky diodes offer unique advantages, they are not without challenges (C. P. Chen et al., 2022). The lack of a depletion region makes them more susceptible to certain forms of leakage currents. Careful consideration of these characteristics is essential in designing circuits to optimize performance.

3. SCHOTTKY BARRIER FORMATION

3.1. Metal-semiconductor contact

Schottky diodes are characterized by the junction formed between a metal and a semiconductor, creating what is known as a metal-semiconductor interface (Turut, 2020). Metals commonly used in Schottky diodes include platinum, tungsten, and gold.

3.2. Work function difference

The key factor in Schottky barrier formation is the difference in work functions between the metal and the semiconductor (Magari, Makino, Hashimoto, & Furuta, 2020). The work function is the minimum energy required to remove an electron from the Fermi level of a material to a point just outside the material.

3.3. Formation of the schottky barrier

When the metal and semiconductor are brought into contact, electrons tend to flow from the metal to the semiconductor until the Fermi levels align (Reddy et al., 2020). However, due to the work function mismatch, not all electrons can transfer across the interface. The surplus electrons in the metal create a region of negative charge, and the deficit of electrons in the semiconductor creates a region of positive charge.

3.4. Creation of potential barrier

The accumulation of charge creates an electric field that opposes the further flow of electrons from the metal to the semiconductor(Nicholls, Dimitrijev, Tanner, & Han, 2019). This electric field forms a potential energy barrier known as the Schottky barrier, which acts as an obstacle for the movement of charge carriers.

3.5. Impact on carrier movement

The presence of the Schottky barrier affects the behaviour of charge carriers (electrons and holes) at the metal-semiconductor interface (Özdemir, Göksu, Yıldırım, & Turut, 2021). In forward bias, when a voltage is applied to the diode in the direction that aids the flow of electrons from the metal to the semiconductor, the barrier is lowered, allowing for current flow. In reverse bias, the barrier height increases, restricting the flow of majority carriers and resulting in minimal current.

Understanding Schottky barrier formation is crucial for comprehending the electrical characteristics of Schottky diodes, including their low forward voltage drop and fast switching capabilities. The unique properties of the Schottky barrier make these diodes valuable in applications where high-speed operation and low power losses are essential.

4. CURRENT-VOLTAGE (I-V) CHARACTERISTICS OF SCHOTTKY DIODES

Schottky diodes exhibit distinctive current-voltage (I-V) characteristics owing to their metal-semiconductor junction. The I-V curve of a Schottky diode provides insights into its behaviour under both forward and reverse bias conditions.

Figure 2. Current characteristics as a function of bias voltage comparison of Shottky diodes at 100, 200 and 300 K
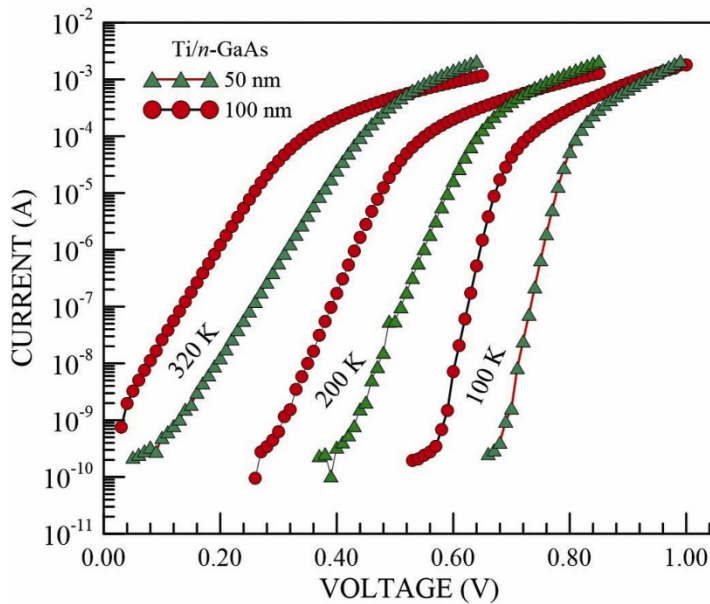
(Özdemir et al., 2021)

4.1. Forward bias operation

Current Flow: In the forward bias, when the voltage is applied in the direction that aids electron flow from the metal to the semiconductor, Schottky diodes exhibit a rapid increase in current.

Low Forward Voltage Drop: One notable characteristic is the low forward voltage drop compared to traditional p-n junction

diodes. This property results from the absence of a depletion region in Schottky diodes, allowing for efficient carrier injection.

4.2. Reverse bias operation

Low Reverse Current: Under reverse bias, Schottky diodes display low reverse current. The absence of a depletion region minimizes the charge storage effect, contributing to fast switching and negligible reverse recovery time.

Increased Barrier Height: The increase in reverse bias voltage enhances the Schottky barrier height, preventing significant electron flow from the semiconductor to the metal.

4.3. Ideality factor and deviations

Ideality Factor: The I-V characteristics are often analyzed using the ideality factor (n). In an ideal diode, n is 1, but in practice, Schottky diodes may deviate from ideality due to factors like series resistance and interface states (Gora et al., 2019).

Deviations from Ideal Behavior: Understanding deviations from ideal behavior is crucial for accurate circuit modeling and performance prediction. Series resistance can affect the slope of the I-V curve, and interface states can introduce non-ideal effects.

4.4. Temperature dependence

Thermionic Emission: Schottky diodes rely on thermionic emission for carrier injection. As temperature increases, thermionic emission enhances, leading to an increase in forward current. Impact on Performance: Engineers must consider the temperature dependence of Schottky diodes, particularly in applications where stability across a range of temperatures is crucial (Patel et al., 2021).

In conclusion, the current-voltage characteristics of Schottky diodes distinguish them with a low forward voltage

drop, rapid response to changes in bias, and minimal reverse recovery time. These characteristics make Schottky diodes valuable in applications requiring high-speed switching and efficient rectification, such as in RF (radio-frequency) circuits, detectors, and power supplies. Engineers carefully consider the I-V characteristics to optimize the performance of Schottky diodes in diverse electronic applications (Jang et al., 2021).

5. CAPACITANCE-VOLTAGE (C-V) CHARACTERISTICS OF SCHOTTKY DIODES

The capacitance-voltage (C-V) characteristics of Schottky diodes are crucial for understanding how the capacitance of the diode varies with applied voltage (Bodunrin, Oeba, & Moloi, 2021). Schottky diodes exhibit distinctive capacitance-voltage (C-V) characteristics, providing valuable insights into their behaviour and performance under varying bias conditions.

5.1. Introduction to C-V analysis

Semiconductor Device Characterization: C-V analysis is a powerful tool used to characterize semiconductor devices, including Schottky diodes (Helal et al., 2020). Understanding Charge Distribution: C-V measurements help in understanding how charge distribution varies with applied voltage.

5.2. Depletion layer capacitance

Capacitance Behavior in Depletion Layer: During reverse bias, the depletion layer in Schottky diodes influences capacitance. Impact of Depletion Width: The width of the depletion layer, influenced by reverse bias voltage, affects the capacitance. A wider depletion layer results in lower capacitance (Murria, Sharma, & Mehta, 2020).

Figure 3. Undoped and Cd-doped p-Si diodes' C-V characteristics in the dark and at room temperature
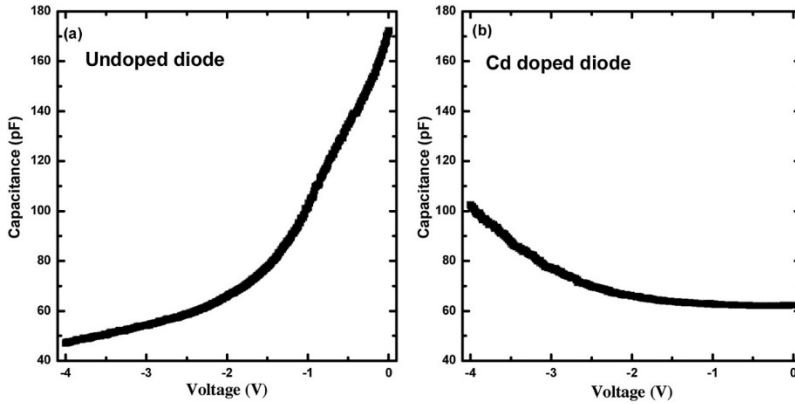
(Bodunrin et al., 2021).

5.3. Transition and diffusion capacitance

Transition Region: The transition region between the depletion and accumulation layers plays a crucial role in C-V characteristics. Diffusion Capacitance: Diffusion capacitance, related to the movement of charge carriers, contributes to the overall capacitance behavior of the diode.

5.4. Frequency dependence

Dynamic Behavior: C-V characteristics are often analyzed at different frequencies to understand the dynamic behavior of Schottky diodes. Transition Between Low and High Frequencies: The transition between low and high frequencies provides insights into the diode's response to changing signals (Cavdar et al., 2022).

5.5. Impact on device performance

Capacitance as a Function of Voltage: Understanding how capacitance varies with voltage is critical for designing circuits using Schottky diodes. Relevance in RF Applications: The C-V characteristics are particularly relevant in radio-frequency (RF)

applications, where the diode's response to varying signals is crucial (Ziane et al., 2021).

5.6. Frequency-dependent capacitance

Dynamic Operation: C-V characteristics help in understanding how capacitance varies with frequency during dynamic operation. Implications for High-Frequency Circuits: In high-frequency circuits, a Schottky diode with predictable C-V characteristics is essential for optimal performance (Cavdar et al., 2022). In conclusion, capacitance-voltage characteristics are integral to understanding how the capacitance of Schottky diodes changes with applied voltage. This knowledge is critical for designing circuits with Schottky diodes, especially in applications where high-frequency operation, signal modulation, and dynamic response are essential considerations (Ziane et al., 2021).

6. CONCLUSION

Advancements in semiconductor technology continually drive the evolution of diodes. Researchers and engineers explore novel materials and designs to enhance performance, efficiency, and miniaturization. This ongoing innovation expands the range of applications, from high-frequency communication devices to power electronics and beyond.

In essence, semiconductor diodes serve as building blocks for electronic circuits, enabling the controlled flow of current and facilitating a myriad of applications across diverse industries. Their simplicity, reliability, and versatility make them indispensable components in the ever-expanding realm of electronic technology.

As technology evolves, ongoing research focuses on refining Schottky diode materials and designs. Innovations aim to address challenges, enhance efficiency, and expand the range of

applications. The continued exploration of new semiconductor materials and manufacturing techniques holds promise for further improving Schottky diode performance.

In summary, Schottky diodes, with their distinctive metal-semiconductor junction and rapid response times, play a vital role in modern electronics. Their unique characteristics make them indispensable in applications where speed, efficiency, and low power losses are paramount.

REFERENCES

Adachi, C., & Sandanayaka, A. S. (2020). The leap from organic light-emitting diodes to organic semiconductor laser diodes. CCS Chemistry, 2(4), 1203-1216.

Al-Ahmadi, N. A. (2020). Metal oxide semiconductor-based Schottky diodes: a review of recent advances. Materials Research Express, 7(3), 032001.

Bodunrin, J., Oeba, D., & Moloi, S. (2021). Current-voltage and capacitance-voltage characteristics of cadmium-doped p-silicon Schottky diodes. Sensors and Actuators A: Physical, 331, 112957.

Candan, İ., & Asubay, S. (2023). Optical and Structural Properties of Metal Doped Copper Oxide Semiconducto. Innovative Research In Natural Science And Mathematics, 83-95.

Cavdar, S., Demirolmez, Y., Turan, N., Koralay, H., Tuğluoğlu, N., & Arda, L. (2022). Investigation of trap states, series resistance and diode parameters in Al/gelatin/n-Si Schottky diode by voltage and frequency dependent capacitance and conductance analysis. ECS Journal of Solid State Science and Technology, 11(2), 025001.

Chand, S., & Kumar, J. (1996). On the existence of a distribution of barrier heights in Pd2Si/Si Schottky diodes. Journal of applied physics, 80(1), 288-294.

Chen, C. P., Jung-Kubiak, C., Lin, R. H., Hayton, D. J., Maestrini, A. E., Siles, J., . . . Mehdi, I. (2022). Silicon Micromachined Waveguide Circuit for a 2 THz Schottky Receiver: Progress and Challenges. IEEE Journal of Microwaves.

Chen, P., Atallah, T. L., Lin, Z., Wang, P., Lee, S.-J., Xu, J., . . . Huang, Y. (2021). Approaching the intrinsic exciton physics limit in two-dimensional semiconductor diodes. Nature, 599(7885), 404-410.

Dang, K., Zhang, J., Zhou, H., Huang, S., Zhang, T., Bian, Z., . . . Wei, K. (2019). A 5.8-GHz high-power and high-efficiency rectifier circuit with lateral GaN Schottky diode for wireless power transfer. IEEE Transactions on Power Electronics, 35(3), 2247-2252.

Das, D., Das, M., Sahu, P., & Ray, P. P. (2023). Investigation of the metal–semiconductor interface by equivalent circuit model in zinc phthalocyanine (ZnPc) based Schottky diodes and its charge transport properties. Materials Today: Proceedings.

Ezhilmaran, B., Patra, A., Benny, S., Sreelakshmi, M., Akshay, V., Bhat, S. V., & Rout, C. S. (2021). Recent developments in the photodetector applications of Schottky diodes based on 2D materials. Journal of Materials Chemistry C, 9(19), 6122-6150.

Fakharuddin, A., Gangishetty, M. K., Abdi-Jalebi, M., Chin, S.-H., bin Mohd Yusoff, A. R., Congreve, D. N., . . . Bolink, H. J. (2022). Perovskite light-emitting diodes. Nature Electronics, 5(4), 203-216.

Gökçen, M., Altındal, Ş., Karaman, M., & Aydemir, U. (2011). Forward and reverse bias current–voltage characteristics of Au/n-Si Schottky barrier diodes with and without SnO2 insulator layer. Physica B: Condensed Matter, 406(21), 4119-4123.

Gora, V. E., Auret, F. D., Danga, H. T., Tunhuma, S. M., Nyamhere, C., Igumbor, E., & Chawanda, A. (2019). Barrier height inhomogeneities on Pd/n-4H-SiC Schottky diodes in a wide temperature range. Materials Science and Engineering: B, 247, 114370.

Greco, G., Fiorenza, P., Spera, M., Giannazzo, F., & Roccaforte, F. (2021). Forward and reverse current transport mechanisms in tungsten carbide Schottky contacts on AlGaN/GaN heterostructures. Journal of Applied Physics, 129(23).

He, Z., Lan, J., & Liu, C. (2020). Compact rectifiers with ultra-wide input power range based on nonlinear impedance characteristics of Schottky diodes. IEEE Transactions on Power Electronics, 36(7), 7407-7411.

Helal, H., Benamara, Z., Arbia, M. B., Khettou, A., Rabehi, A., Kacha, A. H., & Amrani, M. (2020). A study of current-voltage and capacitance-voltage characteristics of Au/n-GaAs and Au/GaN/n-GaAs Schottky diodes in wide temperature range. International Journal of Numerical Modelling: Electronic Networks, Devices and Fields, 33(4), e2714.

Ho, L.-P., Li, S.-h., Lin, T., Cheung, J., Chau, T., & Ling, F. C.-C. (2023). Correlations between reverse bias leakage current, cathodoluminescence intensity and carbon vacancy observed in 4H-SiC junction barrier Schottky diode. Semiconductor Science and Technology, 38(11), 115007.

Islam, Z., Xian, M., Haque, A., Ren, F., Tadjer, M., Glavin, N., & Pearton, S. (2020). In situ observation of β-Ga 2 O 3 Schottky diode failure under forward biasing condition. IEEE Transactions on Electron Devices, 67(8), 3056-3061.

Jang, J., Song, J., Lee, S. S., Jeong, S., Lee, B. J., & Kim, S. (2021). Analysis of temperature-dependent IV characteristics of the Au/n-GaSb Schottky diode. Materials Science in Semiconductor Processing, 131, 105882.

Jhansi, N., Balasubramanian, D., Raman, R., & Mohanraj, K. (2022). Influence of aluminum ion on the structural, optical, and electrical properties of CuO thin films for the PN-Junction diode application. Materials Science for Energy Technologies, 5, 433-443.

Li, Z., Li, J., Wang, W., Yan, Q., Zhou, Y., Zhu, L., . . . Wei, B. (2023). Near Zero-Threshold Voltage P-N Junction Diodes Based on Super-Semiconducting Nanostructured Ag/Al Arrays. Advanced Materials, 35(13), 2210612.

Liu, X., Chen, H., Liang, S., Zhang, M., Jiang, Z., Fan, S., & Sun, Y. (2021). Ultrabroadband electrically controllable terahertz modulation based on GaAs Schottky diode structure. APL Photonics, 6(11).

Magari, Y., Makino, H., Hashimoto, S., & Furuta, M. (2020). Origin of work function engineering of silver oxide for an In–Ga–Zn–O Schottky diode. Applied Surface Science, 512, 144519.

Majumdar, S., Dey, A., Sahu, R., Lepcha, G., Dey, A., Ray, P. P., & Dey, B. (2023). An aromatic acid based supramolecular Zn (II)-metallogel for fabricating light-sensitive metal-semiconductor junction type Schottky diode with

satisfactory rectification ratios. Materials Research Bulletin, 157, 112003.

Murria, M., Sharma, R. K., & Mehta, C. (2020). Capacitance-voltage profiling of aluminium junctioned PVA/CdSe nanocomposite schottky diode. Materials Today: Proceedings, 28, 1445-1449.

Nicholls, J., Dimitrijev, S., Tanner, P., & Han, J. (2019). Description and verification of the fundamental current mechanisms in silicon carbide Schottky barrier diodes. Scientific reports, 9(1), 3754.

Osvald, J. (2009). Temperature dependence of barrier height parameters of inhomogeneous Schottky diodes. Microelectronic Engineering, 86(1), 117-120.

Özdemir, A., Göksu, T., Yıldırım, N., & Turut, A. (2021). Effects of measurement temperature and metal thickness on Schottky diode characteristics. Physica B: Condensed Matter, 616, 413125.

Panneerselvam, A., Mohan, K., Marnadu, R., & Chandrasekaran, J. (2022). The deep investigation of structural and opto-electrical properties of Yb 2 O 3 thin films and fabrication of Al/Yb 2 O 3/p-Si (MIS) Schottky barrier diode. Journal of Sol-Gel Science and Technology, 1-17.

Patel, H., Patel, K., Patel, A., Jagani, H., Patel, K., Solanki, G., & Pathak, V. (2021). Temperature-dependent I–V characteristics of In/p-SnSe schottky diode. Journal of Electronic Materials, 50(9), 5217-5225.

Reddy, P. S., Janardhanam, V., Shim, K.-H., Reddy, V. R., Lee, S.-N., Park, S.-J., & Choi, C.-J. (2020). Temperature-dependent Schottky barrier parameters of Ni/Au on n-type (001) β-Ga2O3 Schottky barrier diode. Vacuum, 171, 109012.

Saied, M. (2021). Novel Technique for The Analysis of Electronic Circuits Including Zener Diodes. Journal of VLSI Design Tools & Technology, 11(3), 31-41p.

Turut, A. (2020). On current-voltage and capacitance-voltage characteristics of metal-semiconductor contacts. Turkish Journal of Physics, 44(4), 302-347.

Xia, H., Luo, M., Wang, W., Wang, H., Li, T., Wang, Z., . . . Wang, F. (2022). Pristine PN junction toward atomic layer devices. Light: Science & Applications, 11(1), 170.

Ziane, A., Amrani, M., Rabehi, A., Douara, A., Mostefaoui, M., Necaibia, A., . . . Bouraiou, A. (2021). Frequency dependent capacitance and conductance–voltage characteristics of nitride GaAs Schottky diode. Semiconductors, 55, 51-55.

DEVELOPMENTS IN SCIENCE

Physics, Chemistry, Biology